

Section IV
High-Energy Astrophysics
and Cosmology

Polarimetric Method for Measuring Black Hole Masses in Active Galactic Nuclei Based on Theory of V.V. Sobolev and S. Chandrasekhar

Yu.N. Gnedin¹, M.Yu. Piotrovich¹

E-mail: *gnedin@gao.spb.ru*

The V.V. Sobolev and S. Chandrasekhar theory of polarized radiation presents the main basis for modern science of the polarized emission of cosmic objects including X-rays and gamma-rays. The accreting supermassive black holes (SMBH) in active galactic nuclei (AGN) are found in the center of modern astrophysics. The main problem is connected with determining the masses of these objects. The virial theorem accepted to a flattened configuration of a broad line region (BLR) in AGNs allows us to get a direct connection between the mass of SMBH and the inclination angle of the accretion flow. The inclination angle itself can be derived from the spectropolarimetric data of broad emission lines using the theory for generation of polarized radiation developed by Sobolev and Chandrasekhar. As a result, the new estimates of SMBH masses in AGN with measured polarization of BLR emission are presented. It is essential that the polarimetric data allow also to determine the value of the virial coefficient that is important for determining SMBH masses and to estimate the recoiling velocity of SMBH.

1 Introduction

AGNs are powered by accretion to a SMBHs, and the broad emission lines seen in Type I AGN are produced in the special region that is named as the broad line region (BLR). Unfortunately, the structure and kinematics of BLR remain unclear. Really, broad emission lines are emitted in the vicinity of SMBH in AGN, but this region is not resolved in interferometric observations. Nevertheless, the properties of the broad emission lines are used to estimate the mass of the central SMBH.

The commonly accepted method for estimating the SMBH mass is to use the virial theorem. It allows to get the following relation [1, 2]:

$$M_{BH} = f \frac{R_{BLR} V_{BLR}^2}{G}, \quad (1)$$

¹ Central Astronomical Observatory at Pulkovo, St. Petersburg, Russia

where M_{BH} is the mass of a black hole, f is a virial parameter that defines the geometry, velocity field and orientation of BLR, R_{BLR} is the radius of BLR and V_{BLR} is the velocity dispersion that is usually measured as the full width of the emission line at a half of height in the radiation spectrum, i.e. FWHM. The BLR radius R_{BLR} is usually determined by the reverberation method, i.e. with time delay between continuum and emission line variations.

Determination of the f value is strongly depending on accepted BLR model. Labita et al. [3] found that the model of an isotope BLR fails to reproduce the observed line widths and shapes. They claimed that a disk model is preferred. A disk-like geometry of the BLR has been proposed by several authors [4]. Collin et al. [5] suggested that the disk may have a finite half thickness H , or a profile with H increasing more than linearly with the disk radius. Other models propose the existence of warped disks [6].

The authors of [7] and [8] found that the hydrogen lines are emitted in a more flattened BLR configuration in comparison to the highly ionized lines. They estimated the ratios of H/R in BLR for a number of AGNs and obtained the interval of $H/R \sim 0.07\text{--}0.5$. Also Pancoast et al. [9] found that the geometry of the BLR is generally a thick disk viewed close to face on. Eracleous and Halpern [10] have found that the inclination angle of BLR is $24\text{--}30^\circ$. Eracleous et al. [11] estimated the inclination angle of the BLR as $i = 19\text{--}42^\circ$. It is interesting to note that the polarimetric observations do not contradict these estimates [12, 13, 14].

The virial coefficient f depends strongly on the BLR geometry, velocity field and orientation. Usually the authors used the value $f \approx 1$. Peterson and Wandel [15] used $f = 3/4$. Onken et al. [16] suggested to use the mean value of the virial coefficient $f = 1.4$. McLure and Dunlop [17] have shown that for a disk inclined at an inclination angle i the virial coefficient value is

$$f = \frac{1}{4 \sin^2 i}. \quad (2)$$

Collin et al. [5] have considered the situation when the opening angle of the BLR disk should be large, i.e. $\Omega/4\pi \geq 0.1$. It means that the half thickness H of the disk should be large enough and the ratio of H to the radius R should be larger than $H/R = 0.1$. As a result, the virial coefficient has a form:

$$f = \frac{1}{4[(H/R)^2 + \sin^2 i]}. \quad (3)$$

This way, the relation (2) is a particular case of Eq. (3).

We adopted the disk-like model for the BLR of a number of Seyfert galaxies and, therefore, will use the expression for the virial coefficient f given by Eq. (2). The required value of the inclination angle can be determined from polarimetric observations using the standard Chandrasekhar–Sobolev theory [18, 19] of multiple scattering of the radiation on free electrons and Rayleigh scattering on gas molecules and small dust particles. According to these classical works, the polarization degree of scattered radiation depends strongly on the inclination

angle. The scattered radiation has the maximum linear polarization $P_l = 11.7\%$ when the line of sight is perpendicular to the normal to the semi-infinite atmosphere (Milne problem). Chandrasekhar [18] and Sobolev [19] presented the solution of this Milne problem. They have considered the multiple scattering of light in optically thick flattened atmospheres. The Milne problem corresponds to the propagation and scattering of light in optically thick disk-like region, i.e. this solution can be directly applied to BLR problem.

2 Polarimetric determining of the virial coefficient

We use the theory of multiple scattering of polarized radiation [18, 19, 20] and the disk-like model for the BLR.

We take into account the process of absorption of radiation. In this case the degree of polarization depends on the parameter $q = \sigma_a/(\sigma_a + \sigma_{SC})$, where σ_a is the cross-section of intrinsic absorption and σ_{SC} is the scattering cross-section. For the standard accretion disk model $\sigma_{SC} = \sigma_{Th}$, where $\sigma_{Th} = 6.65 \times 10^{-25} \text{ cm}^2$ is the cross-section for scattering of radiation on electrons, which in the non-relativistic case is the classical Thomson scattering cross-section. For some cases it is convenient to use the analytical formula for the polarization degree $P_l(\mu)$ obtained by Silant'ev et al. [21]. Using Eq. (2), we can obtain the values of the polarization degree and their dependence of the virial coefficient f . The results of these calculations are presented in Table 1.

For the model of a disk shaped BLR, the sine of the inclination angle is determined by [22]

$$\sin i = \frac{1}{2} \left(\frac{R_{BLR}}{R_g} \right)^{1/2} \frac{FWHM}{c}, \quad (4)$$

where i is the inclination angle, R_{BLR} is the radius of the BLR, $FWHM$ is the full width half maximum of a given line, which can be measured directly, c is the speed of light, $R_g = GM_{BH}/c^2$ is the gravitational radius. The value of $R_{BLR}V_{BLR}^2/G$ is called the ‘‘virial product’’ (VP). This quantity is based on two observable quantities: BLR radius and emission line width and has units of mass. The VP corresponds to the quantity of the virial coefficient $f = 1$ and with accordance to Eq. (2) corresponds to the inclination angle $i = 30^\circ$. According to [18] and [19], it means that the observed BLR emission polarization is $P_l(\mu) = 0.43\%$.

Equation (2) has been used for determining the virial coefficient. The polarimetric data that are necessary for determining the value of the inclination angle and the virial coefficient are presented in the spectropolarimetric atlas of Smith et al. [12]. They obtained the values of polarization degree and position angle for 36 Type 1 Seyfert galaxies during a number of different runs at the Anglo-Australian and William Herschel telescopes. From 36 objects presented in [12] 13 AGNS have the equal polarization degree values for H_α line and continuum. Also these objects have equal values of the position angle with the error limits. For most of the observed objects, there is a difference between

Table 1: Polarization degree P_l [%] dependence on q and μ , f is virial coefficient

μ	f	$q = 0.0$	$q = 0.01$	$q = 0.05$	$q = 0.1$	$q = 0.2$	$q = 0.3$
0.000	0.2500	11.713	12.592	16.074	20.349	28.636	36.642
0.025	0.2502	10.041	10.937	14.488	18.852	27.324	35.516
0.050	0.2506	8.986	9.889	13.473	17.879	26.440	34.723
0.075	0.2514	8.150	9.057	12.656	17.085	25.691	34.019
0.100	0.2525	7.449	8.357	11.961	16.395	25.015	33.354
0.125	0.2540	6.844	7.751	11.349	15.776	24.382	32.704
0.150	0.2558	6.312	7.215	10.799	15.209	23.776	32.056
0.175	0.2579	5.838	6.735	10.297	14.679	23.187	31.403
0.200	0.2604	5.410	6.301	9.834	14.178	22.607	30.737
0.225	0.2633	5.022	5.904	9.401	13.699	22.031	30.056
0.250	0.2667	4.667	5.539	8.994	13.237	21.455	29.356
0.275	0.2705	4.342	5.201	8.608	12.789	20.876	28.636
0.300	0.2747	4.041	4.887	8.240	12.352	20.291	27.895
0.325	0.2795	3.762	4.594	7.887	11.922	19.700	27.132
0.350	0.2849	3.502	4.318	7.547	11.498	19.100	26.346
0.375	0.2909	3.260	4.059	7.217	11.078	18.491	25.538
0.400	0.2976	3.033	3.813	6.897	10.660	17.872	24.707
0.425	0.3051	2.820	3.581	6.584	10.244	17.242	23.854
0.450	0.3135	2.620	3.359	6.278	9.829	16.602	22.979
0.475	0.3228	2.431	3.148	5.977	9.414	15.950	22.083
0.500	0.3333	2.252	2.947	5.681	8.997	15.287	21.166
0.525	0.3451	2.083	2.753	5.389	8.580	14.612	20.230
0.550	0.3584	1.923	2.568	5.100	8.160	13.926	19.275
0.575	0.3735	1.771	2.389	4.813	7.737	13.230	18.302
0.600	0.3906	1.627	2.217	4.529	7.312	12.522	17.312
0.625	0.4103	1.489	2.050	4.246	6.883	11.803	16.306
0.650	0.4329	1.358	1.889	3.965	6.452	11.074	15.285
0.675	0.4592	1.233	1.732	3.684	6.016	10.335	14.250
0.700	0.4902	1.113	1.580	3.404	5.577	9.586	13.202
0.725	0.5270	0.998	1.433	3.124	5.135	8.828	12.143
0.750	0.5714	0.888	1.289	2.844	4.688	8.061	11.072
0.775	0.6260	0.783	1.148	2.563	4.237	7.285	9.992
0.800	0.6944	0.682	1.011	2.282	3.782	6.502	8.903
0.825	0.7828	0.585	0.876	2.001	3.323	5.710	7.807
0.850	0.9009	0.492	0.744	1.719	2.861	4.912	6.704
0.875	1.0667	0.402	0.615	1.435	2.394	4.107	5.595
0.900	1.3158	0.316	0.488	1.151	1.923	3.296	4.482
0.925	1.7316	0.233	0.363	0.865	1.448	2.479	3.365
0.950	2.5641	0.152	0.240	0.578	0.969	1.658	2.245
0.975	5.0633	0.075	0.119	0.290	0.486	0.831	1.123
1.000	—	0.000	0.000	0.000	0.000	0.000	0.000

the values of polarization degree and the position angle. This phenomenon can testify to the difference in the inclination between the disk shaped BLR and the accretion disk that can be described by Shakura–Sunyaev model [23]. Continuum polarization degree of AGN from Palomar–Green catalog has been measured on 6 m telescope of Special Astrophysical Observatory [14].

Some results for the virial coefficient f are presented in Table 1 of our paper [24]. In the second column of this table the values for the BLR inclination angles are presented. These data are obtained from polarimetric data derived by Smith et al. [12]. The values of inclination angles have been obtained with use of the standard Chandrasekhar–Sobolev theory of multiple scattering of polarize radiation in the disk-like electron atmosphere and with use of Eq. (4). The virial factor for most of data in Table 1 from [24] corresponds to $f \sim 1$ within error limits, in accordance with [25]. For some objects, including Mrk 841, Mrk 896, Mrk 976, NGC 3516, NGC 3783 and NGC 5548, the virial coefficient is close to the mean value of $f = 1.4$ [16].

For a number of objects, including Fairall 51, Mrk 6, MC 1849.2-78.32, NGC 6814, UGC 3478 and WAS 45, their inclination angle exceeds considerably the value of $i = 30^\circ$. It means that their virial factor $f < 1.0$. This situation corresponds better to the BLR model of random orbits.

3 Determining SMBH masses

Equation (1) allows to derive the SMBH mass if the virial coefficient is known. The observed full width of emission lines is presented in [1, 26, 27, 28]. The radius R_{BLR} is estimated usually by the reverberation mapping that is related to the continuum monochromatic luminosity λL_λ . An increasing body of measurements is now available for H_β time lags [29, 30, 4, 31]. For example, from Bentz et al [31] one can obtain the following estimate for R_{BLR} :

$$\log(R_{BLR}/1 \text{ ltd}) = K + \alpha \log \frac{\lambda L_\lambda(5100 \text{ \AA})}{10^{44} \text{ erg/s}}, \quad (5)$$

where $K = 1.527_{-0.03}^{+0.031}$, $\alpha = 0.533_{-0.039}^{+0.035}$ and R_{BLR} is measured in light days (ltd).

Equation (5) allows to present the BLR radius in the form

$$R_{BLR} = 10^{16.94} \left(\frac{\lambda L_\lambda(5100 \text{ \AA})}{10^{44} \text{ erg/s}} \right)^{0.533}. \quad (6)$$

Then, using Eqs. (2) and (4), one can get the values of the SMBH masses. The value of $\sin i$ can be derived from the data on the degree of polarization that is strongly dependent on the inclination angle.

The results of our calculations of the SMBH masses are presented in Table 2 [24]. In the last column of this table the published values for SMBH masses are presented. There is a difference for a number of objects. For example, for Fairall 9 our estimate of the SMBH mass looks lower, but our upper

Table 2: The masses of SMBH in AGNs determined via measured polarization of broad H_α emission

Object	M_{BH}/M_\odot (observations)	M_{BH}/M_\odot (literature)
Akn 120	$(3.23^{+0.44}_{-0.32}) \times 10^8$	$(4.49 \pm 0.93) \times 10^8$
Akn 564	$(1.2^{+0.94}_{-0.49}) \times 10^6$	$\sim 1.1 \times 10^6$
Fairall 9	$(1.34^{+0.76}_{-0.36}) \times 10^8$	$(2.55 \pm 0.56) \times 10^8$
I Zw 1	$10^{7.6 \pm 0.17}$	$10^{7.441^{+0.093}_{-0.119}}$
Mrk 6	$(1.09^{+0.37}_{-0.25}) \times 10^8$	$(1.36 \pm 0.12) \times 10^8$
Mrk 279	$(8.13^{+1.24}_{-1.26}) \times 10^7$	$(15.2^{+3.25}_{-3.18}) \times 10^7$
Mrk 290	$(3.94 \pm 0.19) \times 10^7$	$(2.43 \pm 0.37) \times 10^7$
Mrk 304	$10^{8.4^{+0.09}_{-0.02}}$	$10^{8.511^{+0.093}_{-0.113}}$
Mrk 335	$(1.56^{+0.19}_{-0.15}) \times 10^7$	$(1.42 \pm 0.37) \times 10^7$
Mrk 509	$(1.35 \pm 0.12) \times 10^8$	$(1.39 \pm 0.12) \times 10^8$
Mrk 705	$10^{7.07^{+0.11}_{-0.09}}$	$10^{6.79 \pm 0.5}$
Mrk 841	$10^{8.55 \pm 0.1}$	$10^{8.523^{+0.079}_{-0.052}}$
Mrk 871	$10^{7.04^{+0.09}_{-0.06}}$	$10^{7.08 \pm 0.5}$
Mrk 876	$10^{8.57^{+0.19}_{-0.52}}$	$10^{9.139^{+0.096}_{-0.122}}$
Mrk 896	$10^{7.07 \pm 0.06}$	$10^{7.01}$
Mrk 926	$10^{8.8^{+0.19}_{-0.11}}$	$10^{8.36 \pm 0.02}$
Mrk 985	3.18×10^7	5.71×10^7
NGC 3516	$10^{8.06 \pm 0.27}$	$10^{7.88^{+0.04}_{-0.03}}$
NGC 3783	$10^{7.7 \pm 0.11}$	$10^{7.47^{+0.07}_{-0.09}}$
NGC 4051	$(1.64^{+0.67}_{-0.55}) \times 10^6$	$(1.58^{+0.50}_{-0.65}) \times 10^6$
NGC 4593	$(8.25^{+3.46}_{-3.06}) \times 10^6$	$(9.8 \pm 2.1) \times 10^6$
NGC 5548	$(7.84^{+0.53}_{-0.46}) \times 10^7$	$(7.827 \pm 0.017) \times 10^7$
NGC 6104	$10^{7.16^{+0.09}_{-0.08}}$	$10^{7.39}$
NGC 6814	$10^{6.94^{+0.077}_{-0.09}}$	$10^{7.02 \pm 0.5}$
NGC 7213	$10^{6.83^{+0.84}_{-0.33}}$	$10^{6.88 \pm 0.5}$
NGC 7469	$10^{7.54^{+0.17}_{-0.22}}$	$10^{7.19 \pm 0.13}$
PG 1211+143	$10^{8.34^{+0.29}_{-0.20}}$	$10^{7.961^{+0.082}_{-0.101}}$

limit value coincides with the low order limit value of BH mass obtained by Reynolds [32]. For Ark 120 the situation looks the same: there is a coincidence between our estimated value and the low order value of BH mass obtained by Vestergaard and Peterson [1]. The similar situation occurs also for NGC 3516, NGC 3783, NGC 5548, and Mrk 279. The extreme case is Mrk 290. Our low order estimate appears 1.34 times higher than the upper limit of BH mass presented by Feng et al. [28].

This difference between our and other estimates of mass values for some black holes can be associated with the real determination of the virial coefficient f from the Eq. (1). Value of virial coefficient from the papers [17, 25] allows us

to determine this parameter directly from Eq. (2) but only in the situation when the inclination angle of the BLR is certain. Polarimetric observations have preference because the value of polarization degree is directly associated with the inclination angle value, especially for standard Chandrasekhar–Sobolev theory of the generation of polarization in the plane-parallel atmosphere. Other methods for determination of inclinations of BLRs and accretion disks are considerably uncertain. Unfortunately, the size of the BLR cannot be directly measured from single epoch spectra, which are used for estimation of BH masses. Most popular estimates of BLR size rely on the R_{BLR} scales with a certain power of continuum luminosity of the AGN.

4 Determining recoiling velocities of black holes ejected by gravitational radiation in galaxy mergers

We demonstrate that polarimetric observations allow to derive the recoiling velocity of black hole ejected by gravitational radiation produced in the process of black holes merging. Really merging of spinning black holes can produce recoil velocities (“kicks”) of the final merged black holes via anisotropic gravitational radiation up to several thousands km/s [33, 34, 35]. The basic feature of the gravitational wave (GW) recoil effect is the situation when the SMBH spends a significant fraction of time off nucleus at scales beyond that of the molecular obscuring torus. For example, according to [36], isophotal analysis of M87, using data from Advanced Camera for Surveys, reveals a projected displacement of 68 ± 0.8 pc ($\sim 0.''1$) between the nuclear point source and the photo-center of the galaxy itself.

It is very important that a recoiling SMBH in an AGN retains the inner part of its accretion disk. Bonning et al. [37] have shown that the accretion disk will remain bound to the recoiling BH inside the radius $R_{out} = 1.3 \times 10^{18} M_8/V_3^2$ cm ($M_8 = M_{BH}/10^8 M_\odot$, $V_3 = V/10^3$ km/s), where the orbital velocity V is equal to the recoil velocity V_K . In this case the retained disk mass appears less than the BH mass because of stability requirement [33].

If we suggest that $R_{BLR} \approx R_K$, we obtain the following relation instead of Eq. (4):

$$\sin i = 0.492 \left(\frac{FWHM}{V_K} \right). \quad (7)$$

In this case, when $FWHM = 1500$ km/s and $V_K = 10^3$ km/s, we obtain $P_l(H_\beta) = 1.24\%$. For $V_K = 3 \times 10^3$ km/s, we obtain $P_l(H_\beta) = 0.1\%$. According to [38], for merging black hole with spin value $a = 1.0$, the kick velocity has magnitude of $V_K = 4925.94$ km/s. For $FWHM = 5 \times 10^3$ km/s the polarization degree is $P_l(H_\beta) = 0.624\%$. For H_α emission line, the values of polarization degree are practically the same because of the practical equality of FWHMs [39].

According to [33], the accretion disk remains bound to the ejected BH within the region where the accreting matter orbital velocity is larger than the ejection

speed. For example, the ejected disk of $10^7 M_\odot$ BH has a characteristic size of tens of thousands of Schwarzschild radii and an accretion lifetime of $\sim 10^7$ years. But in this case the ejected BH could traverse a considerable distance and appears as an off-center galaxy region. Loeb [33] claimed that only small fraction of all quasars could be associated with an escaping SMBH.

Equation (7) allows us to find the candidates for escaping BHs. According to [40] and [5], the virial coefficient can be presented in the form

$$f = \frac{1}{4 \left[\left(\frac{V_K}{V_{orb}} \right)^2 + \sin^2 i \right]}. \quad (8)$$

In this case Eq. (4) is transforming in the expression

$$\sqrt{\left(\frac{V_K}{V_{orb}} \right)^2 + \sin^2 i} = \frac{FWHM}{2c} \left(\frac{R_{BLR}}{R_g} \right)^{1/2}. \quad (9)$$

The value of $\sin i$ can be obtained from polarimetric observations, naturally if we use the theory of multiple scattering of polarized radiation developed by Chandrasekhar and Sobolev. If we consider the situation $R_K \approx R_{BLR}$ and $V_K < V_{orb}$, we obtain instead of Eq. (7) the following relation:

$$\sqrt{\left(\frac{V_K}{V_{orb}} \right)^2 + \sin^2 i} = 0.492 \left(\frac{FWHM}{V_K} \right). \quad (10)$$

For example, for $V_K = 0.5 V_{orb}$, $\sin i = 0.847$, that corresponds to $P_l(\mu) = 2.05\%$. We estimated the values of kick velocity from a number of AGN using the polarimetric data from [12] and estimates of R_{BLR} obtained in [41]. For estimates of M_{BH} , we used the relation (6) from [1].

As a result we obtained the following estimates of the recoiling velocities: $V_K = 0.22 V_{orb}$ for Ark 120 and Mrk 279, $V_K = 0.42 V_{orb}$ for NGC 3516, $V_K = 0.288 V_{orb}$ for NGC 3783, $V_K = 0.31 V_{orb}$ for NGC 4593. It is interesting that for NGC 4051 the situation occurs when $V_K \approx V_{orb}$.

Of course, our results have a preliminary character, because another situation can be considered when the coefficient $A = H/R$, where H is the geometrical thickness of the BLR [5]. It means that the BLR is the geometrically thick accretion disk compared with the geometrically thin accretion disk that provides the continuum polarization.

5 Conclusions

We demonstrated that V.V. Sobolev and S. Chandrasekhar theory of the multiple scattering of polarized radiation is an efficient instrument for an analysis and interpretation of the polarimetric data of AGNs. The virial theorem accepted to a disk-like configuration of BLR in AGN allows us to determine the real mass of AGN if the inclination angle of the accretion flow is known. Namely,

the polarimetric observations allow us to derive the inclination angle itself using the theory for the generation of polarized radiation developed by Sobolev and Chandrasekhar. As a result we have demonstrated the possibility of polarimetric determining of the virial coefficient and, as the final result, determining the mass of SMBH in AGN. In principle, polarimetric observations allow us to derive the recoil velocity of a black hole ejected by gravitational radiation as a result of a galaxy merger.

Acknowledgments. This research was supported by the Basic Research Program P-7 of Presidium of RAS and the program of the Department of Physical Sciences of RAS No. 2.

References

1. *M. Vestergaard, B.M. Peterson*, *Astrophys. J.*, **641**, 689, 2006.
2. *S. Fine, S.M. Croom, P.F. Hopkins et al.*, *Mon. Not. Roy. Astron. Soc.*, **390**, 1413, 2008.
3. *M. Labita, A. Treves, R. Falomo, M. Uslenghi*, *Mon. Not. Roy. Astron. Soc.*, **373**, 551, 2006.
4. *R. Decarli, M. Labita, A. Treves, R. Falomo*, *Mon. Not. Roy. Astron. Soc.*, **387**, 1237, 2008.
5. *S. Collin, T. Kawaguchi, B.M. Peterson, M. Vestergaard*, *Astron. Astrophys.*, **456**, 75, 2006.
6. *S. Tremaine, S.W. Davis*, *Mon. Not. Roy. Astron. Soc.*, **441**, 1408, 2014.
7. *W. Kollatschny, M. Zetzl, M. Dietrich*, *Astron. Astrophys.*, **454**, 459, 2006.
8. *W. Kollatschny, M. Zetzl*, *Astron. Astrophys.*, **558**, A26, 2013.
9. *A. Pancoast, B.J. Brewer, T. Treu, LAMP2008 Collaboration, LAMP2011 Collaboration*, *Amer. Astron. Soc. Meet. Abstr.*, **221**, 309.08, 2013.
10. *M. Eracleous, J.P. Halpern*, *Astrophys. J. Suppl.*, **90**, 1, 1994.
11. *M. Eracleous, J.P. Halpern, M. Livio*, *Astrophys. J.*, **459**, 89, 1996.
12. *J.E. Smith, S. Young, A. Robinson et al.*, *Mon. Not. Roy. Astron. Soc.*, **335**, 773, 2002.
13. *J.E. Smith, A. Robinson, D.M. Alexander et al.*, *Mon. Not. Roy. Astron. Soc.*, **350**, 140, 2004.
14. *V.L. Afanasiev, N.V. Borisov, Y.N. Gnedin et al.*, *Astron. Lett.*, **37**, 302, 2011.
15. *B.M. Peterson, A. Wandel*, *Astrophys. J. Lett.*, **521**, L95, 1999.
16. *C.A. Onken, L. Ferrarese, D. Merritt et al.*, *Astrophys. J.*, **615**, 645, 2004.
17. *R.J. McLure, J.S. Dunlop*, *Mon. Not. Roy. Astron. Soc.*, **327**, 199, 2001.
18. *S. Chandrasekhar*, *Radiative Transfer*. Oxford: Clarendon Press, 1950.

19. *V.V. Sobolev*, A Treatise on Radiative Transfer. Princeton: Van Nostrand, 1963.
20. *N.A. Silant'ev*, *Astron. Astrophys.*, **383**, 326, 2002.
21. *N.A. Silant'ev*, *M.Y. Piotrovich*, *Y.N. Gnedin*, *T.M. Natsvlishvili*, *Astron. Rep.*, **54**, 974, 2010.
22. *B. Agís-González*, *G. Miniutti*, *E. Kara et al.*, *Mon. Not. Roy. Astron. Soc.*, **443**, 2862, 2014.
23. *N.I. Shakura*, *R.A. Sunyaev*, *Astron. Astrophys.*, **24**, 337, 1973.
24. *M.Y. Piotrovich*, *Y.N. Gnedin*, *N.A. Silant'ev et al.*, *Mon. Not. Roy. Astron. Soc.*, **454**, 1157, 2015.
25. *R.J. McLure*, *M.J. Jarvis*, *Mon. Not. Roy. Astron. Soc.*, **337**, 109, 2002.
26. *L.C. Ho*, *J. Darling*, *J.E. Greene*, *Astrophys. J. Suppl.*, **177**, 103, 2008.
27. *J.-G. Wang*, *X.-B. Dong*, *T.-G. Wang et al.*, *Astrophys. J.*, **707**, 1334, 2009.
28. *H. Feng*, *Y. Shen*, *H. Li*, *Astrophys. J.*, **794**, 77, 2014.
29. *S. Kaspi*, *P.S. Smith*, *H. Netzer et al.*, *Astrophys. J.*, **533**, 631, 2000.
30. *M.C. Bentz*, *B.M. Peterson*, *H. Netzer et al.*, *Astrophys. J.*, **697**, 160, 2009.
31. *M.C. Bentz*, *K.D. Denney*, *C.J. Grier et al.*, *Astrophys. J.*, **767**, 149, 2013.
32. *C.S. Reynolds*, *Space Sci. Rev.*, **183**, 277, 2014.
33. *A. Loeb*, *Phys. Rev. Lett.*, **99**, 041103, 2007.
34. *G.A. Shields*, *E.W. Bonning*, *Astrophys. J.*, **682**, 758, 2008.
35. *S. Komossa*, *D. Merritt*, *Astrophys. J. Lett.*, **689**, L89, 2008.
36. *D. Batcheldor*, *A. Robinson*, *D.J. Axon et al.*, *Astrophys. J. Lett.*, **717**, L6, 2010.
37. *E.W. Bonning*, *G.A. Shields*, *S. Salviander*, *Astrophys. J. Lett.*, **666**, L13, 2007.
38. *C.O. Lousto*, *Y. Zlochower*, *Phys. Rev. Lett.*, **107**, 231102, 2011.
39. *J.E. Greene*, *L.C. Ho*, *Astrophys. J.*, **630**, 122, 2005.
40. *X.-B. Wu*, *J.L. Han*, *Astrophys. J. Lett.*, **561**, L59, 2001.
41. *J.E. Greene*, *C.E. Hood*, *A.J. Barth et al.*, *Astrophys. J.*, **723**, 409, 2010.

Black Holes in Binary Systems and Nuclei of Galaxies

A.M. Cherepashchuk¹

E-mail: *Cherepashchuk@gmail.com*

During last 45 years, a big progress has been achieved in observational investigations of stellar mass black holes in X-ray binary systems and supermassive black holes in galactic nuclei. Masses of several dozens of stellar mass black holes ($M_{BH} = 4 \div 20M_{\odot}$) as well as many hundreds of supermassive black holes ($M_{BH} = 10^6 \div 10^{10}M_{\odot}$) were measured. Recent discovery of gravitational waves from a binary black hole merger opens new era in investigations of black holes.

1 Introduction

In the last 45 years, following pioneering papers by Ya.B. Zeldovich [1] and E.E. Salpeter [2] in which powerful energy release from non-spherical accretion of matter onto black holes (BH) was predicted, many observational investigations of BHs in the Universe have been carried out. To date, the masses of several dozens stellar-mass BH ($M_{BH} = 4 \div 20M_{\odot}$) in X-ray binary systems and many hundreds supermassive BH ($M_{BH} = 10^6 \div 10^{10}M_{\odot}$) in galactic nuclei have been measured. The estimated radii of these massive and compact objects do not exceed several gravitational radii.

Observations suggest (taking into account observational selection effects) that the number of stellar-mass BHs ($M = 8 \div 10M_{\odot}$) in our Galaxy amounts to at least 10^7 or 0.1% of the baryonic matter. A great discovery was made recently by American gravitational wave antennas LIGO1 and LIGO2: gravitational waves were detected from a binary black hole merger GW150914 [3].

Black holes are derived from the collapse of massive objects. According to modern concepts taking into account general relativity effects, if the mass of the stellar core where thermonuclear burning occurs exceeds $3M_{\odot}$ the gravitational core collapse results in the formation of a BH. If the mass of the stellar core is less than $3M_{\odot}$, the stellar evolution ends up with the formation of neutron star or a white dwarf.

A black hole is an object (more precisely, a space-time region) with such a strong gravitational field that no signal, including light, can escape from it to the space infinity. Characteristic dimension of BH is given by the gravitational (Schwarzschild) radius: $r_g = 2GM/c^2$, where M is the mass of the object, G is the Newtonian constant of gravitation, and c is the speed of light in vacuum.

¹ Lomonosov Moscow State University, Sternberg Astronomical Institute, Russia

In this review, we describe the present-day observational status of BHs and discuss further prospects for studies of these extreme objects.

2 Stellar-mass black holes in X-ray binary systems

Black holes can be found in X-ray binary systems ($M_{BH} = 4 \div 20M_{\odot}$), and in galactic nuclei ($M_{BH} = 10^6 \div 10^{10}M_{\odot}$).

After the great discovery of gravitational waves [3], it is clear that black holes can be found also in BH+BH and BH+NS binary systems (here BH is black hole, NS is neutron star).

An X-ray binary consists of a normal optical star (the donor of matter) and relativistic object, a neutron star or black hole, which accretes matter from its companion. To date, specialized X-ray satellites (Uhuru, Einstein, Rosat, Mir-Kvant, Granat, Ginga, Chandra, XMM-Newton, Integral, etc.) have discovered more than one thousand X-ray binaries, which serve as a powerful tool in the detection and studies of stellar-mass BHs. The theory of disk accretion was developed in 1972–1973 in papers by Shakura and Sunyaev [4], Pringle and Rees [5], Novikov and Thorne [6].

X-ray and optical observations of X-ray binary systems perfectly complement each other. X-ray observations from space vehicles allow one to foresee the presence of a compact object in a binary system, while measurements of rapid X-ray time variability on timescales Δt as short as 10^{-3} s provide an estimate the characteristic size of a compact star: $r \leq c\Delta t$. These estimates imply that the sizes of compact X-ray sources never exceed several gravitational radii. At the same time, spectral and photometric observations by ground-based optical telescopes enable us to study the motion of the normal star in an X-ray binary system and to deduce using the star as a “test body”, the mass of BH or neutron star from Newton’s law of gravitation. A great contribution to the theory of absorption and emission lines formation in the stellar atmospheres was done by Sobolev [7]. If the measured mass of an X-ray source exceeds $3M_{\odot}$, it can be considered as a BH candidate. Just this determines the strategy of searching for stellar-mass BHs in binary systems.

The first optical identifications of X-ray binary systems and studies of their optical manifestations (ellipticity and reflection effects) were carried out in 1972–1973 and reported in papers [8]–[11]. Based on these studies, reliable methods of estimating the BH masses in X-ray binaries were developed.

Methods of interpreting light curves, line profiles and radial velocity curves of X-ray binaries were developed by assuming that the optical star has an ellipsoidal or pear-like shape in the framework of Roche model with a complex surface temperature distribution due to gravitational darkening and X-ray heating effects [12]. To date, some scientific groups (from USA, the UK, Germany, Netherlands, France, Russia and some other countries) have measured the masses of 26 stellar-mass BHs ($M_{BH} = 4 \div 20M_{\odot}$), as well as the masses of ~ 70 neutron stars ($M_{NS} \approx 1 \div 2M_{\odot}$) in binary systems (see Fig. 1).

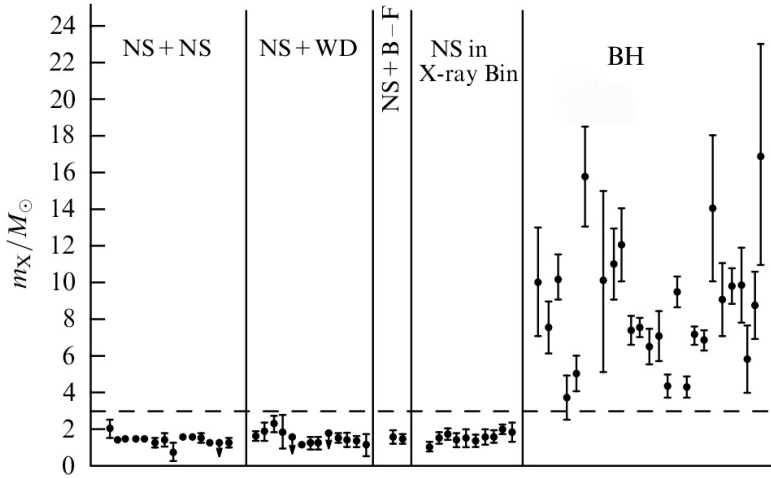


Figure 1: Measured masses of neutron stars and black holes in binary stellar systems: NS+NS – binary radio pulsars with neutron stars, NS+WD – binary radio pulsars with white dwarfs, NS+B–F – binary radio pulsars with an optical non-degenerate stars of the B–F spectral class, NS in X-ray Bin – binary X-ray pulsars. The dashed horizontal line shuts off the value of $3M_{\odot}$ being the absolute upper limit of neutron star mass predicted by GR.

The measured masses of neutron stars lie within the range of $1 \div 2M_{\odot}$, with the mean mass being $\sim 1.4M_{\odot}$. Fine differences in various types of neutron stars have already been found. For example, the masses of rapidly rotating old neutron stars (spin period of about several ms) which have been recycled by accretion in close binary systems [13], are on average $\sim 0.15M_{\odot}$ higher than the masses of slowly rotating neutron stars (spin periods about several s) [14]. This inference is consistent with theoretical predictions [15].

All neutron stars with measured masses demonstrate clear signatures of their observable surfaces – they are either radio pulsars, X-ray pulsars or type I X-ray bursters.

Thus, in all ~ 70 cases where a compact object demonstrates clear signatures of an observable surface, its measured mass ranges $1 \div 2M_{\odot}$ and does not exceed $3M_{\odot}$, in full agreement with the GR prediction of the existence of an upper mass limit $3M_{\odot}$ for neutron stars.

The measured masses of 26 BH candidates fall within the range ($M_{BH} = 4 \div 20M_{\odot}$) with the mean mass being of order $9M_{\odot}$. As BHs have no observable surface, they should not show up as a radio pulsar, X-ray pulsar, or type I X-ray burster. This is indeed the case for 26 BH candidates: none (!) of these massive ($M > 3M_{\odot}$), compact (radii do not exceed a few r_g) X-ray sources has shown evidence of radio pulsar, X-ray pulsar, or type I X-ray burster.

All of them demonstrate only irregular or quasi-periodic (but not strictly periodic) X-ray emission variability down to timescales as short as $\sim 10^{-3}$ s. In the model which takes into account oscillation of the inner parts the accretion

disk or the orbital motion of hot spots in the inner parts of the disk, it is possible to show (e.g., [16]) that such a rapid X-ray variability of BH candidates is due to their very small sizes not exceeding several gravitational radii.

Thus, a remarkable result gradually emerges with the increasing bulk of information on the masses of relativistic objects: neutron stars and BH candidates differ not only in masses, but also in other observational manifestations, in full agreement with GR.

New results have recently been obtained in studies of the rotation of stellar-mass BHs. The possibility of determining the angular momentum of a BH stems from the fact that if BH co-rotates with the accretion disk, the inner edge of the disk comes much closer to the BH than in the case of a non-rotating BH, since the radius of the event horizon of a rotating BH is smaller than that of a non-rotating BH.

The measured values of dimensionless angular momentum of stellar mass BH lie within the range

$$a_* = 0.98 \text{ (system GRS1915+105)} \div 0.12 \text{ (system A0620-00)}. \quad (1)$$

A remarkable result was recently obtained by Narayan and McClintock [17]. They found a correlation between the observed radio fluxes from collimated jets from accreting BHs, P_{jet} , and the value of dimensionless angular momentum a_* of the BHs: $P_{jet} \sim a_*^2$. This is the first observational evidence that the relativistic jets from accreting stellar-mass BHs can be generated from the conversion of the rotational energy of BH into the kinetic energy of regular bulk motion of matter in collimated relativistic jets with outflow velocities close to the speed of light. Here, the well-known Blandford–Znajek mechanism seems to be operative [18].

Relativistic collimated jets are observed in many X-ray binary systems (most spectacular example is the SS433 binary system, e.g., [19, 20]). Studies of X-ray binaries with relativistic collimated jets, called microquasars, are of special interest, since the physical processes in microquasars are microscopic versions of processes occurring in quasars – very active galactic nuclei, as well as in the nuclei of other galaxies.

3 Supermassive black holes in galactic nuclei

The first estimates of the masses of supermassive BHs (SMBHs) in quasars were made as early as 1964 in the pioneering paper by Zeldovich and Novikov [21] under reasonable assumption that the quasar luminosity is close to the critical Eddington luminosity.

Presently, the masses of SMBHs in galactic nuclei estimated by assuming that the motion of “test bodies” (gas disks, gas clouds, individual stars) near the SMBH is governed by the gravitational field of the central SMBH. In this case the mass of SMBH can be estimated by the formula

$$M_{BH} = \eta V^2 r / G, \quad (2)$$

where V is the velocity of the test body, r is its distance from the center of SMBH, G is the Newtonian constant of gravitation, $\eta \cong 1 \div 3$ is the factor that takes into account the character of test body motions around the central SMBH.

The two most reliable methods of SMBH mass determination in galaxy centers are the resolved kinematics method and reverberation mapping method.

The method of resolved kinematics is based on direct observations of the motion of test bodies (e.g., [22]). It can be applied to nearby galaxies, for which the telescope angular resolution allows “watching” the test bodies residing in the galactic nucleus and direct measurement of their velocities and distances from the central SMBH. For example, there is a SMBH with mass $(4.31 \pm 0.36) \times 10^6 M_\odot$ in the center of our Galaxy. The mass of this SMBH is determined with an accuracy of better than 10% from the motion of 28 stars orbiting it in elliptic orbit [23]. Using very long baseline radio interferometers, by resolved kinematics method the mass of the SMBH in the center of galaxy NGC4257 was reliably determined to be $M_{BH} = 3.9 \times 10^7 M_\odot$ [24]. For more detailed results of SMBH mass estimations by resolved kinematics methods using basically Hubble Space Telescope, see review by Kormendy and Ho [22].

Unfortunately, the angular resolution of telescopes for the most of remote galaxies is insufficient to directly see individual test bodies; in these cases, one has to apply the reverberation mapping method when estimating the mass of SMBHs. In this method, the velocities and distances of test bodies are estimated indirectly. In the case of active galactic nuclei the velocity V is estimated from Doppler width of emission lines formed in gas clouds, rotating around the central SMBH.

The characteristic distance r of the gas clouds from the central SMBH is determined from the time delay of the emission lines variability relative to that of the continuum spectrum, which is formed in the central parts of the galaxy nucleus.

The time delay between the variability in emission lines relative to the continuum in active galactic nuclei was discovered in 1970–1972 by Cherepashchuk and Lyutyi [25]. It turned out that although due to non-stationary processes in galactic nuclei both the lines and continuum change chaotically, a correlation is revealed between their changes: the line intensity variations repeat those of the continuum intensity with a time delay Δt , which in different galaxies varies from a week to several months. It was noted [25] that a comparatively high gas density in the clouds corresponding to broad components of emission lines implies a short gas recombination time, so the time delay Δt is basically the time of flight of hard emission photons, which are created near the central accreting source to the gas clouds – test bodies emitting spectral lines. Then, the characteristic distance from the test bodies to the central SMBH can be estimated using formula $r \cong c\Delta t$. The SMBH mass can ultimately be estimated from the known characteristic distance r and velocity V using formula (1). The reverberation mapping method for SMBH mass estimates has been widely applied to evaluate SMBH masses in active galactic nuclei.

There are also indirect, less reliable methods of SMBH mass estimates. These include, for instance, the use of widths and absolute intensities of emission lines in active galactic nucleus spectra (e.g., [26]), the empirical relation between SMBH mass and velocity dispersion of stars in the galactic central regions and kink frequency in the power spectra of X-ray irregular variability of galactic nuclei. Such methods enable a quick mass estimation of a large number of SMBHs, which is essential for statistical studies. As a rule, the results obtained with these indirect methods are calibrated by SMBH masses which were reliably measured using resolved kinematics and reverberation mapping methods.

To date, the masses of several hundreds SMBHs have been measured applying resolved kinematics and reverberation mapping methods. They all lie within the range of $10^6 \div 10^{10} M_{\odot}$. The most reliable mass estimates of SMBH in 44 elliptical and 41 spirals (see the recent review by Kormendy and Ho [22]) span the interval from $(0.94 \div 1.34) 10^6 M_{\odot}$ to $(0.49 \div 3.55) 10^{10} M_{\odot}$. Here, the values in parenthesis stand for the mass determination errors. Reliable values of mass of SMBHs and central star clusters were summarized recently by Zasov and Cherepashchuk [27] for 82 galaxies with known rotational velocities (i.e. with known total galactic masses, including the dark matter halo mass).

Indirect mass evaluations were made for many thousand SMBHs in active galactic nuclei. For example, the targeted spectrophotometric Sloan digital sky survey (SDSS) allowed about 60 000 SMBH mass in centers of quasars to be estimated by indirect method, and statistical dependence of SMBH masses on redshift to be constructed in the redshift range $z = 0.1 \div 4.5$ [28]. It turned out that on average the SMBH mass increases with redshift (i.e. with a decrease in the proper age of a quasar). This effect, if free of a strong observational selection, can hardly be explained in the framework of the model of an SMBH mass increase due to the accretion of circumnuclear matter in quasars.

But the most difficult question to explain relates to the discovery of more than a dozen quasars with very high redshifts $z = 6 \div 8$ (proper age of less than one billion years [29]). How could such massive ($M_{BH} = 10^8 \div 10^{10} M_{\odot}$) SMBHs be formed in a time of less than 10^9 years? This important observational fact poses a serious theoretical problem.

In recent years (e.g., [30]), the analysis of iron K_{α} line profiles in X-ray spectra of galactic nuclei has allowed the dimensionless angular momentum $a_* = cj/(GM_{BH}^2)$ to be estimated for some SMBHs. These parameters found to be less than the critical value of $a_* = 0.998$, in agreement with theoretical predictions [31]. The parameter a_* can be estimated also from the kinetic energy flux in relativistic jets from SMBH [32]. These estimates require the magnetic field value in the last stable orbit in the accretion disk or the SMBH event horizon to be known. Spectropolarimetric observations of the nuclei of active galaxies made by Gnedin group [33] allowed the values of parameter a_* to be estimated for a dozen SMBHs. The values found range from $a_* = 0.920 \div 998$ to $a_* = 0.550 \div 0.650$ and do not exceed the theoretical upper limit $a_* = 0.998$.

Limits on the radii of SMBHs are set by observations of fast variability of the optical, infrared and X-ray emission from some galactic nuclei on timescales smaller than tens of minutes. Strong but model-dependent constraints on the SMBH radii can be obtained by analyzing the broad X-ray profiles of the iron K_α emission line at 6.4 keV. The line width of this asymmetric profile corresponds to velocities as high as $\sim 10^5$ km/s. The analysis of this component in the galaxy MCG6–30–15 [34] implies that the inner edge of the accretion disk in this case is located at a distance smaller than $3r_g$ from central SMBH, possibly due to its rapid rotation.

In the last few years, direct measurements of the radii of SMBHs in the center of our Galaxy ($M_{BH} \cong 4.3 \times 10^6 M_\odot$) and galaxy M87 ($M_{BH} = 6 \times 10^6 M_\odot$) have been carried out using VLBI-interferometry at short wavelengths ($\lambda \cong 1.3$ mm) with an angular resolution close to 10^{-5} seconds [35, 36]. It is shown that the dimension of the SMBHs “shadow” at the center of the accretion flow is several gravitational radii ($r_g = 9.1 \times 10^{-6}$ arcseconds for SMBH in our Galaxy and $r_g = 7.8 \times 10^{-6}$ arcseconds for the SMBH in the galaxy M87). A great contribution to the problem of measuring the dimensions of SMBHs will be done by the space radiointerferometers RADIOASTRON and MILLIMETRON.

Accordingly to S.S. Doelman, international effort has been done recently to create an Event Horizon Telescope (EHT) through a millimeter wavelength VLBI network. The EHT is the global effort to carry out the investigations of BH “shadow” and strong gravity effects in the vicinity of the event horizon of SMBH. The Black Hole Cam team, along with groups from Taiwan, Japan, Chile, USA and Germany are all working within the EHT.

New results of measurement on EHT of linear polarization and intensity of radioemission on the scale about 6 gravitational radius for the supermassive black hole in the galaxy M87 have been published recently [37].

Thus, supermassive ($M_{BH} = 10^6 \div 10^{10} M_\odot$) and very compact objects (with sizes not exceeding several gravitational radii) have been discovered to date in the nuclei of many galaxies. All their features most likely suggest that they comprise black holes.

4 Demography of stellar-mass and supermassive black holes

Black hole demography studies the formation and growth of black holes and their evolutionary connection to other astrophysical objects – stars, galaxies, etc.

In the last few years, a close similarity has been established between the observational manifestations of BHs in X-ray binary systems and in galactic nuclei [38]. In particular, the statistical dependence, called the fundamental plane, was discovered for supermassive and stellar-mass BHs [39]

$$\lg L_r = (0.60_{-0.11}^{+0.11}) \lg L_x + (0.78_{-0.09}^{+0.11}) \lg M_{BH} + 7.33_{-4.07}^{+4.05}, \quad (3)$$

where L_r is the observed radio luminosity (mainly due to relativistic jet radio emission), L_x is the X-ray luminosity (from the accretion disk and the jet base), and M_{BH} is the black hole mass (for both stellar-mass BHs and SMBHs).

The variability of active galactic nuclei containing accreting supermassive BHs was related to be similar to that of accreting stellar-mass BHs in X-ray binary systems if the variability time is normalized depending on the BH mass [38].

In X-ray binaries with BHs, in addition to irregular variability there are two types of quasi-periodic (i.e., not strictly periodic) oscillations (QPO) of an X-ray flux: low frequency QPOs (LFQPOs) with the characteristic frequencies $0.1 \div 30$ Hz, and high-frequency QPOs (HFQPOs) with frequencies falling in the range of $40 \div 450$ Hz.

Quasi-periodic X-ray oscillations were recently discovered from accreting SMBHs in the nuclei of some galaxies. For example, QPOs with the characteristic period of about one hour were observed in the active nucleus of the galaxy REJ1034+396 [40]. With a central SMBH mass of about $10^7 M_\odot$, this quasiperiod corresponds to an orbit radius of about $3r_g$, which yields an upper limit on the size of this very massive and compact object, giving support to its BH nature.

Interesting results were obtained in studies of the mass distribution of stellar-mass BHs. It turned out that in binary systems there is no dependence of masses of relativistic objects on their companion masses. The neutron star and black hole mass distribution turned out to be unusual as well [41, 42], – see Fig. 2. The number of studied stellar-mass BHs does not increase with decreasing of their masses. This looks strange, since the stellar mass distribution in the Galaxy (the most massive stellar objects are progenitors of the relativistic compact objects) is such that the number of stars very strongly (as M^{-5}) increases with decreasing stellar mass.

In addition, a mass distribution dip between $2M_\odot$ and $4M_\odot$ seems to exist for neutron star and BH masses. In this mass range, no neutron stars or BHs have been observed. The mass dip within the range $(2 - 4)M_\odot$ for neutron stars and BH mass distributions, if confirmed in further observations (especially from observations of X-ray binaries in other galaxies), will require a serious theoretical elucidation.

Let us briefly discuss the problem of SMBH demography (see the recent review by Kormendy and Ho [22]). As noted above, the formation time of SMBHs in galactic nuclei is relatively short, namely less than 10^9 years. Such a rapid formation of very massive BH is difficult to explain in the model assuming their mass growth due to gas accretion onto a low-mass seed BH that has been formed via the core collapse of a massive ($M = 100 \div 1000M_\odot$) population III star, even if the mass accretion rate is as high as the Eddington luminosity.

Recently, in addition to SMBHs, the important role of massive stellar clusters located in galaxy center has been revealed [43, 44].

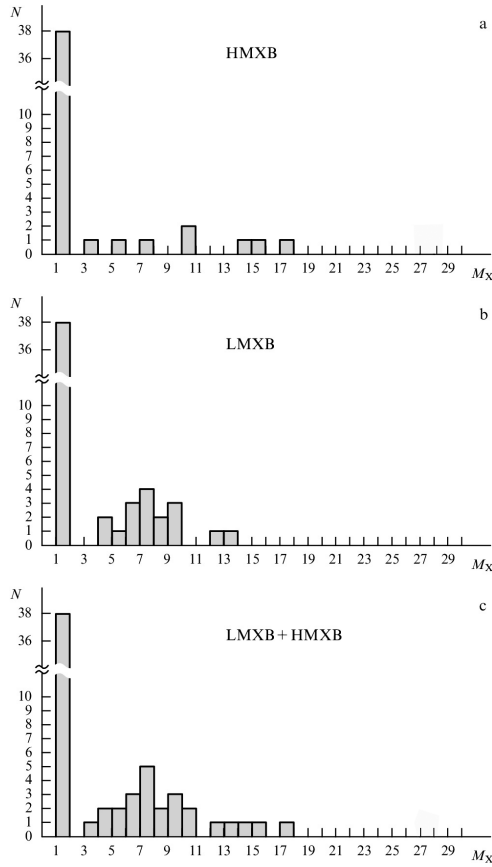


Figure 2: Neutron star and black hole mass distributions in binary systems: (a) black hole masses in high-mass X-ray binaries (HMXB) with massive optical stars of O–B and WR spectral classes; (b) black hole masses in low-mass X-ray binaries (LMXB), and (c) the total black hole and neutron star mass distributions (in low-mass and high-mass X-ray binaries). The high peaks in the left part of the panels (a)–(c) correspond to neutron star masses.

An important correlation is also revealed between SMBH masses, the masses of central star clusters, and parameters of spheroidal galactic components:

$$M \sim \sigma^\beta,$$

where M is the mass of the SMBH or a stellar cluster, and σ is the star velocity dispersion in the spheroidal component. The index of a power is $\beta = 4 \div 5$ for SMBHs (e.g., [45]), and β falls within the range from 1.57 ± 0.24 [45] to 2.73 ± 0.29 .

Although the dispersion of the exponent β for central star clusters is large ($\beta = 1.57 \div 2.73$), the dependence of mass M on the velocity dispersion σ for central star cluster may be considered as weaker compared to SBMHs. This allows us to assume that the formation and evolution of central SMBHs and massive star clusters in galactic nuclei are related to different mechanisms.

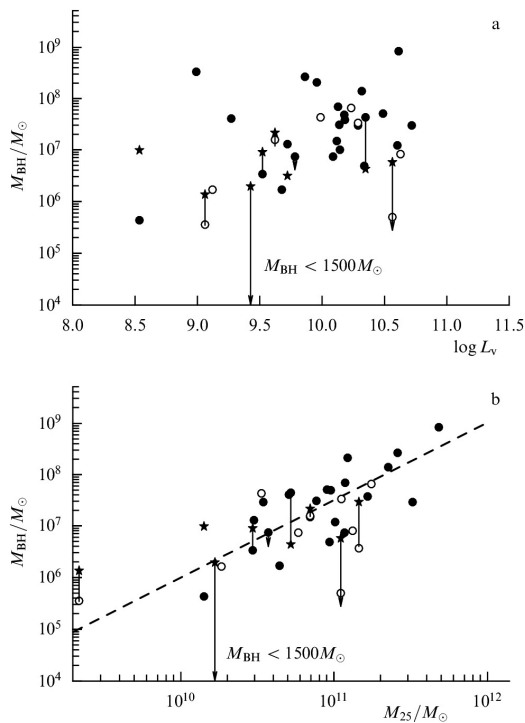


Figure 3: SMBH mass as function: (a) total optical luminosity L_V of the host galaxy characterizing the baryonic mass, and (b) the indicative mass of the galaxy $M_{25} = V_{far}^2 R_{25}/G$, which includes both baryonic and dark-matter masses. The filled “star” symbols correspond to central stellar clusters. Linear segments join circles (BHs) and filled “stars” (clusters). Arrows show the upper limits (taken from paper by Zasov et al. [43]).

Of special interest is the possible association of central SMBHs and massive star clusters with dark matter in galaxies. Our observations of the galactic rotation in galaxies with known heavy central black hole masses are aimed at solving this problem [43, 46, 27]. As shown in studies performed by A.V. Gurevich’s group [47], the gravitational instability in proto-galaxy dark matter clumps form sharp and deep minima of gravitational potential (cusps), into which baryonic matter “falls” to produce a stellar population of the forming galaxy.

This process can also stimulate the formation of an SMBH in galaxy nucleus. Therefore, the association of the central SMBH mass with the mass of the galactic halo dominated by dark matter is rather expectable. Indeed, due to coalescence of galaxies at early stages of their formation, as well as star formation in galactic centers, this association can be rather indirect. Nevertheless, the search for a correlation between the central SMBH mass and the dark matter-dominated galactic halo mass is a very important observational task.

In Fig. 3 important correlations obtained in our paper [43] are presented. They demonstrate the important role of dark matter in the central SMBH formation in the galactic nucleus. The figure depicts two dependencies: $M_{BH}(L_V)$ and

$M_{BH}(M_{25})$, where L_V is the total optical luminosity of the galaxy, which is a single-valued function of the total baryonic mass of the galaxy, and M_{25} is the so-called indicative mass of the galaxy: $M_{25} = V_{far}^2 R_{25} / G$, where V_{far} is the observed maximum rotational velocity of the galaxy (which tends to a plateau at large distances from the nucleus), and R_{25} is the radius of the galactic region limited by the surface brightness isophot reaching the 25th stellar magnitude per square arcsecond, which determines the boundary of the visible part of the galaxy. Apparently, there is virtually no correlation between the SMBH mass and the total baryonic mass of the whole galaxy. At the same time, if we consider the indicative galactic mass M_{25} for the same galaxies as comprising both baryonic and substantial fraction of dark matter, a good $M_{BH}(M_{25})$ correlation is revealed. This result immediately indicates that the influence of dark matter on central SMBH formation, although indirect, remains quite significant.

The linkage of central SMBH and stellar clusters with the kinematics and color of host galaxies was studied in more detail in the paper by Zasov and Cherepashchuk [27].

5 Conclusions

After 45 years of observational studies of BHs, there are almost no doubts that these extreme objects really exist in the Universe. This is due to the fact that all observations of these massive and very compact objects are in beautiful agreement with GR prediction for black holes.

Recent discovery of gravitational waves from a binary black hole merger GW150914 [3] opens a new era in investigations of black holes.

References

1. *Ya.B. Zeldovich*, *Sov. Phys. Dokl.*, **9**, 195, 1964.
2. *E.E. Salpeter*, *Astrophys. J.*, **140**, 796, 1964.
3. *B.P. Abbott, R. Abbott, T.D. Abbott et al.*, *Phys. Rev. Lett.*, **116**, 061102, 2016.
4. *N.I. Shakura, R.A. Sunyaev*, *Astron. Astrophys.*, **24**, 337, 1973.
5. *J.E. Pringle, M.J. Rees*, *Astron. Astrophys.*, **21**, 1, 1972.
6. *I.D. Novikov, K.S. Thorne*, in *Black Holes*. Eds. C. De Witt, B.S. De Witt. New York: Gordon and Breach, 1973, p. 343.
7. *V.V. Sobolev*, *A Treatise on Radiative Transfer*. Princeton: Van Nostrand and Co. Inc., 1963.
8. *A.M. Cherepashchuk, Yu.N. Efremov, N.E. Kurochkin et al.*, *Inf. Bull. Var. Stars*, No. 720, 1, 1972.
9. *J.N. Bahcall, N.A. Bahcall*, *Astrophys. J. Lett.*, **178**, L1, 1972.
10. *V.M. Lyutiy, R.A. Sunyaev, A.M. Cherepashchuk*, *Sov. Astron.*, **17**, 1, 1973.

11. V.M. Lyutyi, R.A. Sunyaev, A.M. Cherepashchuk, *Sov. Astron.*, **18**, 684, 1974.
12. E.A. Antokhina, A.M. Cherepashchuk, V.V. Shimansky, *Astron. Zh.*, **82**, 131, 2005.
13. G.S. Bisnovatyi-Kogan, B.V. Komberg, *Sov. Astron.*, **18**, 217, 1974.
14. B. Kiziltan, A. Kottlas, S.E. Thorsett, *Astrophys. J.*, **778**, 2013.
15. M.A. Alpar, A.F. Cheng, M.A. Ruderman, J. Shaham, *Nature*, **300**, 728, 1982.
16. J.E. McClintock, R.A. Remillard, in *Compact Stellar X-ray Sources*. Eds. W. Lewin, M. Van der Klis. Cambridge Astrophys. Ser., vol. 39. Cambridge: Cambridge Univ. Press, 2006, p. 157.
17. R. Narayan, J.E. McClintock, *Mon. Not. Roy. Astron. Soc.*, **419**, L69, 2012.
18. R.D. Blandford, R.I. Znajek, *Mon. Not. Roy. Astron. Soc.*, **179**, 433, 1977.
19. A.M. Cherepashchuk, *Mon. Not. Roy. Astron. Soc.*, **194**, 761, 1981.
20. B. Margon, *Ann. Rev. Astron. Astrophys.*, **22**, 507, 1984.
21. Ya.B. Zeldovich, I.D. Novikov, *Sov. Phys. Dokl.*, **9**, 834, 1964.
22. J. Kormendy, L.C. Ho, *Ann. Rev. Astron. Astrophys.*, **51**, 511, 2013.
23. S. Gillessen, F. Eisenhauer, S. Trippe *et al.*, *Astrophys. J.*, **692**, 1075, 2009.
24. J.M. Moran, L.J. Greenhill, J.R. Herrnstein, *J. Astrophys. Astron.*, **20**, 165, 1999.
25. A.M. Cherepashchuk, W.M. Lyutyi, *Astrophys. Lett.*, **13**, 165, 1973.
26. E.A. Dibai, *Sov. Astron.*, **28**, 123, 1984.
27. A.V. Zasov, A.M. Cherepashchuk, *Astron. Rep.*, **57**, 797, 2013.
28. Y. Shen, J.E. Greene, M.A. Strauss *et al.*, *Astrophys. J.*, **680**, 169, 2008.
29. M. Volonteri, M.J. Rees, *Astrophys. J.*, **650**, 669, 2006.
30. L.W. Brenneman, C.S. Reynolds, M.A. Nowak *et al.*, *Astrophys. J.*, **736**, 103, 2011.
31. K.S. Thorne, *Astrophys. J.*, **191**, 507, 1974.
32. R.A. Daly, *Mon. Not. Roy. Astron. Soc.*, **414**, 1253, 2011.
33. Yu.N. Gnedin, *Phys. Usp.*, **56**, 709, 2013.
34. J. Wilms, C.S. Reynolds, M.C. Begelman *et al.*, *Mon. Not. Roy. Astron. Soc.*, **328**, L27, 2001.
35. S.S. Doelman, J. Weintroub, A.E.E. Rogers *et al.*, *Nature*, **455**, 78, 2008.
36. S.S. Doelman, V.L. Fish, D.E. Schenck *et al.*, *Science*, **338**, 355, 2012.
37. M.D. Johnson, V.L. Fish, S.S. Doelman *et al.*, *Science*, **350**, 1242, 2015.
38. I.M. McHardy, E. Koerding, C. Knigge *et al.*, *Nature*, **444**, 730, 2006.
39. A. Merloni, S. Heinz, T. Di Matteo, *Mon. Not. Roy. Astron. Soc.*, **345**, 1057, 2003.
40. M. Gierliński, M. Middleton, M. Ward, C. Done *et al.*, *Nature*, **455**, 369, 2008.
41. A.M. Cherepashchuk, *Astron. Rep.*, **45**, 120, 2001.

42. *A.M. Cherepashchuk*, *Phys. Usp.*, **45**, 896, 2002.
43. *A.V. Zasov*, *A.M. Cherepashchuk*, *I.Yu. Katkov*, *Astron. Rep.*, **55**, 595, 2011.
44. *L. Ferrarese*, *P. Côté*, *J.-C. Cuillandre et al.*, *Astrophys. J. Lett.*, **644**, L21, 2006.
45. *A.W. Graham*, *Mon. Not. Roy. Astron. Soc.*, **422**, 1586, 2012.
46. *A.M. Cherepashchuk*, *V.L. Afanas'ev*, *A.V. Zasov*, *I.Yu. Katkov*, *Astron. Rep.*, **54**, 578, 2010.
47. *A.S. Ilyin*, *K.P. Zybin*, *A.V. Gurevich*, *J. Exp. Theor. Phys.*, **98**, 1, 2004.

Continuum Variations with Luminosity in Accreting X-Ray Pulsars

M.I. Gornostaev^{1,2}, K.A. Postnov^{1,2}, D. Klochkov³,
N.I. Shakura²

E-mail: *mgornost@gmail.com*

Two-dimensional structure of accretion columns in the radiation-diffusion limit is calculated for two possible geometries (filled and hollow cylinder) for mass accretion rates \dot{M} ranging from 10^{17} to 1.2×10^{18} g s⁻¹. The observed spectral hardening in the transient X-ray pulsars with increasing \dot{M} can be reproduced by a Compton-saturated sidewall emission from optically thick magnetized accretion columns with taking into account the emission reflected from the neutron star atmosphere. At \dot{M} above some critical value $\dot{M}_{cr} \sim (6-8) \times 10^{17}$ g s⁻¹, the height of the column becomes such that the contribution of the reflected component to the total emission starts decreasing, which leads to the saturation and even slight decrease of the spectral hardness. Hollow-cylinder columns have a smaller height than the filled-cylinder ones, and the contribution of the reflected component in the total emission does not virtually change with \dot{M} (and hence the hardness of the continuum monotonically increases) up to higher mass accretion rates than \dot{M}_{cr} for the filled columns.

1 Observations

After the discovery of X-ray pulsars in 1971 [1] it was realized that in bright pulsars the radiation plays a crucial role in braking of the accreting matter onto the surface of a neutron star with strong magnetic field. It is now well recognized that once the radiation density above the polar cap starts playing the role in the accreting matter dynamics, an optically thick accretion column above the polar cap is formed [2] (see [3] for the latest investigation). The characteristic height of the column increases with accretion rate, most of the emission escapes through sidewalls, and it can be expected that above some X-ray luminosity the dependence of the observed properties of the continuum emission on the X-ray luminosity can become different from that in the low-luminosity regime.

Indeed, a similar bimodality is observed in the dependence of the X-ray continuum hardness on luminosity. This dependence can be studied using, for example, data from all-sky monitors such as RXTE/ASM and MAXI,

¹ Faculty of Physics, M.V. Lomonosov Moscow State University, Russia

² Sternberg Astronomical Institute, Moscow M.V. Lomonosov State University, Russia

³ Institute of Astronomy and Astrophysics, Karl-Eberhard University, Germany

i.e. without dedicated spectroscopic observations which are necessary to measure CRSFs. Following this approach, we measured the hardness ratio as a function of luminosity in the accreting pulsars GX 304-1, 4U 0115+63, V 0332+53, EXO 2030+375, A 0535+26 and MXB 0656-072 using the data from different energy bands of RXTE/ASM. The result is shown in Fig.1. To convert the ASM count rates into X-ray luminosities, we used published distances to the sources (GX 304-1: ~ 2 kpc [4]; 4U 0115+63: ~ 7 kpc [5], V 0332+53: ~ 7 kpc [6]; EXO 2030+375: ~ 7 kpc [7]; A 0535+26: ~ 2 kpc [8]; MXB 0656-072: ~ 3.9 kpc [9]) and their broadband X-ray spectra from the archival pointed observations with INTEGRAL and RXTE available to us. One can see that at lower fluxes the hardness ratio increases with flux. At a certain flux, however, a flattening of the hardness ratio is observed in 4U 0115+63, V 0332+53, EXO 2030+375, A 0535+26 and MXB 0656-072. This “turnover” occurs at the flux roughly corresponding to luminosities $(3-7) \times 10^{37}$ erg s $^{-1}$. In GX 304-1, which does not show such a turnover, this “critical” luminosity has simply not been reached during the outbursts registered by RXTE/ASM.

A similar dependence of spectral properties on the X-ray flux at luminosities below $\sim 10^{37}$ erg s $^{-1}$ was also reported from spectroscopic observations of the transient Be-X-ray pulsar GRO J1008-57 [10].

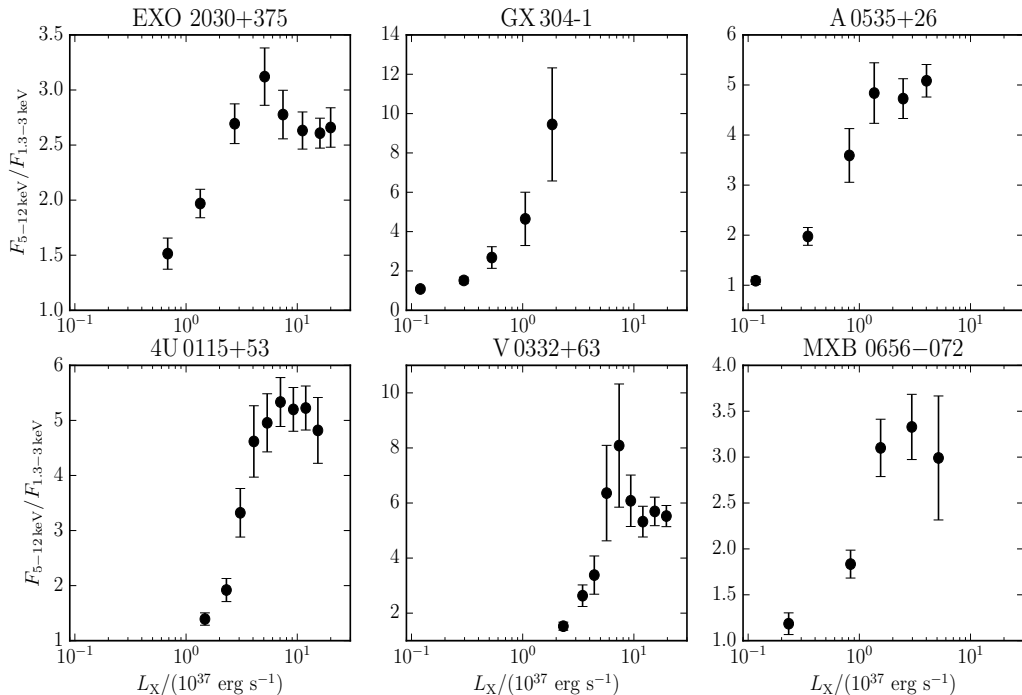


Figure 1: The ratio of the fluxes in 5–12 keV and 1.33–3 keV ranges (referred to as “hardness ratio” in text) measured with RXTE/ASM for six transient accreting pulsars as a function of the total ASM flux in the 1.33–12 keV range.

2 Numerical simulations of accretion column in radiation-diffusion approximation

2.1 Boundary conditions

We introduce cylindrical coordinates r , φ , z centered at the columns axis and $z = 0$ at the neutron star surface. The initial velocity of the falling matter at high altitude above the surface of the neutron star is $v_0 = 10^{10}$ cm s⁻¹. At the cylinder base ($z = 0$), the velocity is $v = 0$. As a boundary condition at the column side surface we used the relation between the radial energy flux and the energy density U in the form $F_r(r_0, z) = 2cU(r_0, z)/3$, which roughly corresponds to the conditions expected in the scattering atmospheres in the Eddington approximation.

2.2 Basic equations

The cylindrical symmetry of the problem makes it essentially two-dimensional. The steady-state momentum equation (ignoring gravity, which is very good approximation as discussed, e.g., in [2]) for accretion braking by the radiation with energy density U reads $(\mathbf{S} \cdot \nabla) \mathbf{v} = -\frac{1}{3}\nabla U$. The mass continuity equation is $\mathbf{S} = \rho \mathbf{v} = \text{const}$. The integration of momentum equation yields

$$U = 3S(v_0 - v). \quad (1)$$

Following [11], the energy equation can be written as

$$\nabla \cdot \mathbf{F} = -\mathbf{S} \cdot \nabla \left(\frac{v^2}{2} \right), \quad (2)$$

where we have neglected the flow of internal energy of the falling matter.

The radiative transfer equation for the components of the radiation energy flux in cylindrical coordinates yields

$$F_r = \frac{-\frac{c}{3\kappa_{\perp}\rho} \frac{\partial U}{\partial r}}{1 + \frac{1}{3\kappa_{\perp}\rho} \frac{1}{U} \left| \frac{\partial U}{\partial r} \right|}, \quad F_z = \frac{-\frac{c}{3\kappa_{\parallel}\rho} \frac{\partial U}{\partial z} - \frac{4}{3}Uv}{1 + \frac{1}{3\kappa_{\parallel}\rho} \frac{1}{U} \left| \frac{\partial U}{\partial z} \right|}, \quad (3)$$

where the denominators are introduced to use the modified diffusion approximation [12].

The system of equations (1)–(3) was solved numerically for accretion rates onto one pole in the range 10^{17} – 1.2×10^{18} g s⁻¹ for the geometry of filled cylinder with radius r_0 and the hollow cylinder with wall thickness $0.1r_0$ (see [13] for details). The column structure at different accretion rates is shown in Fig. 2.

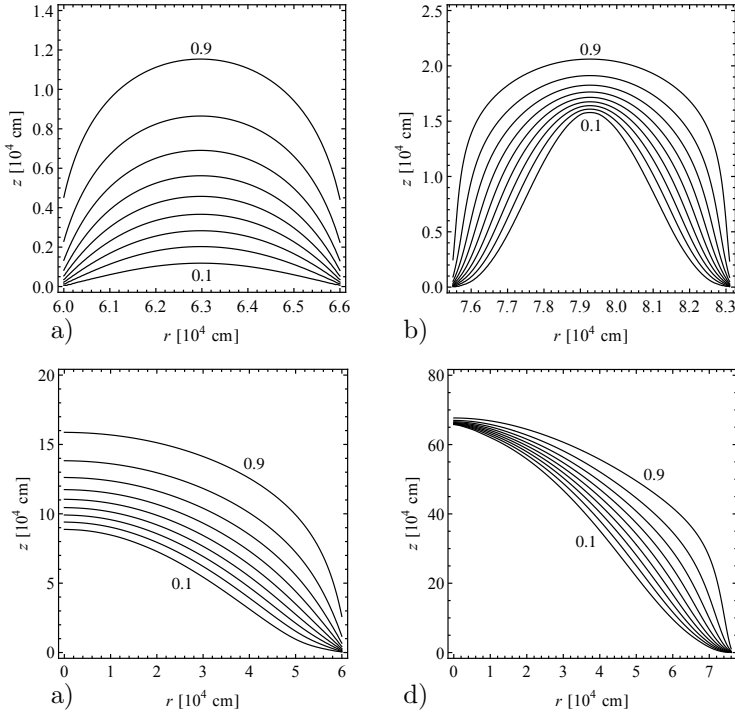


Figure 2: Contours of constant Q (0.9 to 0.1, from top to bottom). The hollow cylinder geometry calculated for $M_{17} = 1$ (a) and $M_{17} = 5$ (b). The filled cylinder geometry for $M_{17} = 1$ (c) and $M_{17} = 5$ (d).

3 Hardness ratio variations

3.1 Saturated Compton spectrum of sidewall emission

The LTE treatment of the spectrum of the sidewall emission from accretion columns is clearly a strong oversimplification. To take into account the scattering on electrons in the optically thin boundary of the column, we can use the model calculations of the radiation transfer problem in a semi-infinite plane-parallel atmosphere with strong magnetic field. In this case the emerging spectrum will be formed in the saturated Compton regime, with the mode 1 photons (extraordinary, i.e. polarized perpendicular to the $\mathbf{k} - \mathbf{B}$ -plane, where \mathbf{k} is the photon wavevector and \mathbf{B} is the magnetic field vector) predominantly escaping through sidewalls [14]. The intensity of mode 2 (ordinary, i.e. polarized in the $\mathbf{k} - \mathbf{B}$ plane) photons is comparable to that of mode 1 photons only at large angles to the normal, $\mu' \sim 0$, and thus insignificantly contributes to the total flux from the unit surface area due to the geometrical factor.

In this regime, the specific intensity of extraordinary photons at energies far below the cyclotron resonance can be written as $I'_\nu = (1 + 2\mu') \frac{2\sqrt{3}}{5} \frac{h\nu\nu_g^2}{c^2\tau_0} e^{-\frac{h\nu}{kT}}$ [14], where $\mu' = \cos\theta'$ is the angle between the normal to the atmosphere and the

escaping radiation direction in the plasma reference frame, τ_0 is the characteristic optical depth of the problem, $\nu_g = \frac{eB}{2\pi m_e c}$ is the electron gyrofrequency in the magnetic field. By expressing the characteristic optical depth τ_0 through the emergent radiation flux Φ using (34)–(37) from [14], we find

$$I_\nu = \frac{I'_\nu}{1 + 2\mu'} = \frac{3}{10\pi} \left(\frac{h\nu}{kT} \right)^2 \frac{\Phi}{\nu} e^{-\frac{h\nu}{kT}}. \quad (4)$$

Therefore, we are in the position to calculate the emerging spectrum from the column in this approximation using the solutions for the column structure obtained above. To do this, it is sufficient to substitute the total radial energy flux at each height of the column $\Phi \rightarrow F_r(z)/2$ ($F_r(z)$ in Eq. (3) is known from our numerical calculations), and temperature $T \rightarrow T(z)$ estimated deep inside the column (at the optical depth ~ 1), so that $T(z) = (U(z)/a_r)^{1/4}$.

3.2 Account for the reflected component

Now we should take into account the fact that the electrons in the optically thin part of the column are moving with high velocity $v_0 \sim 1/3c$, and thus the emission beam of the column (4) should be Doppler-boosted towards the neutron star surface and reflected from the neutron star atmosphere, as discussed in [15] and [16]. The reflection coefficient in the case of single Compton electron scattering in strong magnetic field is determined by the ratio $\lambda(\nu) = \kappa_{sc}/(\kappa_{sc} + \kappa_{abs})$, where κ_{sc} and κ_{abs} are the scattering and absorption coefficients for photons in the strong magnetic field, respectively. Since the calculated X-ray albedo turns out to be very similar for both extraordinary and ordinary photons and is virtually insensitive to the photon incident angle to the magnetic field, below we shall use its mode-averaged value for the angle $\pi/4$.

Let α be the angle between the photon wavevector and the plasma bulk velocity vector. The critical value α^* within which the radiation from the height z will be intercepted by the neutron star (in the Schwarzschild metric and with taking into account the difference between the polar axis and the column cylinder side) is

$$\alpha^*(z) = \arcsin \left(\frac{R_{NS}}{\sqrt{(R_{NS}+z)^2 + r_0^2}} \sqrt{\frac{1 - r_S/\sqrt{(R_{NS}+z)^2 + r_0^2}}{1 - r_S/R_{NS}}} \right) - \arctan \frac{r_0}{R_{NS}+z},$$

where $r_S = 2GM/c^2$ is the Schwarzschild radius (cf. [16]).

Let Σ be the surface of the column, $\Sigma'(\varphi, z)$ be a point on the surface and $d\Sigma = r_0 d\varphi dz$ be the elementary area. The flux from the surface element at frequency ν (in conventional notations) reads $f_\nu(\Sigma') = dE(\Sigma')/(dt d\nu d\Sigma)$ and can be separated into three parts in accordance to the angle relative to the observer. Photons escaping with angles $\alpha > \alpha^*$ to the column are directly seen as the proper column radiation f_ν^{col} . The second part includes the radiation f_ν^{ref} intercepted by the neutron star and reflected from the neutron star surface with

X-ray albedo $\lambda(\nu)$. The third part f_ν^{abs} is the radiation absorbed and re-radiated by the neutron star atmosphere. Then we can write

$$\begin{aligned}
 f_\nu(\Sigma') &= \int_{-1}^1 \frac{df_\nu(\Sigma')}{d \cos \alpha} d \cos \alpha \\
 &= \int_{-1}^{\cos \alpha^*} \frac{df_\nu(\Sigma')}{d \cos \alpha} d \cos \alpha + \lambda(\nu) \int_{\cos \alpha^*}^1 \frac{df_\nu(\Sigma')}{d \cos \alpha} d \cos \alpha + (1-\lambda(\nu)) \int_{\cos \alpha^*}^1 \frac{df_\nu(\Sigma')}{d \cos \alpha} d \cos \alpha \\
 &= f_\nu^{col}(\Sigma') + f_\nu^{ref}(\Sigma') + f_\nu^{abs}(\Sigma').
 \end{aligned} \tag{5}$$

The integrands [16] in the cylindrical coordinates with account for the axial symmetry ($I_\nu(\Sigma') = I_\nu(z)$, giving by (4)) have the form

$$\frac{df_\nu(\Sigma')}{d \cos \alpha} = I_\nu(z) \frac{2D^3}{\gamma} \sin \alpha \left(1 + \frac{\pi D}{2} \sin \alpha \right),$$

where the Doppler factor is $D = 1/(\gamma(1 - \beta \cos \alpha))$, $\gamma = 1/\sqrt{1 - \beta^2}$ is the plasma Lorentz factor and $\beta = v/c$. Then for the total radiation from the column at frequency ν we obtain

$$\begin{aligned}
 L_\nu &= \iint_{\Sigma} f_\nu(\Sigma') d\Sigma = 2\pi r_0 \int_0^{z_{max}} \left(f_\nu^{col}(z) + f_\nu^{ref}(z) + f_\nu^{abs}(z) \right) dz \\
 &= L_\nu^{col} + L_\nu^{ref} + L_\nu^{abs},
 \end{aligned} \tag{6}$$

where z_{max} is the upper limit of the computational area. The observed X-ray flux from one column is $F_\nu = (L_\nu^{col} + L_\nu^{ref})/(4\pi d^2)$, where d is the distance to the source. For the illustrative purposes, we assume $d = 5$ kpc. Taking into account the radiation absorbed by the neutron star atmosphere L_ν^{abs} will add more soft photons to the total spectrum.

Since we are observing both the direct and reflected radiation from the column, the total change in the hardness of the spectrum depends on the fraction of the reflected radiation in the total flux. This, in turn, depends on the height of the column. We have calculated the total flux as the sum of the direct and reflected component as a function of \dot{M} with taking into account the photon ray propagation in the Schwarzschild metric of the neutron star with a fiducial mass $M = 1.5M_\odot$ and radius $R = 10$ and 13 km. The magnetic field of the neutron star is set to 3×10^{12} G, so that the CRSF energy is about 35 keV. The result is presented in Fig. 3. It is seen that the hardness ratio

$$\text{HR} = \frac{\int_{5 \text{ keV}}^{12 \text{ keV}} F_\nu d\nu}{\int_{1.3 \text{ keV}}^{3 \text{ keV}} F_\nu d\nu}$$

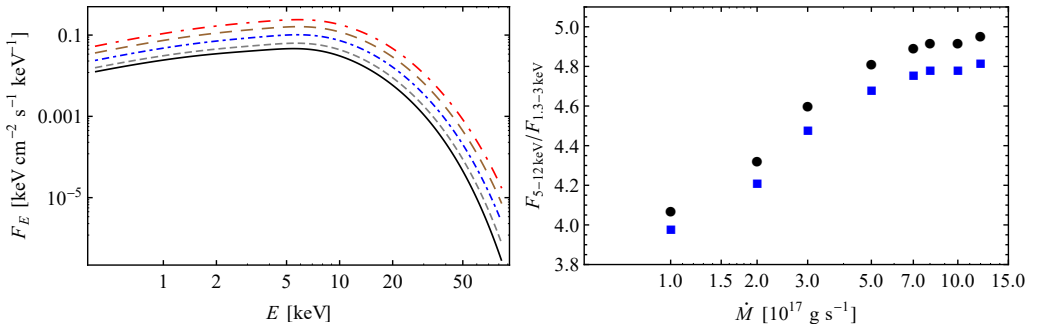


Figure 3: *Left*: the total spectrum of direct sidewall and reflected from the neutron star atmosphere from the optically thick filled accretion column for mass accretion rates $\dot{M}_{17} = 2, 3, 5, 8$ and 12 (from bottom to up, respectively). *Right*: the hardness ratio HR of the total spectrum. Shown are calculations for the neutron star radius $R_{NS} = 10$ km (squares) and $R_{NS} = 13$ km (circles).

first increases with the mass accretion rate (X-ray luminosity), but starting from $\dot{M}_{cr} \sim (6-8) \times 10^{17} \text{ g s}^{-1}$, it gets saturated. This is in agreement with observations shown in Fig. 1.

For the hollow cylinder accretion columns which have smaller height (see Fig. 2), the fraction of the reflected component in the total emission does not virtually change with mass accretion rate within the calculated range, therefore the hardness ratio of the total spectrum monotonically increases with \dot{M} in this range. Note also that in this case the spectrum is harder than in the case of the filled column because the reflected (harder) emission dominates in the total spectrum.

4 Summary and conclusions

Therefore, our model calculations lead to the following conclusions:

1. The spectral hardening in X-ray pulsars with positive CRSF energy dependence on X-ray flux can be explained by increasing of the Comptonization parameter y in the slab atmosphere of the accretion mound. It is in this regime that positive correlation of the cyclotron line is observed, for example, in Her X-1 [17].
2. At high accretion rates, the radiation-supported optically thick accretion column grows above the polar cap, the sidewall emission from the column is formed by extraordinary photons in the saturated Compton regime. The spectrum of this emission gets harder with increasing mass accretion rate.
3. With further increasing mass accretion rate the height of the column increases, such that the fraction of radiation reflected from the neutron star atmosphere starts decreasing. As the reflected radiation is harder than the incident one,

the spectrum of the total emission (direct plus reflected) stops hardening (and even becomes slightly softer).

4. In the frame of this model, the saturation of the spectral hardness in the case of a hollow cylinder geometry of the accretion column can be achieved at much higher accretion rates (roughly, scaled with the relative thickness of the column wall, b), because the characteristic height of the column in this case is correspondingly smaller than that of the filled column.

References

1. R. Giacconi, H. Gursky, E. Kellogg et al., *Astrophys. J. Lett.*, **167**, L67, 1971.
2. M.M. Basko, R.A. Sunyaev, *Mon. Not. Roy. Astron. Soc.*, **175**, 395, 1976.
3. A.A. Mushtukov, V.F. Suleimanov, S.S. Tsygankov, J. Poutanen, *Mon. Not. Roy. Astron. Soc.*, **447**, 1847, 2015.
4. G.E. Parkes, P.G. Murdin, K.O. Mason, *Mon. Not. Roy. Astron. Soc.*, **190**, 537, 1980.
5. I. Negueruela, A.T. Okazaki, *Astron. Astrophys.*, **369**, 108, 2001.
6. I. Negueruela, P. Roche, J. Fabregat, M.J. Coe, *Mon. Not. Roy. Astron. Soc.*, **307**, 695, 1999.
7. C.A. Wilson, M.H. Finger, M.J. Coe et al., *Astrophys. J.*, **570**, 287, 2002.
8. I.A. Steele, I. Negueruela, M.J. Coe, P. Roche, *Mon. Not. Roy. Astron. Soc.*, **297**, L5, 1998.
9. V.A. McBride, J. Wilms, M.J. Coe et al., *Astron. Astrophys.*, **451**, 267, 2006.
10. M. Kühnel, S. Müller, I. Kreykenbohm et al., *Phys. J. Web Conf.*, **64**, 6003, 2014.
11. K. Davidson, *Science*, **246**, 1, 1973.
12. Y.-M. Wang, J. Frank, *Astron. Astrophys.*, **93**, 255, 1981.
13. K.A. Postnov, M.I. Gornostaev, D. Klochkov et al., *Mon. Not. Roy. Astron. Soc.*, **452**, 1601, 2015.
14. Y.E. Lyubarskii, *Astrophys.*, **25**, 577, 1986.
15. Y.E. Lyubarskii, R.A. Sunyaev, *Astron. Lett.*, **14**, 390, 1988.
16. J. Poutanen, A.A. Mushtukov, V.F. Suleimanov et al., *Astrophys. J.*, **777**, 115, 2013.
17. R. Staubert, N.I. Shakura, K. Postnov et al., *Astron. Astrophys.*, **465**, L25, 2007.

A 2D Model of Non-Stationary Accretion onto a Magnetized Neutron Star

V.V. Grigoryev¹, A.M. Krassilchtchikov²

E-mail: *vitaliygrigoryev@yandex.ru*, *kra@astro.ioffe.ru*

A 2D non-stationary model of column accretion over the surface of a magnetized neutron star is presented. It is found that collisionless shocks appear and evolve in the column on the time scales of about 10^{-7} s, and their surface is not flat. A significant non-uniformity of flow parameters across the column is observed. In general, the modeling results agree with those of the previously developed 1D model.

1 Introduction

Accretion onto compact stellar objects was recognized as an efficient source of hard X-ray emission already 50 years ago [1, 2]. Ya.B. Zeldovich [3, 4] showed that the spectrum emitted from the vicinity of a neutron star surface critically depends on the accretion regime, namely, on whether the infalling matter comes as separate particles (free-fall) or as a hydrodynamic flow.

The accretion models developed in 1970–80 postulated the existence of a collisionless shock in the column, and its height over the surface of the star was a model parameter. However, for the substantially super-Eddington case J. Arons and R. Klein [5] and their collaborators [6] showed that non-stationary radiation-dominated shocks appear and evolve in the accretion column.

Apart from gas dynamics in an accretion column, some studies were devoted to the problem of radiation transfer in the column. Thus, R. Araya, A. Harding considered the influence of Compton processes on the transfer of cyclotron line emission and computed line profiles for a set of column parameters [7].

In 2004 A.M. Bykov and A.M. Krassilchtchikov [8] developed a 1D model of non-stationary accretion in a column of a magnetized neutron star. They did not postulate the existence of a shock in the column, rather, such a shock appeared as a natural result of evolution of an accreting flow. In this model a collisionless shock formed on the scales of 10^{-5} s. Thus, the aim of the present work was to extend the model of [8] to the 2D case and compare the resulting flow profiles.

¹ St. Petersburg State University, Russia

² Ioffe Institute, St. Petersburg, Russia

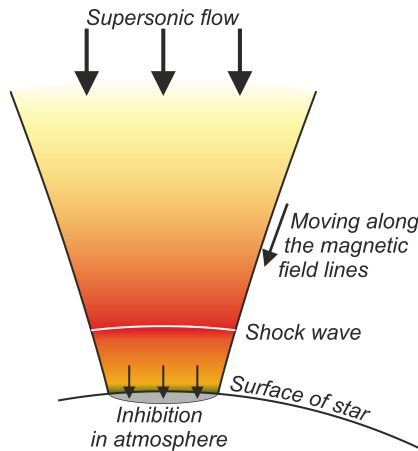


Figure 1: A sketch of the modeled accretion column.

2 The accretion column model

We consider a numerical model of sub-Eddington non-stationary accretion in a 2D column over a magnetic pole of a neutron star. We do not postulate the existence of a shock in the column as an initial condition. The model takes into account various interactions of two sorts of particles (electrons and ions) within the infalling hydrodynamical flow, as well as interaction of the plasma and radiation field. We consistently describe the dynamics of the plasma flow in the strong magnetic field of the star which is considered stationary. A sketch of the modeled system is presented in Fig. 1.

One of the main features of the presented model is a Godunov-type hydrodynamical approach which allowed us to treat discontinuous flows and describe shocks dynamics. Another feature of the model is the use of 2D dipole geometry, which is a natural choice to describe the flow of gas along the force lines of the dipole magnetic field.

The main global parameters of the employed model are as follows: the accretion rate \dot{M} (typically $\dot{M} \sim 10^{15}$ g/s), the induction of the dipole magnetic field of a neutron star B ($\sim 10^{12}$ G), the radius of the star (~ 10 km), the mass of the star (~ 1.4 Solar mass), the area of the accretion spot on the star surface (~ 1 km²).

3 Input physics and the numerical approach

The accreting plasma flow is treated in the 1-flow hydrodynamical approximation, due to the very short time scale of 2-flow instabilities. Hence, we model a flow of two fluids (electrons and ions) moving at the same velocity, but having different temperatures. The magnetic field of the neutron star is kept constant on the considered times scales.

The flow evolution is described by the following set of equations:

$$\begin{cases} \frac{\partial \rho}{\partial t} + \text{div}(\rho \vec{u}) = 0, \\ \frac{\partial(\rho \vec{u})}{\partial t} + \nabla P + \nabla \cdot (\vec{u} \oplus (\rho \vec{u})) = \vec{\mathcal{F}}, \\ \frac{\partial}{\partial t} \left[\rho_s \left(E_s + \frac{u^2}{2} \right) \right] + \text{div} \left[\rho_s \vec{u} \left(E_s + \frac{u^2}{2} \right) + p_s \vec{u} \right] = \mathcal{Q}_s, \end{cases} \quad (1)$$

where $\rho = \rho_e + \rho_i$, $p = p_e + p_i$, \mathcal{F} and \mathcal{Q}_s denote the sources of momentum and energy, respectively, and s is the sort of particles (i for ions, and e for electrons).

The set has to be completed with equations of state for each sort of particles. The ideal gas approximation $E_s(\gamma_s - 1) = p_s/\rho_s$ is valid for the considered ranges of temperatures and densities, but to account for the mild relativism achieved at the highest temperatures of the flow, we treat the adiabatic indexes as temperature-dependent values.

For mildly relativistic particles ($k_B T_s \ll m_s c^2$) the adiabatic index can be approximated as $\gamma_s \approx \gamma_{0s} \left(1 - \frac{k_B T_i}{m_i c^2} \right)$ [9], where $\gamma_{0i} = 5/3$ is the usual non-relativistic value for particle distributions with 3 degrees of freedom, and $\gamma_{0e} = 3$ as the electrons appear quasi-one-dimensional in the considered strong magnetic fields.

As we consider both the (resonant) cyclotron line emission, which provides substantial radiative pressure on the flow, and the (non-resonant) continuum emission, the transfer equation is solved by numerical iterations via a custom 2-step procedure with different emission and absorption coefficients at each step.

The force term $\vec{\mathcal{F}}$ is the sum of several forces: the gravitational force, the non-resonant and resonant radiative forces, and the viscous resistive force in the atmosphere of the neutron star (which is, in fact, an extended boundary condition at the bottom of the correction column). The force of resonant radiation acting on the electrons accounts for the scattering phase function (according to [10]), while the non-resonant force is due to Thomson scattering.

The ions change their energy due to the following processes: small-angle scattering with the electrons, collisional excitation of electrons to Landau levels, collisional relaxation in the atmosphere, and the work of the effective ambipolar force.

The electrons change their energy due to the following processes: small-angle scattering with the ions, Bremsstrahlung cooling in collisions with electrons and ions, excitation to Landau levels in collisions with electrons and ions, Compton processes, and the work of the effective ambipolar force.

The complete set of equations is rewritten in dipole geometry and numerically integrated. As the multi-component accreting flow may contain discontinuities, in particular, shocks, a modified Godunov-type approach [11, 12] has been employed. The radiation transfer equation is integrated within a first order finite-difference scheme.

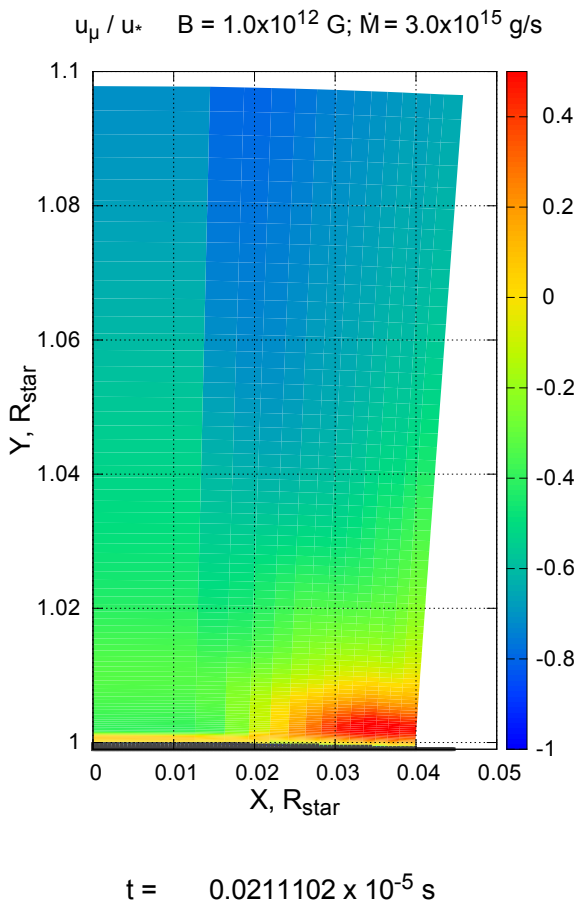


Figure 2: Distribution of velocity projection along the field lines (color) in the cross section of the accretion column.

4 Results

The performed modeling showed collisionless shocks to appear and evolve on the time scales of about 10^{-7} s. The 2D modeling also allows to see that the surface of the evolving shock is not flat, but rather resembles an “upside down hat”: at the borders of the column the shock position is higher than over the pole.

A cross section of a modeled column (projection of 2D velocity onto the field lines) is shown in Figs. 2 and 3 to illustrate the form of the shock.

The 2D model allowed us to account for the flow motion and radiation transfer across the force lines. We also implemented an improved approach to the treatment of radiation transfer accounting for the scattering phase function both for non-resonant and resonant emission.

The presented results of 2D modeling are consistent with those of the 1D model [8]. Namely, the column profiles of accreting plasma parameters of the 2D model near the pole force line are in a qualitative agreement with the profiles

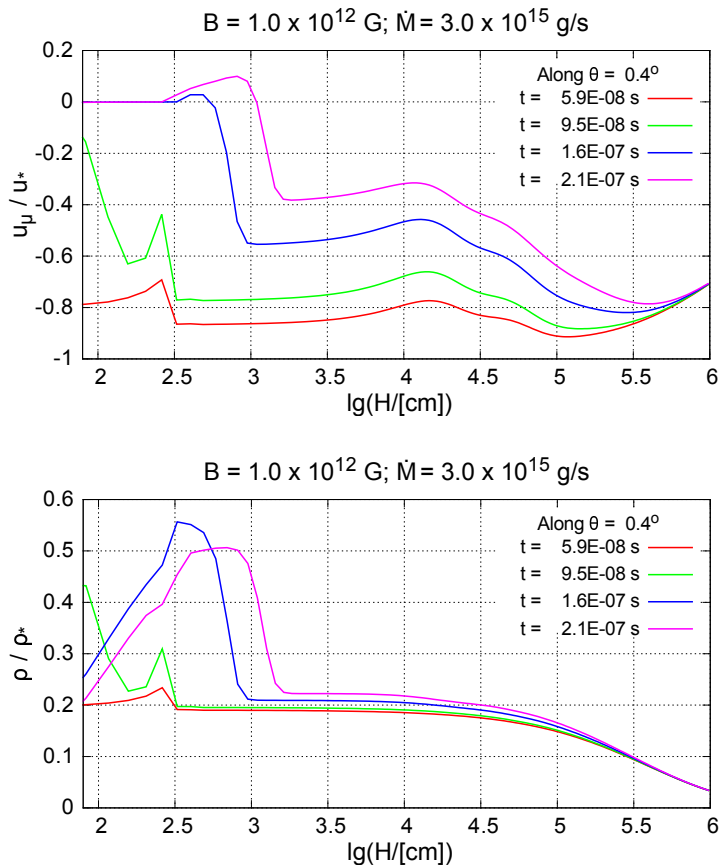


Figure 3: Velocity projection (up) and density (down) along the force line started at the magnetic pole, normalized by $u_* = 1.9 \times 10^{10} \text{ cm/s}$ and $\rho_* = 10^{20} \text{ g/cm}^3$, respectively.

obtained with the 1D model. However, with the new model we also obtain a new effect which could not have been studied before – the inhomogeneity of the flow across the field lines.

References

1. *Ya.B. Zel'dovich*, Dokl. Acad. Nauk SSSR, **155**, 67, 1964.
2. *E.E. Salpeter*, Astrophys. J., **140**, 796, 1964.
3. *Ya.B. Zel'dovich*, Trans. XIII IAU Meet., Prague, 1967.
4. *Ya.B. Zel'dovich, N.I. Shakura*, Astron. Zh., **46**, 255, 1969.
5. *R.I. Klein, J. Arons*, Proc. 23rd ESLAB Symp. on Two-Topics in X-Rays Astronomy. Noordwijk, 1989, p. 89.
6. *R.I. Klein, J. Arons, G. Jernigan, J.J.-L. Hsu*, Astrophys. J. Lett., **457**, L85, 1996.
7. *R.A. Araya, A.K. Harding*, Astrophys. J., **517**, 334, 1999.

8. *A.M. Bykov, A.M. Krasil'shchikov*, *Astron. Lett.*, **30**, 351, 2004.
9. *S. De Groot, W. van Leeuwen, Ch. van Weert*, *Relativistic Kinetic Theory*. Amsterdam: North-Holland, 1980.
10. *A.K. Harding, D. Lai*, *Rep. Prog. Phys.*, **69**, 2631, 2006.
11. *S.K. Godunov, A.V. Zabrodin, M.Ya. Ivanov et al.*, *Numerical Integration of Multi-dimensional Gas-Dynamic Problems*. Moscow: Nauka, 1976 (in Russian).
12. *R.J. LeVeque*, *J. Comput. Phys.*, **131**, 327, 1997.

Generation of Hot Plasma and X-Rays in Comets

S. Ibadov^{1,2}

E-mail: *ibadovsu@yandex.ru*

Generation of hot plasma and X-rays in comets due to high-velocity collisions between cometary and interplanetary dust particles is analytically considered. The results are presented as a brief summary of our researches carried out in the field during the last three decades. It is found that in the inner heliosphere, i.e., at relative velocities of colliding dust particles more than 50–70 km/s (for retrograde and quasi-retrograde comets), initial temperatures of short-living dense plasma clumps produced by these collisions will be more than 10^5 K. Observable indicators of the phenomenon are multicharge ions as well as X-ray radiation of the hot clumps. The study of comets like Halley 1986 III and Hyakutake 1996 B2, having dust to gas production rates ratio more than 0.1, perihelion distances less than 1 AU and almost retrograde orbital motion, providing the dominant role of high-velocity (d-d) collisions in the gas-dust comet comas, is especially important to reveal peculiarities of the new radiation process/mechanisms in the Solar System objects using soft X-ray observatories like ROSAT and XMM. Such researches can expand the role of comets as natural space probes.

1 Introduction

The passage of bright dusty comets through circumsolar region is accompanied by intense collisions between cometary and interplanetary dust particles. Indeed, comet nuclei approaching the Sun become intense sources of gas-dust matter. According to the data of in situ measurements by VEGA 1/2 and GIOTTO missions, carried out at the comet heliocentric distance $R = 0.8\text{--}0.9$ AU, the gas and dust production rates of the nucleus of comet Halley 1986 III are $Q_g = 4 \times 10^7$ and $Q_d = 10^7$ g/s, respectively. These data lead to the dust to gas production rate ratio around 0.25 [1, 2].

Calculations show that for the Halley type dusty comets the dominant interaction mechanism of the gas-dust coma of the comet with interplanetary dust particles, IPD, will be no meteor-like phenomenon (i.e., intense gradual thermal evaporation of IPD due to irradiation by the cometary coma gas molecules), but collisions between comet dust and IPD, (d-d) process, that can lead to high-temperature phenomena: impulse generation of hot plasma, multicharge ions and soft, 0.1–1 keV, X-rays [3, 4, 5].

¹ Moscow State University, Sternberg Astronomical Institute, Russia

² Institute of Astrophysics, Tajik Academy of Sciences, Dushanbe, Tajikistan

Meantime, discovery of soft cometary X-rays was made on 27 March 1996 by orbital telescope ROSAT during observations of bright and dusty comet Hyakutake 1996 B2 having quasi-retrograde orbit [6]. To carry out these observations results of a theoretical consideration [7] was used, as a motivation (Dennerl, Lisse, Truemper, 1998, 1999, private communications).

We present here a brief review of basic results of theoretical investigations on the generation of hot plasma and X-rays in comets due to high-velocity collisions between dust particles as well as some prospects for further X-ray observations of dusty comets.

2 Generation of hot plasma and X-rays in comets by (d-d) process

Collisions between dusty coma of comets and interplanetary/zodiacal dust cloud, (d-d) process, in the inner heliosphere have high-velocity character for comets with retrograde and quasi-retrograde orbits. This phenomenon will lead to production of hot quickly expanding/short-living dense plasma clumps. The initial temperature of the plasma and the mean charge of ions can be analytically presented as $T = T_*(V/V_*)^2$ and $z = z_*(V/V_*)^{(2/s_i)}$ ($s_i = 1.3$ is the parameter of the curve of ionization potentials, $I(z)$, of dust particle atoms), so that at $R_* = 1$ AU we have $V = V_* = 7 \times 10^6$ cm/s and $T_* = 3 \times 10^5$ K, $z_* = 4$ for the Halley 1986 III type comets.

Calculations show that radiation mechanism of hot dense/quickly expanding plasma clumps with the initial radii around and more than 10^{-5} cm will be like the black-body one, due to suffice large “optical/photon thickness” of the plasma clots consisting of multicharge ions of heavy/multielectron atoms of elements like Fe, Si, O, etc. Such plasma blobs during their expansion become optically thin and hence can give line emission too.

The efficiency of conversion of the kinetic energy of colliding dust particles into the energy of X-ray photons, k_x , was calculated for the both cases taking into account both bremsstrahlung and recombination radiation mechanisms. It is found that the maximum value of the efficiency will be around $k_x = 0.1$. The most probable energy of photons from the cometary coma hot plasma clumps will raise at decreasing the comet heliocentric distance and change in the range 0.1–1 keV at the range of $R = 1$ –0.1 AU, respectively [7, 8, 9].

X-ray luminosity of dusty comets like comet Hyakutake 1996 B2 due to (d-d) process will be more than 10^{15} erg/s at $R < 1$ AU [10]. This value is close to the measured soft X-ray luminosity of comet Hyakutake 1996 B2 by ROSAT as $L_x(0.09$ – 2 keV, $R = 1$ AU) = 4×10^{15} erg/s, with strong temporal variations [6].

It should be noted that an essential contribution to the X-ray luminosity of comets can also give line emission due to recombination of multicharge ions of the solar wind plasma via charge exchange process with cometary coma atoms and molecules that occurs effectively near the cometopause [11].

The maximum brightness of the X-ray emission of the cometary gas-dust coma, produced by these radiation mechanisms, should be located/shifted in the direction to the Sun because gas-dust matter from the comet nucleus always is being ejected, basically, towards the Sun. It is compatible with observations of such bright comet as Mrkos 1957d/1957 V showed emissions of Na-atoms with anomalous distribution at high angular resolution, as well as with data of the Vega 1/2 and Giotto in situ television observations of comet Halley 1986 III (cf. [1, 2, 12, 13, 14]).

3 Conclusions

It is analytically shown that high-velocity collisions between cometary and interplanetary dust particles in the comas of dusty comets with retrograde and quasi-retrograde orbital motion, (d-d) process, will lead to generation of hot short-living dense plasma clumps in the inner heliosphere. Such component of the cometary atmospheres plasma is able to emit 0.1–1 keV photons, i.e., soft X-rays.

Modern soft X-ray space telescopes like ROSAT and XMM have carried out X-ray observations of comets only at heliocentric distances close and more than 1 AU. For revealing and identification of X-ray generation mechanisms of comets as well as using comets as natural space probes it is important appropriate observations of bright dusty comets in the inner heliosphere and determining the dependence of X-ray luminosity and spectra of comets on the heliocentric distance.

Acknowledgments. The author is grateful to the Organizing Committee of the International Conference “Sobolev100: Radiation Mechanisms of Astrophysical Objects: Classics Today” (St. Petersburg, Russia, September 21–25, 2015) for hospitality and financial support, Dr. G.M. Rudnitskij, SAI MSU for useful discussions.

References

1. *R.Z. Sagdeev, J. Blamont, A.A. Galeev et al.*, Nature, **321**, 259, 1986.
2. *R. Reinhard*, Nature, **321**, 313, 1986.
3. *S. Ibadov*, Proc. Int. Conf. on Cometary Exploration. Budapest: Hungar. Acad. Sci., 1983, p. 227.
4. *S. Ibadov*, Europ. Space Agen. Sp. Publ., **SP-250**, 377, 1986.
5. *S. Ibadov*, Europ. Space Agen. Sp. Publ., **SP-278**, 655, 1987.
6. *C.M. Lisse, K. Dennerl, J. Englhauser et al.*, Science, **274**, 205, 1996.
7. *S. Ibadov*, Icarus, **86**, 283, 1990.
8. *S. Ibadov*, Adv. Space Res., **17**, 93, 1996.
9. *S. Ibadov*, Physical Processes in Comets and Related Objects. Moscow: Cosmos-inform, 1996.

10. *S. Ibadov*, Proc. IAU Symp. No. 274. Advances in Plasma Astrophysics. Cambridge: Cambridge Univ. Press, 2011, p. 76.
11. *T.E. Cravens*, J. Geophys. Res. Lett., **24**, 105, 1997.
12. *G.L. Greenstein, C. Arpigny*, Astrophys. J., **135**, 892, 1962.
13. *S. Ibadov*, Comets Meteors, No. 37, 8, 1985.
14. *S. Ibadov*, 10th Europ. Reg. Astron. Meet. Prague: Czech. Acad. Sci., 1987, p. 51.

The Evolution of a Supermassive Retrograde Binary in an Accretion Disk

P.B. Ivanov^{1,2}, J.C.B. Papaloizou², S.-J. Paardekooper³,
A.G. Polnarev³

E-mail: *pbi20@cam.ac.uk*

In this contribution we discuss the main results of a study of a massive binary with unequal mass ratio, q , embedded in an accretion disk, with its orbital rotation being opposed to that of the disk. When the mass ratio is sufficiently large, a gap opens in the disk, but the mechanism of gap formation is very different from the prograde case. Inward migration occurs on a timescale of $t_{ev} \sim M_p/\dot{M}$, where M_p is the mass of the less massive component (the perturber), and \dot{M} is the accretion rate. When $q \ll 1$, the accretion takes place mostly onto the more massive component, with the accretion rate onto the perturber being smaller than, or of order of, $q^{1/3}\dot{M}$. However, this rate increases when supermassive binary black holes are considered and gravitational wave emission is important. We estimate a typical duration of time for which the accretion onto the perturber and gravitational waves could be detected.

1 Statement of the problem

Supermassive black hole binaries (SBBH) may form as a consequence of galaxy mergers (see, e.g., [6, 1]). Since the directions of the angular momenta associated with the motion of the binary and the gas in the accretion disk are potentially uncorrelated, the binary may be on either a prograde or retrograde orbit with respect to the orbital motion in the disk when it becomes gravitationally bound and starts to interact with it. The prograde case has been considered in many works beginning with [3] and [2]. The retrograde case has received much less attention, with relatively few numerical simulations available to date (see, e.g., [7]). However, the retrograde case may be as generic as the prograde case when the interaction of SBBH with an accretion disk is considered. Note that although the disk is likely to be inclined with respect to the binary orbital plane initially, alignment on a length scale corresponding to the so-called alignment radius is attained relatively rapidly, the direction of rotation of the disk gas being either retrograde or prograde with respect to orbital motion, depending on the initial inclination (see, e.g., [3]). Here we briefly review recent results on the evolution of retrograde SBBH published in detail in [4].

¹ Astro Space Centre, P.N. Lebedev Physical Institute, Moscow, Russia

² DAMTP, University of Cambridge, UK

³ Astronomy Unit, Queen Mary University of London, UK

2 Numerical simulations of massive retrograde perturbers embedded in an accretion disk

In this section we consider numerical simulations for which the perturber is massive enough to significantly perturb the accretion disk and open a surface density depression called hereafter “a gap” in the vicinity of its orbit. For that we require mass ratio, q , of the perturber with mass M_p to the dominant mass M , to be larger than $\sim 1.57(H/r_p)^2$, where r_p is the radius of perturber’s orbit and H is the disk semi-thickness. We consider values of $q = 0.01$ and 0.02 below. Note that the alternative case of a low mass perturber which is insufficiently massive to open a gap has been considered by [4]. The perturber was initiated on a retrograde circular orbit of radius r_0 which is taken to be the simulation unit of length. For simulation unit of time, we take the orbital period of a circular orbit with this radius, the disk aspect ratio was constant and equal to 0.05 , for other details see [4]. The structure of the disk gaps for $q = 0.02$ is illustrated in the surface density contour plots presented in Fig. 1 at various times. Note that an animation of the process of gap formation can be found on the website <http://astro.qmul.ac.uk/people/sijme-jan-paardekooper/publications>. The semi-major axis is shown as a function of time for $q = 0.02$ and $q = 0.01$ with a gravitational softening length of $b = 0.1H$ and for $q = 0.01$ with $b = 0.6H$ in Fig. 2. The behavior depends only very weakly on whether the perturber is allowed to accrete from the disk or not.

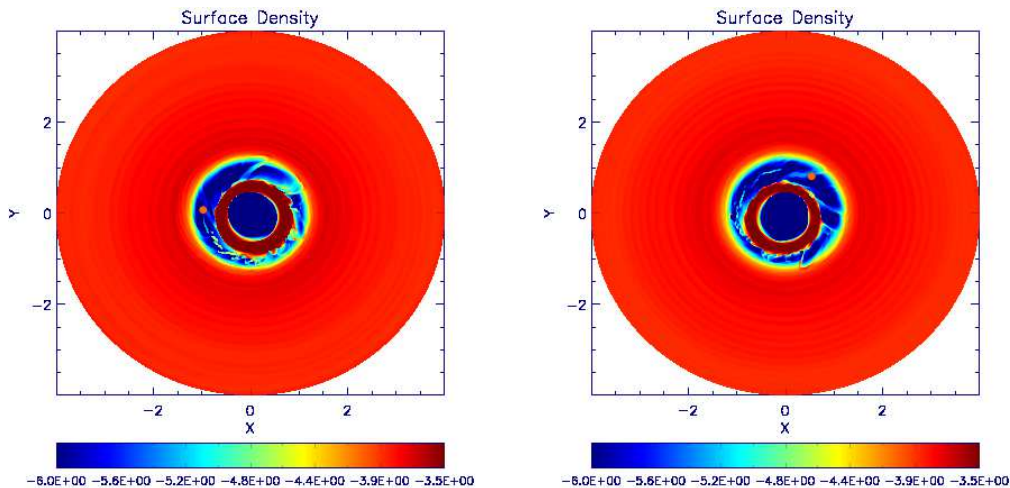


Figure 1: $\log \Sigma$ contours for $q = 0.02$ with softening length $0.1H$ after 50 orbits (left panel) and after 100 orbits (right panel). In these simulations the companion, its position in each case being at the center of the small red circle located within the gap region, was allowed to accrete. The width of the gaps slowly increases while the accretion rates, on average, slowly decrease with time. Short wavelength density waves in the outer disks are just visible. Note that values of $\log \Sigma$ below the minimum indicated on the color bar are plotted as that minimum value.

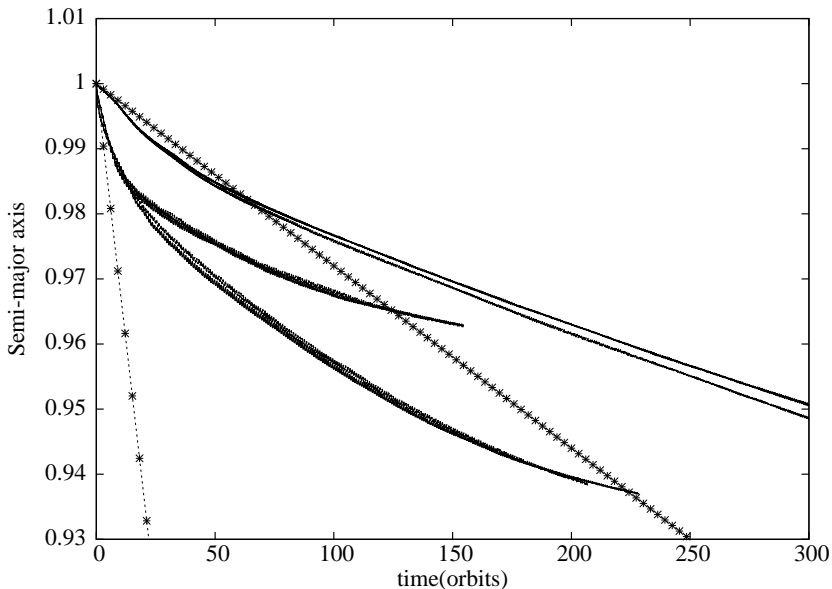


Figure 2: Semi-major axis, in units of the initial orbital radius, as a function of time for $q = 0.02$ and 0.01 with gravitational softening length $b = 0.1H$ and for $q = 0.01$ with $b = 0.6H$. Two curves without imposed crosses, which are very close together, are shown for each of these three cases. The uppermost pair of curves corresponds to $q = 0.01$ with $b = 0.6H$ and the lowermost pair to $q = 0.01$ with $b = 0.1H$. The central pair does to $q = 0.02$ with $b = 0.1H$. The lower of the pair of curves for the cases of $b = 0.1H$ corresponds to runs with accretion from the disk included. For the case of $b = 0.6H$, this situation is reversed. The straight lines which have imposed crosses are obtained adopting the initial Type I migration rate. The line with more widely separated crosses corresponds to $q = 0.01$ with $b = 0.1H$ while the other line corresponds to $q = 0.01$ with $b = 0.6H$.

3 Results

Our numerical results are confirmed by an analytic approach developed in [4]. In this paper the following general results have been obtained:

- 1) When the mass ratio q is small, but larger than $\sim 1.6(H/r_p)^2$ a gap in the vicinity of the perturber opens due to an increase of radial velocity of the gas in this region. Its size is smaller than the orbital distance r_p in this limit.
- 2) For such systems for which the perturber's mass is larger than a typical disk mass within a distance $\sim r_p$, the disk structure outside the gap is approximately quasi-stationary. The inner disk has nearly zero angular momentum flux, while the outer disk has an angular momentum flux equal to the product of the mass flux and the binary specific angular momentum. The orbital evolution timescale $t_{ev} = M_p/(2\dot{M})$ is then determined by conservation of angular momentum. Note that this picture differs from the prograde case with similar parameters, where there is a pronounced cavity instead of an inner disk and the orbital evolution is somewhat faster.

- 3) When the orbital evolution is determined by interaction with the disk, the mass flux onto the more massive component $\sim \dot{M}$, while the average mass flux onto the perturber is smaller $\sim q^{1/3} \dot{M}$. However, the latter exhibits strong variability on timescales on the order of the orbital period. The mass flux onto the perturber can increase significantly during the late stages of the inspiral of SBBH when the emission of gravitational waves controls the orbital evolution.
- 4) When the binary is sufficiently eccentric and the disk is sufficiently thin, the opening of a “conventional” cavity within the disk is also possible due to the presence of Lindblad resonances.

Additionally, we estimated a time duration for which the emitted gravitational waves would have sufficient amplitude for detection by a space-borne interferometric gravitational wave antenna with realistic parameters, as well as the appropriate range of frequencies as a function of the primary BH mass in [5].

Note that all these results have been obtained under the assumption that the binary orbit and the disk are coplanar. This may break down at late times. An estimate for the time required for their mutual inclination angle measured at large distances to change is given in [4] for an initially retrograde binary. The typical timescale is on the order of, or possibly even smaller than, t_{ev} depending on the mass ratio and disk parameters. Thus, this effect should be taken into account in future studies of these systems.

References

1. *M.C. Begelman, R.D. Blandford, M.J. Rees*, *Nature*, **287**, 307, 1980.
2. *A. Gould, H.-W. Rix*, *Astrophys. J. Lett.*, **532**, L29, 2000.
3. *P.B. Ivanov, J.C.B. Papaloizou, A.G. Polnarev*, *Mon. Not. Roy. Astron. Soc.*, **307**, 79, 1999.
4. *P.B. Ivanov, J.C.B. Papaloizou, S.-J. Paardekooper, A.G. Polnarev*, *Astron. Astrophys.*, **576**, A29, 2015.
5. *P.B. Ivanov, J.C.B. Papaloizou, S.-J. Paardekooper, A.G. Polnarev*, *Balt. Astron.*, **24**, 166, 2015.
6. *B.V. Komberg*, *Sov. Astron.*, **11**, 727, 1968.
7. *C.J. Nixon, A.R. King, J.E. Pringle*, *Mon. Not. Roy. Astron. Soc.*, **417**, L66, 2011.

Search for the Giant Pulses – an Extreme Phenomenon in Radio Pulsar Emission

A.N. Kazantsev^{1,2}, V.A. Potapov¹

E-mail: *kaz.prao@bk.ru*

Here we present results of our search for Giant Pulses (GPs) from pulsars of Northern Hemisphere. Our survey was carried out at a frequency of 111 MHz using the Large Phased Array (LPA) radio telescope. Up to now we have detected regular generation of strong pulses satisfying the criteria of GPs from 2 pulsars: B1133+16, B1237+25.

1 Introduction

Slow pulse-to-pulse variation of intensity is very typical for overwhelming majority of known pulsars. However, a handful of pulsars have mysterious mechanism which can break such a stability.

Phenomenon of generation GPs was first detected for Crab pulsar (B0531+21) [1] and the millisecond pulsar B1937+21 [2]. In following studies a set of typical characteristics of GPs was determined. These are: very narrow components in pulse's microstructure (up to several nanoseconds), high peak flux density (up to several MJy), and power-law distribution of the peak flux density of GPs. It is important to emphasize that B0531+21 and B1937+21 have very strong magnetic field on the light cylinder ($B_{LC} \approx 10^6$ G) and are considered as “classical” pulsars with GPs. In course of time, GPs were detected from 5 pulsars with very strong magnetic field on the light cylinder ($B_{LC} \approx 10^5$ – 10^6 G): B0218+42 [3], B0540–69 [4], B1821–24 [5], J1823–3021 [6] and B1957+20 [3].

However, later a similar phenomenon was detected (mostly at low radio frequencies between 40 and 111 MHz) for a set of pulsars with B_{LC} in the range from several to several hundreds Gauss: J0034–0721 [7], J0529–6652 [8], J0659+1414 [9], J0953+0755 [10, 11], J1115+5030 [12] and J1752+2359 [13].

In present work we describe the results of our observations that were held to search for new pulsars generating GPs or anomalous strong pulses at low radio frequencies.

¹ P.N. Lebedev Phys. Inst. of the RAS, Pushchino Radio Astronomy Observatory, Russia

² Pushchino State Institute of Natural Sciences, Russia

2 Observations and processing

The observations were made during 2012 and 2014 at the Pushchino Radio Astronomy Observatory with the Large Phased Array radio telescope. This is the transit telescope with the effective area of about 20000 ± 4000 m² in the zenith direction. The main frequency of the observations was 111 MHz with a bandwidth of 2.3 MHz (460×5 kHz channels digital receiver with post-detector DM (Dispersion Measure) removal). The sampling interval was 1.2288 ms and the duration of each observation session was about 3.5 min (153 periods of PSR B1237+25).

We have processed the results of 66 observational sessions containing 11 091 pulses of B1133+16 and 89 observational sessions containing 13 617 pulses of B1237+25.

Average pulse of pulsar was obtained by summing and averaging of all individual pulses during one session of pulsar's observation. We have analyzed every pulse with a peak flux density $> 4\sigma_{noise}$ and located at the phase of the average pulse. Pulses with peak flux density more than 30 peak flux density of the average (per session) pulse were marked as GPs candidates.

For PSR B1133+16 we calculated peak flux density distribution separately for two main components of the average pulse of pulsar.

3 Results and conclusion

B1133+16 and B1237+25 are active second period (normal) radio pulsars with multicomponent average pulses having two and five main components, respectively. B1133+16 has a rotational period $P = 1.1879$ s and $B_{LC} = 11.9$ G, for B1237+25 $P = 1.3824$ s and $B_{LC} = 4.14$ G. We have regularly observed strong pulses from each pulsar during entire period of our observation [14, 15].

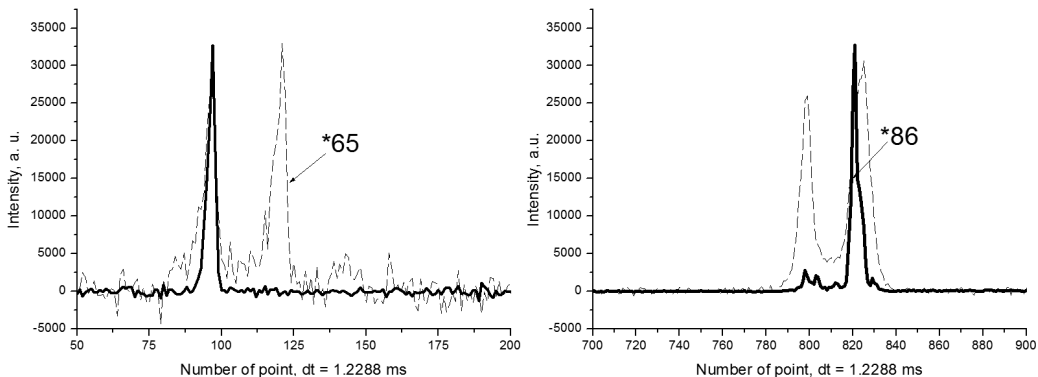


Figure 1: Strong pulses of PSR B1237+25 observed on May 14, 2012 (left panel), and of PSR B1133+16 observed on March 14, 2014 (right panel). The average pulse (dashed line) is shown multiplied by 65 and 86, respectively.

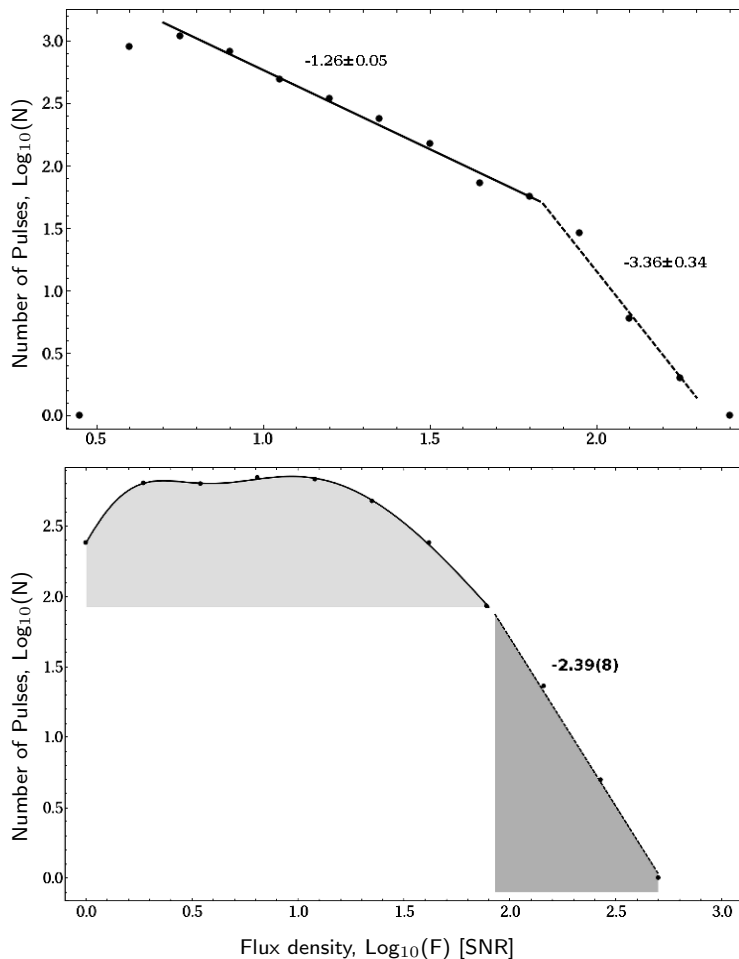


Figure 2: Histograms of distributions of the peak flux density of individual pulses for B1237+25 (top panel), and for the second (right-hand) component of B1133+16 (bottom panel) shown in the Log-Log scale. Data was fitted by the combination of two power-law distributions, and two log-normal plus power-law distribution, respectively.

An example of GPs from B1237+25 and B1133+16 are shown in Fig. 1. The most powerful GP of B1237+25 was detected on August 12, 2012, and has a flux density of 900 ± 130 Jy. There are around 12 GP events per 10000 pulses for B1237+25, and around 16 GP events per 10000 pulses for B1133+16.

The distribution of the peak flux density (in signal to noise ratio units) in the Log-Log scale is shown in Fig. 2. For B1237+25 distribution of the strong pulses has a bimodal power-law shape with exponents -1.26 ± 0.05 and -3.36 ± 0.34 , which is quite typical of GPs and obviously differs from log-normal individual pulses distribution of regular pulses. The distribution for B1133+16 has a complex character and may be fitted as a combination of two log-normal distributions for the first component of pulse and two log-normal and one power-law components with an exponent -2.39 ± 0.08 for the second.

We can conclude that strong individual pulses of PSR B1133+16 and PSR B1237+25 observed at 111 MHz satisfy the main criteria of GPs. It is worth noting that B1133+16 and PSR B1237+25 are pulsars with low magnetic field on light cylinder. This is the further confirmation of our earlier assumptions that such pulsars (including J0034–0721, J0529–6652, J0659+1414, J0953+0755, J1115+5030 and J1752+2359) may be referred as a sub-class of pulsars with GP, having low magnetic field on light cylinder and generating GPs mostly at low radio frequencies.

Acknowledgments. This work was supported by the Program of the Presidium of the Russian Academy of Sciences 41P “Transitional and explosive processes in astrophysics”, and by Scientific Educational Complex Program of P.N. Lebedev Institute of the RAS.

References

1. *D.N. Staelin, E.C. Reifstein*, IAU Astron. Telegram Circ., No. 2110, 1968.
2. *A. Wolszczan, J. Cordes, D. Stinebring*, NRAO Workshop, 1984, p. 63.
3. *B.C. Joshi, M. Kramer, A.G. Lyne et al.*, Proc. IAU Symp. No. 218, 2004, p. 319.
4. *S. Johnston, R.W. Romani*, Astrophys. J. Lett., **590**, L95, 2003.
5. *S. Johnston, R.W. Romani*, Astrophys. J. Lett., **557**, L93, 2001.
6. *H.S. Knight, M. Bailes, R.N. Manchester, S.M. Ord*, Astrophys. J., **625**, 951, 2005.
7. *A.D. Kuzmin, A.A. Ershov, B. Ya. Losovsky*, Astron. Lett., **30**, 247, 2004.
8. *F. Crawford, D. Altemose, H. Li, D.R. Lorimer*, Astrophys. J., **762**, 97, 2013.
9. *A.D. Kuzmin, A.A. Ershov*, Astron. Lett., **32**, 583, 2006.
10. *A.K. Singal*, Astrophys. Space Sci., **278**, 61, 2001.
11. *T.V. Smirnova*, Astron. Rep., **54**, 430, 2012.
12. *A.A. Ershov, A.D. Kuzmin*, Astron. Lett., **29**, 91, 2003.
13. *A.A. Ershov, A.D. Kuzmin*, Chin. J. Astron. Astrophys., **6**, 30, 2006.
14. *A.N. Kazantsev, V.A. Potapov*, Astron. Tsirk., **1620**, 1, 2015.
15. *A.N. Kazantsev, V.A. Potapov*, Astron. Tsirk., **1628**, 1, 2015.

Testing the Variation of Fundamental Constants by Astrophysical Methods: Overview and Prospects

S.A. Levshakov^{1,2}

E-mail: *lev@astro.ioffe.rssi.ru*

By measuring the fundamental constants in astrophysical objects one can test basic physical principles as space-time invariance of physical laws along with probing the applicability limits of the standard model of particle physics. The latest constraints on the fine structure constant α and the electron-to-proton mass ratio μ obtained from observations at high redshifts and in the Milky Way disk are reviewed. In optical range, the most accurate measurements have already reached the sensitivity limit of available instruments, and further improvements will be possible only with next generation of telescopes and receivers. New methods of the wavelength calibration should be realized to control systematic errors at the sub-pixel level. In radio sector, the main tasks are the search for galactic and extragalactic objects suitable for precise molecular spectroscopy as well as high resolution laboratory measurements of molecular lines to provide accurate frequency standards. The expected progress in the optical and radio astrophysical observations is quantified.

1 Introduction

The idea that the fundamental physical constants may vary on the cosmological time scale has been discussed since 1937, when Milne and Dirac argued about possible variations of the Newton constant G during the lifetime of the universe [1, 2]. Currently, the subject of the cosmological variation of fundamental constants is closely related to emergence considerations of different cosmological models inspired by the discovery of late time acceleration of the expansion of the universe [3, 4]. The possibility that dimensionless coupling constants such as electron-to-proton mass ratio $\mu = m_e/m_p$ and the fine structure constant $\alpha = e^2/\hbar c$ may roll with cosmic time has recently been reviewed in [5, 6, 7, 8].

The variation of fundamental constants would imply a violation of the Einstein equivalence principle (EEP), that is, local position invariance (LPI) and local Lorentz invariance (LLI). In particular, a changing α accompanied by variation in other coupling constants can be associated with a violation of LLI [9], and LPI postulates that the fundamental physical laws are space-time invariant.

¹ A.F. Ioffe Physical-Technical Institute, St. Petersburg, Russia

² St. Petersburg Electrotechnical University “LETI”, Russia

The standard model of particle physics (SM) is based on the EEP; thus, we can probe the applicability limits of the SM and new types of interactions by experimental validation of the EEP.

In spite of some claims that changes in α or μ were marginally detected at high redshifts, to date no confirmed variation of dimensionless coupling constants has been found on astronomical space-time scales. Below we review current observational constraints on α and μ variations which provide limits on the allowed deviations from the SM and Λ CDM cosmology.

2 Basics of the astronomical measurements

Two dimensionless coupling constants μ and α are of particular interest for astronomical studies since their fractional changes $\Delta\mu/\mu = (\mu_{\text{obs}} - \mu_{\text{lab}})/\mu_{\text{lab}}$, and $\Delta\alpha/\alpha = (\alpha_{\text{obs}} - \alpha_{\text{lab}})/\alpha_{\text{lab}}$ can be accurately measured from spectral line profiles of Galactic and extragalactic sources.

Differential measurements of $\Delta\mu/\mu$ and $\Delta\alpha/\alpha$ are based on the comparison of the line centers in the absorption/emission spectra of cosmic objects and the corresponding laboratory values. It was shown that electro-vibro-rotational lines of H_2 [10] and CO [11] have their own sensitivities to μ -variation. Similarly, each atomic transition is characterized by its individual sensitivity to α -variation [12]. The dependence of an atomic frequency ω on α in the comoving reference frame of a distant object located at redshift z is given by $\omega_z = \omega + qx + O(x^2)$, where $x \equiv (\alpha_z/\alpha)^2 - 1$. Here ω and ω_z are the frequencies corresponding to the present-day value of α and that at a redshift z . The so-called q factor is an individual parameter for each atomic transition [12]. If $\alpha_z \neq \alpha$, then $x \neq 0$ and the corresponding frequency shift $\Delta\omega = \omega_z - \omega$ is $\Delta\omega/\omega = Q\Delta\alpha/\alpha$, where $Q = 2q/\omega$ is the dimensionless sensitivity coefficient.

For two lines of the same element with the sensitivity coefficients Q_1 and Q_2 , the fractional changes $\Delta\mu/\mu$ and $\Delta\alpha/\alpha$ are equal to $\Delta v/(c\Delta Q)$, where $\Delta v = v_1 - v_2$ is the difference of the measured radial velocities of these lines, and $\Delta Q = Q_2 - Q_1$ is the corresponding difference between their sensitivity coefficients [13, 14].

The Q values of atomic transitions observed in quasar spectra are very small, $|Q| \ll 1$ [12]. Similar low sensitivity coefficients were calculated for electro-vibro-rotational transitions in H_2 and CO (for references, see [14]). Small values of Q and ΔQ put tough constraints on optical methods to probe $\Delta\alpha/\alpha$ and $\Delta\mu/\mu$. For instance, at $\Delta\alpha/\alpha \sim 10^{-5}$, the required line position accuracy must be $\sigma_v \lesssim 0.25 \text{ km s}^{-1}$ in accord with the inequality [14]: $\sigma_v/c < (\Delta Q/\sqrt{2})(\Delta\alpha/\alpha)$. A typical error of the line center measurements of an unsaturated absorption line in quasar spectra is about 1/10th of the pixel size [15]. For high redshift objects, the UV-Visual Echelle Spectrograph (UVES) at the ESO Very Large Telescope (VLT) provides a pixel size $\Delta\lambda_{\text{pix}} \sim 0.06 \text{ \AA}$ at $\lambda \sim 5000 \text{ \AA}$, that is $\sigma_v \sim 0.5 \text{ km s}^{-1}$, which is comparable to the velocity offset due to a fractional change in α at the level of 10^{-5} . This shows that special care and additional calibrations are

required to probe $\Delta\alpha/\alpha$ and $\Delta\mu/\mu$ at a level of 10^{-6} by optical methods. Such measurements have been carried out at the VLT/UVES as described in the next section.

3 VLT/UVES Large Program for testing fundamental physics

The ESO Large Programme 185.A–0745 (2010–2013) was especially aimed at testing the hypothetical variability of physical constants [16, 17, 18, 19]. Its prime goal was to study systematic errors in wavelength scales of quasar spectra. For this purpose, quasars were observed almost simultaneously with bright asteroids, whose reflected sunlight spectra contain many narrow features with positions as accurate as a few m s^{-1} [20]. Additionally, bright stars were observed through an iodine gas absorption cell, providing a precise transfer function for part of the wavelength range.

As a result, there were revealed distortions of the wavelength scale with a jigsaw pattern and peak-to-peak amplitude of several hundreds m s^{-1} along the echelle orders. The presence of long range wavelength dependent velocity drifts ranging between ~ 0.5 and 1.0 km s^{-1} and showing opposite sign as compared with the Keck/HIRES spectra of quasars was found as well [21].

A stringent bound for $\Delta\alpha/\alpha$ was obtained for the absorber at $z_{\text{abs}} = 1.69$ towards the quasar HE2217–2818 [16]. The fractional change of α in this system is $\Delta\alpha/\alpha = (1.3 \pm 2.4_{\text{stat}} \pm 1.0_{\text{sys}}) \times 10^{-6}$ if AlII $\lambda 1670 \text{ \AA}$ and three FeII transitions are used, and $\Delta\alpha/\alpha = (1.1 \pm 2.6_{\text{stat}}) \times 10^{-6}$ in a slightly different analysis with only FeII transitions used. Together with another system observed with the UVES/VLT at $z_{\text{abs}} = 1.58$ towards HE0001–2340 where $\Delta\alpha/\alpha = (-1.5 \pm 2.6_{\text{stat}}) \times 10^{-6}$ [22], and eight HIRES/Keck quasar absorbers with the mean $\Delta\alpha/\alpha = (-0.1 \pm 2.6) \times 10^{-6}$ [23], these values are the tightest bounds to date on α -variation at high redshifts. As seen, they do not show any evidence for changes in α at the precision level of $\sim 3 \times 10^{-6}$ (1σ confidence level, C.L.).

For the electron-to-proton mass ratio, the analysis of the H_2 absorption lines of the $z_{\text{abs}} = 2.40$ damped Ly- α system towards HE0027–1836 yields $\Delta\mu/\mu = (2.5 \pm 8.1_{\text{stat}} \pm 6.2_{\text{sys}}) \times 10^{-6}$ [17]. When corrections to the wavelength dependent velocity drift are applied then $\Delta\mu/\mu = (7.6 \pm 8.1_{\text{stat}} \pm 6.3_{\text{sys}}) \times 10^{-6}$. At higher redshift $z_{\text{abs}} = 4.22$ the analysis of H_2 absorption lines in the spectrum of J1443+2724 gives $\Delta\mu/\mu = (9.5 \pm 5.4_{\text{stat}} \pm 5.3_{\text{sys}}) \times 10^{-6}$ [24]. These results are consistent with a null μ -variation at the $\sim 2 \times 10^{-5}$ (1σ C.L.) precision level over a lookback time of $\approx 12.4 \text{ Gyr}$ (10% of the age of the Universe today).

4 Microwave and submillimeter molecular transitions

Radio astronomical observations allow us to probe variation of the fundamental constants on the cosmological time scale at a level deeper than 10^{-5} . In the microwave range there are a good deal of molecular transitions arising

in galactic and extragalactic sources. Electronic, vibrational, and rotational energies in molecular spectra are scaled as $E_{\text{el}} : E_{\text{vib}} : E_{\text{rot}} = 1 : \mu^{1/2} : \mu$. This means that the sensitivity coefficients for pure vibrational and rotational transitions are equal to $Q_{\text{vib}} = 0.5$ and $Q_{\text{rot}} = 1$. Molecules have also fine and hyperfine structures, Λ -doubling, hindered rotation, accidental degeneracy between narrow close-lying levels of different types and all of them have a specific dependence on the physical constants. Some of these molecular transitions are ~ 100 times more sensitive to variations of μ and α than atomic, and electro-vibro-rotational transitions of H_2 and CO which are detected in six quasar absorbers between $z = 1.6$ and 2.7 [25]. In addition, positions of narrow molecular lines arising from cold dark clouds in the Milky Way disk can be measured with uncertainties of $\sigma_v \lesssim 0.01 \text{ km s}^{-1}$ [26], that is, the resulting sensitivity in radio bands is about three orders of magnitude higher as compared with optical spectra.

The molecular transitions with enhanced sensitivity coefficients which are the prime targets for testing the constancy of the fundamental constants by radio astronomical methods were recently reviewed in [14]. For instance, inversion transitions of ammonia NH_3 – one of the most abundant molecules in the interstellar medium – have sensitivity coefficients $Q_\mu = 4.5$ [27]. This enhancement occurs due to the tunneling effect depending on the action S which is proportional to μ^{-1} : the ground state tunneling frequency $\omega \propto e^{-S}$. Observations of the $\text{NH}_3(1,1)$ inversion line and five HC_3N rotational lines at $z_{\text{abs}} = 0.89$ towards PKS1830–211 [28], as well as the inversion (NH_3) and rotational (CS , H_2CO) lines at $z_{\text{abs}} = 0.69$ towards B0218+357 [29] led to constraints (1σ C.L.): $|\Delta\mu/\mu| < 5 \times 10^{-7}$ and $|\Delta\mu/\mu| < 1 \times 10^{-7}$, respectively.

The second molecule which is extremely sensitive to μ -variation and which is observed in galactic and extragalactic molecular clouds is methanol CH_3OH . The sensitivity coefficients Q_μ for different transitions in CH_3OH range from -53 to 42 [30, 31]. A distinctive feature of methanol is strong interaction between the internal (hindered) and overall rotations. Transitions, in which both the internal and overall rotation states are changed, have strongly enhanced Q_μ -factors. However, the magnetic hyperfine structure of methanol transitions which was partly resolved in laboratory measurements [32] puts natural restriction on the methanol method at the level of $\sim 10^{-8}$ in $\Delta\mu/\mu$ tests. The hyperfine coupling in methanol is due to the well known magnetic spin-rotation and spin-spin couplings leading to small line splittings of ~ 10 kHz. The large amplitude internal rotation may also lead to a less known magnetic coupling – the so-called spin-torsion coupling – which has not yet been conclusively evidenced.

So far, methanol absorption lines were detected at $z_{\text{abs}} = 0.89$ in the gravitationally lensed system PKS1830–211 [33]. This system provides the most stringent limit on changes in μ over a lookback time of ≈ 7.5 Gyr: $|\Delta\mu/\mu| < 2 \times 10^{-7}$ (1σ C.L.) [34].

Cold ($T_{\text{kin}} \sim 10$ K) and dense ($n_{\text{H}_2} \sim 10^4 \text{ cm}^{-3}$) molecular cores in the Milky Way disk are another perspective targets to probe μ . The molecular cores are the ammonia emitters exhibiting some of the narrowest ($\Delta v \lesssim 0.2 \text{ km s}^{-1}$ (FWHM))

lines ever observed [35, 36]. The NH_3 line widths Δv of some of them correspond to a pure thermal broadening at a minimum gas temperature of $T_{\text{kin}} \approx 8$ K coming mainly from the heating by cosmic rays [37]. A lifetime of molecular cores is $\sim 10^{6-7}$ yr [38], and they are located at regions with different gravitational potentials.

A sample of the molecular cores were studied with the Medicina 32-m, Nobeyama 45-m, and Effelsberg 100-m telescopes in [26, 39, 40]. The main result of these measurements is the most stringent limit on μ -variation for the period of $\sim 10^{6-7}$ yr obtained by astronomical methods [26]: $|\Delta\mu/\mu| < 7 \times 10^{-9}$ (1 σ C.L.). This upper limit is comparable with the current constraint stemming from laboratory experiments, $\dot{\mu}/\mu < 6 \times 10^{-16}$ yr $^{-1}$ [41].

An independent test that α and μ may differ between the high- and low-density environments of the Earth and the interstellar medium was performed with CH and OH in [42]. In the Milky Way, the strongest limit to date on α -variation is $|\Delta\alpha/\alpha| < 1.4 \times 10^{-7}$ (1 σ C.L.).

Thus, the Einstein heuristic principle of LPI is validated all over the universe, that is, neither α at the level of $\sim \text{few} \times 10^{-6}$, no μ at the level of $\sim \text{few} \times 10^{-7}$ deviates from its terrestrial value for the passed 10^{10} yr. Locally, no statistically significant deviations of $\Delta\mu/\mu$ from zero were found at even more deeper level of $\sim \text{few} \times 10^{-9}$. For the fine structure constant, such limit is $\sim 10^{-7}$.

5 Future prospects

In previous sections we demonstrated that the radio observations of NH_3 and CH_3OH lines are an order of magnitude more sensitive to fractional changes in μ than the optical constraints derived from H_2 . However, at cosmological distances there are only five radio molecular absorbers known and all of them are located at $z < 1$, whereas H_2 lines are detected at redshifts $2 \lesssim z \lesssim 4$.

As was emphasized in [14], the improvements in measurements of $\Delta\alpha/\alpha$ and $\Delta\mu/\mu$ at the level of, respectively, 10^{-8} and 10^{-9} , can be achieved if two main requirements will be fulfilled: (i) increasing precision of the laboratory measurements of the rest frame frequencies of the most sensitive molecular transitions, and (ii) increasing sensitivity and spectral resolution of astronomical observations.

The second requirement is expected to be realized in a couple of years when the Next Generation Very Large Array (ngVLA) will start regular operations [43]. The ngVLA will provide ten times the effective collecting area of the JVLA and ALMA, operating from 1 GHz to 115 GHz, with ten times longer baselines (300 km). The increased sensitivity of the ngVLA by an order of magnitude over the VLA would allow discovery of new molecular absorbers at $z > 1$ and, thus, would extend the sample of targets suitable to test the EEP at early cosmological epochs.

In optical sector, the forthcoming generation of new optical telescopes such as the Thirty Meter Telescope (TMT) and the European Extremely Large

Telescope (E-ELT) equipped by high-resolution ultra-stable spectrographs will significantly improve the constancy limits of fundamental couplings. The future high precision optical measurements should achieve sensitivities of $\sim 10^{-7}$ for individual absorbers. Thanks to a large sample of absorption-line systems, a few times deeper limit is expected for the ensemble average.

In spite of a far higher sensitivity of radio methods as compared to that of next-generation optical facilities, the unresolved (or partly resolved) magnetic hyperfine structure of molecular transitions prevents the radio measurements to achieve the accuracy better than $\sim 10^{-9}$.

For example, the hyperfine structure of several transitions in methanol CH_3OH was recently recorded in the microwave domain using the Fourier transform microwave (FT-MW) spectrometer in Hannover and the molecular beam FT-MW spectrometer in Lille [32]. With the line splitting of ~ 10 kHz revealed in these laboratory studies, and the difference between the sensitivity coefficients $\Delta Q_\mu \sim 10$ for the 48.372, 48.377, and 60.531 GHz methanol lines observed at $z_{\text{abs}} = 0.89$ towards PKS1830–211 [34], one finds the uncertainty of $\Delta\mu/\mu$ of about 3×10^{-8} , which is entirely caused by the unresolved hyperfine structure of methanol lines.

It should be obvious that further progress in radio sector is in need of accurate laboratory measurements of the rest frame molecular frequencies. The required uncertainty of laboratory frequencies is $\lesssim 1 \text{ m s}^{-1}$. There is currently a shortage of such data. Among molecules with high sensitivity coefficients to changes in μ and α only NH_3 [44] and CH [42, 45] transitions fulfill this requirement.

6 Conclusions

In this short review we highlighted the most important observational results which mark the frontier of most precise spectroscopic measurements of line positions in optical and radio sectors aimed at different tests of the variation of fundamental physical constants by astrophysical methods.

Current null results from the VLT and Keck optical telescopes as well as from different radio telescopes validate the Einstein equivalence principle at a rather deep level of $\sim 10^{-7} - 10^{-6}$ for extragalactic sources and at $\sim 10^{-8}$ within the Milky Way disk. This is a tremendous step forward in experimental justification of basic principles of the general relativity and the standard model of particle physics as compared with the first astrophysical constraint on $|\Delta\alpha/\alpha| < 3 \times 10^{-3}$ towards radio galaxy Cygnus A ($z = 0.057$) obtained 60 years ago by Savedoff [46].

It should be emphasized that both optical and radio methods complement each other and in future will provide independent tests of $\Delta\alpha/\alpha$ and $\Delta\mu/\mu$ variability using the next-generation radio and optical telescopes.

References

1. *E.A. Milne*, Proc. Roy. Soc. A., **158**, 324, 1937.
2. *P.A.M. Dirac*, Nature, **139**, 323, 1937.

3. *A.G. Riess, A.V. Filippenko, P. Challis et al.*, *Astron. J.*, **116**, 1009, 1998.
4. *S. Perlmutter, G. Aldering, G. Goldhaber et al.*, *Astrophys. J.*, **517**, 565, 1999.
5. *J.-P. Uzan*, *Living Rev. Rel.*, **14**, 2, 2011.
6. *S. Liberati*, *Class. Quant. Grav.*, **30**, 133001, 2013.
7. *C.J.A.P. Martin*, *Gen. Rel. Grav.*, **47**, 1843, 2014.
8. *M. Martinelli, E. Calabrese, C.J.A.P. Martin*, *J. Cosmol. Astropart. Phys.*, **11**, 030, 2015.
9. *V.A. Kostelecký, R. Lehnert, M.J. Perry*, *Phys. Rev. D*, **68**, 123511, 2003.
10. *D.A. Varshalovich, S.A. Levshakov*, *J. Exp. Theor. Phys.*, **58**, 231, 1993.
11. *E.J. Salumbides, M.L. Niu, J. Bagdonaitė et al.*, *Phys. Rev. A*, **86**, 022510, 2012.
12. *V.A. Dzuba, V.V. Flambaum, J.K. Webb*, *Phys. Rev. Lett.*, **82**, 888, 1999.
13. *S.A. Levshakov, M. Dessauges-Zavadsky, S. D'Odorico, P. Molaro et al.*, *Mon. Not. Roy. Astron. Soc.*, **333**, 373, 2002.
14. *M.G. Kozlov, S.A. Levshakov*, *Ann. Phys.*, **525**, 452, 2013.
15. *S.A. Levshakov, M. Centurión, P. Molaro, S. D'Odorico*, *Astron. Astrophys.*, **434**, 827, 2005.
16. *P. Molaro, M. Centurión, J.B. Whitmore et al.*, *Astron. Astrophys.*, **555**, 68, 2013.
17. *H. Rahmani, R. Srianand, N. Gupta et al.*, *Mon. Not. Roy. Astron. Soc.*, **425**, 556, 2013.
18. *P. Bonifacio, H. Rahmani, J.B. Whitmore et al.*, *Astron. Nachr.*, **335**, 83, 2014.
19. *T.M. Evans, M.T. Murphy, J.B. Whitmore et al.*, *Mon. Not. Roy. Astron. Soc.*, **445**, 128, 2014.
20. *P. Molaro, S.A. Levshakov, S. Monai et al.*, *Astron. Astrophys.*, **481**, 559, 2008.
21. *J.B. Whitmore, M.T. Murphy*, *Mon. Not. Roy. Astron. Soc.*, **447**, 446, 2015.
22. *I.I. Agafonova, P. Molaro, S.A. Levshakov, J.L. Hou*, *Astron. Astrophys.*, **529**, A28, 2011.
23. *A. Songaila, L.L. Cowie*, *Astrophys. J.*, **793**, 103, 2014.
24. *J. Bagdonaitė, W. Ubachs, M.T. Murphy, J.B. Whitmore*, *Phys. Rev. Lett.*, **114**, 071301, 2015.
25. *P. Noterdaeme, P. Petitjean, R. Srianand et al.*, *Astron. Astrophys.*, **526**, L7, 2011.
26. *S.A. Levshakov, D. Reimers, C. Henkel et al.*, *Astron. Astrophys.*, **559**, A91, 2013.
27. *V.V. Flambaum, M.G. Kozlov*, *Phys. Rev. Lett.*, **98**, 240801, 2007.
28. *C. Henkel, K.M. Menten, M.T. Murphy et al.*, *Astron. Astrophys.*, **500**, 725, 2009.
29. *N. Kanekar*, *Astrophys. J. Lett.*, **728**, L12, 2011.
30. *P. Jansen, L.-H. Xu, I. Kleiner et al.*, *Phys. Rev. Lett.*, **106**, 100801, 2011.

31. *S.A. Levshakov, M.G. Kozlov, D. Reimers*, *Astrophys. J.*, **738**, 26, 2011.
32. *L.H. Coudert, C. Gutlé, T.R. Huet et al.*, *J. Chem. Phys.*, **143**, 044304, 2015.
33. *S. Muller, A. Beelen, M. Guélin et al.*, *Astron. Astrophys.*, **535**, A103, 2011.
34. *N. Kanekar, W. Ubachs, K.M. Menten et al.*, *Mon. Not. Roy. Astron. Soc.*, **448**, L104, 2015.
35. *J. Jijina, P.C. Hyers, F.C. Adams*, *Astrophys. J. Suppl.*, **125**, 161, 1999.
36. *S.A. Levshakov, D. Reimers, C. Henkel*, *Astron. Astrophys.*, **586**, A126, 2016.
37. *P.F. Goldsmith, W.D. Langer*, *Astrophys. J.*, **222**, 881, 1978.
38. *C.W. Lee, P.C. Myers*, *Astrophys. J. Suppl.*, **123**, 233, 1999.
39. *S.A. Levshakov, P. Molaro, A.V. Lapinov et al.*, *Astron. Astrophys.*, **512**, A44, 2010.
40. *S.A. Levshakov, A.V. Lapinov, C. Henkel et al.*, *Astron. Astrophys.*, **524**, A32, 2010.
41. *M.C. Ferreira, M.D. Julião, C.J.A.P. Martins et al.*, *Phys. Rev. D*, **86**, 125025, 2012.
42. *S. Truppe, R.J. Hendricks, S.K. Tokunaga et al.*, *Nature Commun.*, **4**, 2600, 2013.
43. *G.C. Bower, P. Demorest, J. Braatz et al.*, *arXiv: astro-ph.HE/1510.06432*, 2015.
44. *S.G. Kukolich*, *Phys. Rev.*, **156**, 83, 1967.
45. *S. Truppe, R.J. Hendricks, S.K. Tokunaga et al.*, *J. Molec. Spectrosc.*, **300**, 70, 2014.
46. *M.P. Savedoff*, *Nature*, **178**, 688, 1956.

A Viscous-Convective Instability in Laminar Keplerian Thin Discs

K.L. Malanchev^{1,2}, K.A. Postnov^{1,2}, N.I. Shakura¹

E-mail: *malanchev@physics.msu.ru*

Using the anelastic approximation of linearized hydrodynamic equations, we investigate the development of axially symmetric small perturbations in thin Keplerian discs. Dispersion relation is found as a solution of general Sturm–Liouville eigenvalue problem for different values of relevant physical parameters (viscosity, heat conductivity, disc semi-thickness). The analysis reveals the appearance of overstable mode for Prandtl parameter higher than some critical value. These modes have a viscous-convective nature and can serve as a seed for turbulence in astrophysical discs even in the absence of magnetic fields.

1 Introduction

The problem of linear stability of sheared astrophysical flows has been actively studied. The recent papers [1] and [2] used the Boussinesq and anelastic approximations, respectively, with taking into account microscopic viscosity and thermal conductivity of the gas. These analyses have revealed the presence of overstable viscous modes whose physical origin is likely to be connected to development of convective motions in vertically stratified accretion flows. However, in those papers averaging over vertical disc structure was performed, which restricted applications of the obtained results. In the present paper, we take into account more realistic polytropic structure of a Keplerian accretion disc and solve linearized general Sturm–Liouville eigenvalue problem. Our analysis confirms the appearance of the overstable modes in the wide range of microscopic parameters of the gas described by the Prandtl number.

2 Basic equations

The system of hydrodynamic equations for axially symmetric accretion flow can be written as follows:

¹ M.V. Lomonosov Moscow State University, Sternberg Astronomical Institute, Russia

² M.V. Lomonosov Moscow State University, Faculty of Physics, Russia

1. Continuity equation

$$\frac{\partial \rho}{\partial t} + \frac{1}{r} \frac{\partial(\rho r u_r)}{\partial r} + \frac{\partial(\rho u_z)}{\partial z} = 0. \quad (1)$$

The anelastic approximation for gas velocity is \mathbf{u} is $\nabla \cdot \rho_0 \mathbf{u} = 0$.

2. The radial, azimuthal and vertical components of the Navier–Stokes momentum equation are, respectively,

$$\frac{\partial u_r}{\partial t} + u_r \frac{\partial u_r}{\partial r} + u_z \frac{\partial u_r}{\partial z} - \frac{u_\phi^2}{r} = -\frac{\partial \phi_g}{\partial r} - \frac{1}{\rho} \frac{\partial p}{\partial r} + \mathcal{N}_r, \quad (2)$$

$$\frac{\partial u_\phi}{\partial t} + u_r \frac{\partial u_\phi}{\partial r} + u_z \frac{\partial u_\phi}{\partial z} + \frac{u_r u_\phi}{r} = \mathcal{N}_\phi, \quad (3)$$

$$\frac{\partial u_z}{\partial t} + u_r \frac{\partial u_z}{\partial r} + u_z \frac{\partial u_z}{\partial z} = -\frac{\partial \phi_g}{\partial z} - \frac{1}{\rho} \frac{\partial p}{\partial z} + \mathcal{N}_z, \quad (4)$$

where \mathcal{N}_r , \mathcal{N}_ϕ and \mathcal{N}_z are viscous forces. For their specific form see for instance [3].

In this work we will drop the second derivatives of velocities u with respect to the vertical coordinate z in the Navier–Stokes equations following [2]. This assumption makes the problem simpler and the more general problem will be solved in [4].

3. Energy equation

$$\frac{\rho R T}{\mu} \left[\frac{\partial s}{\partial t} + (\mathbf{u} \nabla) \cdot s \right] = Q_{\text{visc}} - \nabla \cdot \mathbf{F}, \quad (5)$$

where s is specific entropy per particle, Q_{visc} is the viscous dissipation rate per unit volume, R is the universal gas constant, μ is the molecular weight, T is the temperature and terms on the right stand for the viscous energy production and the heat conductivity energy flux F , respectively. The energy flux due to the heat conductivity is

$$\nabla \cdot \mathbf{F} = \nabla(-\kappa \nabla T) = -\kappa \Delta T - \nabla \kappa \cdot \nabla T. \quad (6)$$

In the Boussinesq approximation, in the energy equation the Eulerian perturbations should be zero: $p_1 = 0$. Following [1], we will also drop the term $\nabla \kappa \cdot \nabla T$ but keep $\kappa \Delta T$.

3 Linearized equations in the anelastic approximation

The perturbed hydrodynamic variables can be written in the form $x = x_0 + x_1$, where x_0 stands for the unperturbed background quantities and $x_1 = (\rho_1, p_1, u_r, u_z, u_\phi)$ are small perturbations. We take all these small perturbations in the form $x_1 = f(z) \exp(i\omega t - ik_r r)$. We will consider thin discs with semi-thickness $z_0/r \ll 1$ and relatively large radial wavenumbers of perturbations $k_r r \gg 1$. Small thickness of the disc and large wavenumbers allow us to set the radial derivatives to zero, $\partial x_0/\partial r = 0$. Under these assumptions, linearizing of the system of equations (1–5) yields the following system of equations [1, 2]:

1. Continuity equation

$$\frac{\partial u_z}{\partial z} - ik_r u_r + \frac{1}{\rho_0} \frac{\partial \rho_0}{\partial z} u_z = 0. \tag{7}$$

2. Momentum equations

$$(i\omega + \nu k_r^2) u_r - 2\Omega u_\phi = ik_r \frac{p_1}{\rho_0}, \tag{8}$$

$$(i\omega + \nu k_r^2) u_\phi + \frac{\varkappa^2}{2\Omega} u_r = 0, \tag{9}$$

$$(i\omega + \nu k_r^2) u_z = -\frac{1}{\rho_0} \frac{\partial p_1}{\partial z} + \frac{\rho_1}{\rho_0} \frac{1}{\rho_0} \frac{\partial p_0}{\partial z}. \tag{10}$$

3. Energy equation

$$\begin{aligned} \frac{\rho_1}{\rho_0} \left[i\omega + \frac{\nu k_r^2}{\text{Pr}} - \alpha_{\text{visc}} \frac{\nu}{\text{Pr} T_0} \frac{\partial^2 T_0}{\partial z^2} - \alpha_{\text{visc}} \nu \left(r \frac{d\Omega}{dr} \right)^2 \frac{\mu}{\mathcal{R} T_0} \right] \\ = \frac{2ik_r \nu r (d\Omega/dr)}{c_p \mathcal{R} T_0 / \mu} u_\phi + \frac{1}{c_p} \frac{\partial s_0}{\partial z} u_z, \end{aligned} \tag{11}$$

where Pr is the Prandtl number, \mathcal{R} is the universal gas constant, \varkappa is the epicyclic frequency, $\nu \sim T_0^{\alpha_{\text{visc}}} / \rho_0$ is the kinematic viscosity coefficient. The kinematic viscosity in the disc equatorial plane is $\nu|_{z=0} = (v_s/v_\phi) (l/r) \Omega r^2$, where v_s is the sound velocity and l is the mean free path of particles. We assume the gas to be fully ionized so that $\alpha_{\text{visc}} = 5/2$.

It is necessary to set the background solution of hydrodynamic equations to find solution for perturbations. As the background state, we will use adiabatic polytropic discs [5]

$$\begin{aligned} T_0(z) = T_c \left(1 - \left(\frac{z}{z_0} \right)^2 \right), \quad \rho_0(z) = \rho_c \left(1 - \left(\frac{z}{z_0} \right)^2 \right)^{3/2}, \\ p_0(z) = p_c \left(1 - \left(\frac{z}{z_0} \right)^2 \right)^{5/2}, \quad s_0(z) = c_p \log \left(\frac{p_0^{3/5}}{\rho_0} \right) = \text{const.} \end{aligned}$$

This system of algebraic and differential equations can be transformed to one second-order differential equation for pressure perturbations p_1

$$\frac{\partial^2 p_1}{\partial z^2} - \alpha(\omega) \frac{z}{z_0^2} \frac{\partial p_1}{\partial z} - (\alpha(\omega) + \beta(\omega)) \frac{1}{z_0^2} p_1 = 0, \quad (12)$$

where $z_0 = \sqrt{3}(v_s/v_\phi)r$ is the disc semi-thickness [5], and the dimensionless coefficients α and β reads

$$\alpha(\omega) = \left(\frac{v_s}{v_\phi}\right) \left(\frac{l}{r}\right) \frac{\varkappa^2}{(i\omega + \nu k_r^2)^2} \times \frac{(-d \ln \Omega / d \ln r)}{c_p \left[i\omega + \frac{\nu k_r^2}{\text{Pr}} + 2 \frac{\alpha_{\text{visc}} \nu}{z_0^2} \frac{\nu}{T_0} - \alpha_{\text{visc}} \nu \left(r \frac{d\Omega}{dr} \right)^2 \frac{\mu}{\mathcal{R}T_0} \right]}{1 + \frac{(k_r r)^2}{(i\omega + \nu k_r^2)^2}}, \quad (13)$$

$$\beta(\omega) = \frac{(k_r r)^2}{1 + \frac{\varkappa^2}{(i\omega + \nu k_r^2)^2}}, \quad (14)$$

The pressure perturbation p_1 must vanish at the disc boundary ($z = z_0$), and the function $p_1(z)$ should be even or odd because of the plane symmetry of the problem. Bellow we will consider the case of even $p_1(z)$ with the boundary conditions

$$\left. \frac{\partial p_1}{\partial z} \right|_{z=0} = 0, \quad (15)$$

$$p_1|_{z=z_0} = 0. \quad (16)$$

We are searching for the least oscillating solutions, which means that $p_1(z)$ should not have zeros between $z = 0$ and $z = z_0$. This condition comes from our previous assumption about the smallness of the secondary derivatives of velocities in the Navier–Stokes equations (2–4).

Using a new variable $x \equiv z/z_0$, equation (12) transforms to

$$\frac{\partial^2 p_1}{\partial x^2} - \alpha(\omega) \frac{\partial p_1}{\partial x} - (\alpha(\omega) + \beta(\omega)) p_1 = 0. \quad (17)$$

Let us introduce a new function $Y(x)$

$$Y \equiv p_1 \exp\left(\frac{1}{2} \int_0^x -\alpha(\omega) x' dx'\right) = p_1 \exp\left(-\frac{\alpha(\omega) x^2}{4}\right). \quad (18)$$

Then (17) transforms to

$$\frac{\partial^2 Y}{\partial x^2} + \left(-\beta(\omega) - \frac{\alpha(\omega)}{2} - \frac{\alpha^2(\omega) x^2}{4}\right) Y = 0. \quad (19)$$

After introducing the new variable $\zeta \equiv \sqrt{\alpha(\omega)} x$, the eigenvalue problem (12), (15), (16) takes the form

$$\frac{\partial^2 Y}{\partial \zeta^2} - \left(\frac{\zeta^2}{4} + \left[\frac{\beta(\omega)}{\alpha(\omega)} + \frac{1}{2} \right] \right) Y = 0, \tag{20}$$

$$\left. \frac{\partial Y}{\partial \zeta} \right|_{\zeta=0} = 0, \tag{21}$$

$$Y|_{\zeta=\sqrt{\alpha(\omega)}} = 0. \tag{22}$$

Our boundary condition (21) and the plane symmetry of the problem enable us to use an even solution of equation (20) [6]

$$\begin{aligned} Y_\eta(\zeta) &= e^{-\zeta^2/4} M\left(-\frac{\eta}{2}, \frac{1}{2}, \frac{\zeta^2}{2}\right) \\ &= e^{-\zeta^2/4} \left\{ 1 + (-\eta) \frac{\zeta^2}{2!} + (-\eta)(-\eta + 2) \frac{\zeta^4}{4!} + \dots \right\}, \end{aligned} \tag{23}$$

where M is the confluent hypergeometric function, $\eta(\omega) \equiv -1 - \beta(\omega)/\alpha(\omega)$.

An eigenfunction of the problem (with the boundary condition (22)) must satisfy the following relation:

$$Y_{\eta(\omega)}(\sqrt{\alpha(\omega)}) = 0. \tag{24}$$

The last relation can be regarded as an equation for the unknown variable ω , then the solutions to this equations are eigenvalues of our problem, and the corresponding $Y_\eta(\zeta)$ will be its eigenfunctions.

4 Dispersion relation

Solution of the eigenvalue problem depends of the sign of the linearized term $\kappa \Delta T$, which appears in the energy equation (11) in the form

$$\alpha_{\text{visc}} \frac{\nu}{\text{Pr}} \frac{1}{T_0} \frac{\partial^2 T_0}{\partial z^2} + \alpha_{\text{visc}} \nu \left(r \frac{d\Omega}{dr} \right)^2 \frac{\mu}{\mathcal{R}T_0}. \tag{25}$$

If the Prandtl number $\text{Pr} \leq 8/45$ and this relation is negative, there is only one mode of the dispersion equation which corresponds to a decaying mode (see Fig. 1). Otherwise, if $\text{Pr} > 8/45$, an additional overstable mode appears (see Fig. 2).

Fig. 3 shows the dependence of $\text{Im}(\omega)$ of the overstable mode on the viscosity parameters l/r and v_s/v_ϕ . Fig. 4 shows $p_1(x)$ corresponding to the eigenfunction of the overstable mode for $\text{Pr} = 0.2$, $k_r r = 40$, $l/r = 0.01$ and $v_s/v_\phi = 0.01$.

5 Conclusions

Using the anelastic approximation of linearized hydrodynamic equations, we studied the development of axially symmetric small perturbations in thin Keplerian discs. Dispersion relation is derived as a solution of general Sturm–Liouville eigenvalue problem for pressure perturbations. An overstable mode is discovered for different values of the disc thickness and microscopic viscosity and thermal conductivity of the gas. The overstability appears when the Prandtl parameter exceeds a critical value $8/45$. The unstable mode has viscous-convective nature and can serve as a seed for turbulence in astrophysical discs even in the absence of magnetic fields.

Acknowledgments. We thank R.A. Sunyaev for useful discussions. The work is supported by the Russian Foundation for Basic Research grant 14-02-91345.

References

1. *N. Shakura, K. Postnov*, Mon. Not. Roy. Astron. Soc., **448**, 3707, 2015.
2. *N. Shakura, K. Postnov*, Mon. Not. Roy. Astron. Soc., **451**, 3995, 2015.
3. *S. Kato, J. Fukue, S. Mineshige*, Black-Hole Accretion Disks: Towards a New Paradigm. Kyoto: Kyoto University Press, 2008.
4. *K. Malanchev, N. Shakura, K. Postnov*, in preparation.
5. *N. A. Ketsaris, N. I. Shakura*, Astron. Astroph. Trans., **15**, 193, 1998.
6. *M. Abramowitz, I. A. Stegun*, Handbook of Mathematical Functions: with Formulas, Graphs, and Mathematical Tables. Washington: Nat. Bur. Stand., 1972.

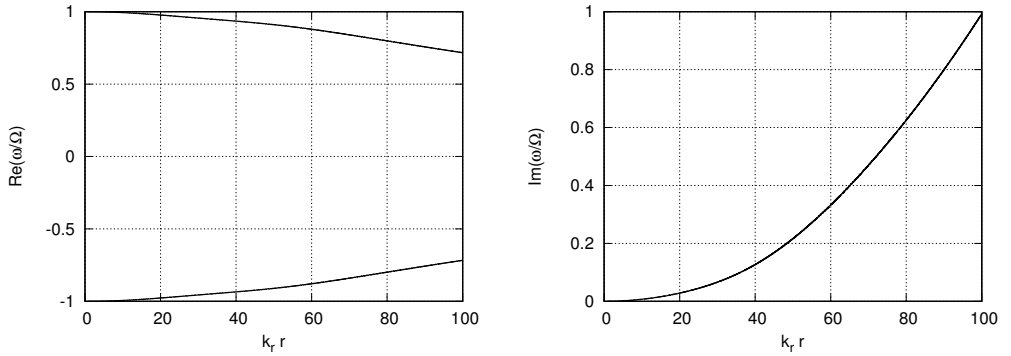


Figure 1: The dispersion equation for the critical Prandtl number $Pr = 8/45$, the mean-free path length of particles $l/r = 0.01$ and disc semi-thickness parameter $v_s/v_\phi = 0.01$. The left panel shows the real part of two decaying modes in terms of dimensionless frequency ω/Ω and the dimensionless wavenumber $k_r r$. The right panel shows the imaginary part of the dispersion relation which is the same for both decaying modes.

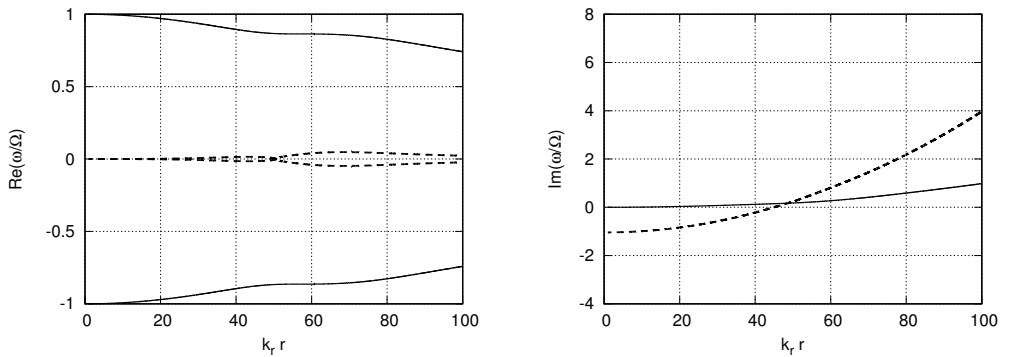


Figure 2: Dispersion relation for $Pr = 0.2$, $l/r = 0.01$ and $v_s/v_\phi = 0.01$. Left panel shows the real part of two decaying (the solid line) and two overstable modes (the dashed line) in terms of the dimensionless frequency ω/Ω and the dimensionless wavenumber $k_r r$. Right panels shows the imaginary part of these modes.

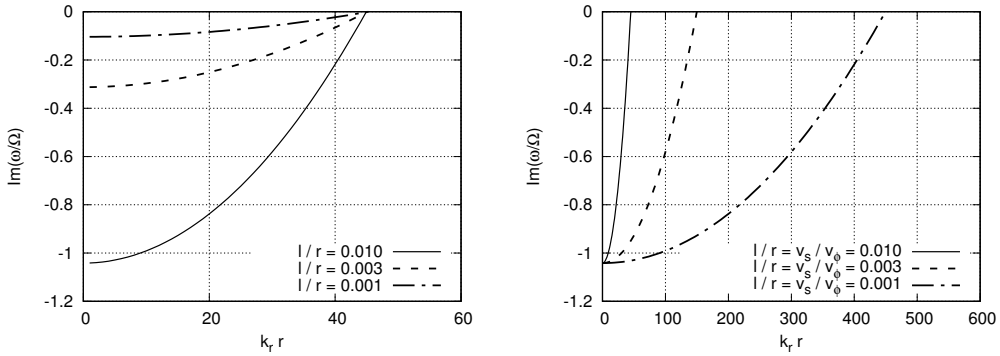


Figure 3: The imaginary part of the dispersion relations for $Pr = 0.2$ and different values of l/r and v_s/v_ϕ . In the left panel, the value of $v_s/v_\phi = 0.01$ is constant for all curves. The viscosity changes in proportion to l/r and $Im(\omega)$ changes in the same way. On the right panel both v_s/v_ϕ and l/r changes in the same way so that the term (25) keeps constant. Here the range of wavenumbers $k_r r$ of the overstable mode decreases inversely proportional to the disc thickness.

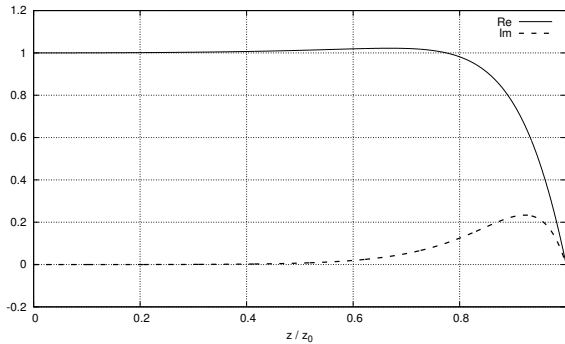


Figure 4: The overstable solution of the problem (12, 15, 16) for variable $x = z/z_0$ with the following parameters: $k_r r = 40$, $Pr = 0.2$, $l/r = 0.01$ and $v_s/v_\phi = 0.01$. Figure shows the normalized eigenfunction $p_1(x)$. The solid line shows the real part of $p_1(x)$, the dashed line shows the imaginary part of the pressure perturbation $p_1(x)$.

X-Ray Pulsars in a Wide Luminosity Range

A. Mushtukov^{1,2,3}, V. Suleimanov^{4,5}, S. Tsygankov³,
D. Nagirner⁶, A. Lutovinov^{7,8}, J. Poutanen^{3,9}

E-mail: *al.mushtukov@gmail.com*

A picture of X-ray pulsars (XRPs) behavior in a wide luminosity range is presented. The characteristic accretion luminosity values are discussed as well as connection between XRP and ultraluminous X-ray sources (ULXs).

1 X-ray pulsars

XRP stand out from the other classes of accreting NSs due to their strong magnetic field ($\gtrsim 10^{12}$ G), which affects both the geometry of the accretion flow in the vicinity of NS and elementary processes of interaction between radiation and matter.

Magnetic field interrupts the accretion disc (or stellar wind) at the magnetospheric radius, where the magnetic and plasma stresses balance. The magnetospheric radius is given by

$$R_m = k \left(\frac{\mu^4}{GM\dot{M}^2} \right)^{1/7},$$

where M and μ are the NS mass and magnetic moment, respectively, \dot{M} is the mass accretion rate and $k \leq 1$ is a constant which depends on the accretion flow geometry ($k = 1$ for the case of spherical accretion and $k < 1$ for the case of accretion from the disc, see [1]). Inside the magnetospheric radius, the magnetic field channels the gas towards the magnetic poles, where the captured matter releases its gravitational energy as X-ray radiation. Some questions concerns the interaction of the accretion flow (stellar wind or accretion disc) and NS magnetosphere [2]. They are important for a self-consistent picture, but beyond the scope of this text.

¹ Anton Pannekoek Institute, University of Amsterdam, The Netherlands

² Pulkovo Observatory of the Russian Academy of Sciences, St. Petersburg, Russia

³ Tuorla Observatory, Department of Physics and Astronomy, Univ. of Turku, Finland

⁴ Institut für Astronomie und Astrophysik, Universität Tübingen, Germany

⁵ Kazan (Volga region) Federal University, Russia

⁶ Sobolev Astronomical Institute, St. Petersburg State University, Russia

⁷ Space Research Institute of the Russian Academy of Sciences, Moscow, Russia

⁸ Moscow Institute of Physics and Technology, Russia

⁹ Nordita, KTH Royal Institute of Technology and Stockholm University, Sweden

High magnetic field modifies the elementary processes of interaction between radiation and matter including Compton scattering [3], which defines the radiation pressure and affects spectrum of emergent radiation. In the case of strong magnetic fields, the scattering has a number of special features. Its cross-section can be much smaller than the Thompson scattering cross-section σ_T depending on magnetic field strength, photon momentum and polarization state. At the same time electron transition between Landau levels causes the resonant scattering at some photon energies, where the cross-section can exceed σ_T by several orders of magnitude [4, 5]. The resonant scattering leads to appearance of absorption features in the spectra of XRPs – cyclotron lines – and affects the radiation pressure.

2 Below and above the critical luminosity

The accretion luminosity of XRPs is observed to be close or even higher than the Eddington limit L_{Edd} [6], which is commonly used as a restriction of possible isotropic luminosity of the object with a given mass M

$$L_{\text{Edd}} = \frac{4\pi GMm_{\text{H}}c}{\sigma_{\text{T}}(1+X)} \approx 1.4 \times 10^{38} \frac{M}{M_{\odot}} \text{ erg s}^{-1}, \quad (1)$$

where m_{H} is the hydrogen mass and X is its mass fraction.

The theory of accretion onto magnetized NS is based on two important effects: the accretion flow is channeled by strong magnetic field, which makes the problem essentially non-spherically symmetrical, and the effective cross-section σ_{eff} of the interaction between radiation and matter can be much different from the cross-section in the non-magnetic case.

At low mass accretion rates ($< 10^{16} \text{ g s}^{-1}$) radiation pressure has only a minor effect on the infalling material. The accretion flow heats up the NS surface and the observed spectrum is shaped by plasma deceleration in the NS atmosphere and by interaction of already emitted radiation with the accretion flow.

The higher the mass accretion rate, the higher the radiation pressure. If the radiation pressure is high enough, it affects the accretion flow velocity. The changes of the accretion flow velocity can be detected from variations of cyclotron line position in the spectrum: the line forms due to the resonant scattering in the accretion flow and, as a result, it is affected by Doppler shifting in the accretion channel [7].

At sufficiently high mass accretion rate the matter is fully stopped by the radiation pressure above stellar surface and an accretion column begins to grow. The corresponding luminosity, which is called critical luminosity, can be estimated as follows [8, 9]:

$$L^* = 4 \times 10^{36} \frac{M/M_{\odot}}{R/10^6 \text{ cm}} \left(\frac{l_0}{2 \times 10^5 \text{ cm}} \right) \frac{\sigma_{\text{T}}}{\sigma_{\text{eff}}} \text{ erg s}^{-1}, \quad (2)$$

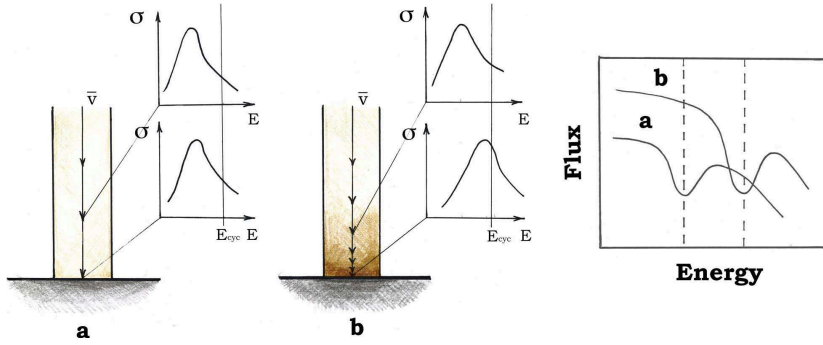


Figure 1: The schematic presentation of the dependence of the cyclotron line energy on the velocity profile in the line-forming region for the case of sub-critical XRPCs (see [7] for details).

where R is the NS radius, l_0 is the length of the accretion channel cross-section on the NS surface and σ_{eff} is the effective scattering cross-section in strong magnetic field. The value of L^* depends on the surface magnetic field strength due to the strong dependence of the scattering cross-section on the field strength. The critical luminosity is not a monotonic function of B and has its minimum value of $\sim(3 \div 5) \times 10^{36} \text{ erg s}^{-1}$ at B -field strength of $\sim 10^{12} \text{ G}$, when the peak in the source spectrum is close to E_{cycl} and the effective radiation pressure reaches its maximum value [9]. For higher magnetic field strength, the critical luminosity value increases due to decrease of the effective scattering cross-section (see Fig. 1).

At the accretion luminosity $L > L^*$ for a given magnetic field strength the accretion flow stops at the radiation dominated shock above the NS surface and slowly settles in inside a sinking region. The luminosity of highly magnetized NS featuring an accretion column above its surface can be much higher than the Eddington luminosity value, because the radiation pressure is balanced by the strong magnetic pressure (instead of gravity), which supports the column. The luminosity of the NS with an accretion column of height H above its surface can be roughly estimated as follows [10]:

$$L^{**}(H) \approx 38 \left(\frac{l_0/d_0}{50} \right) \frac{\sigma_{\text{T}}}{\sigma_{\perp}} f \left(\frac{H}{R} \right) L_{\text{Edd}}, \quad f(x) = \log(1+x) - \frac{x}{1+x}, \quad (3)$$

where d_0 is the thickness of the accretion channel, σ_{\perp} is the effective Compton scattering cross-section across the magnetic field direction. For a column as high as the NS radius, the accretion luminosity becomes $L^{**}(H = R) \approx (2 \div 3) \times 10^{39} \left(\frac{l_0/d_0}{50} \right) \frac{\sigma_{\text{T}}}{\sigma_{\perp}} \text{ erg s}^{-1}$.

From the comparison of XRPCs spectra variability with the theoretical models, we can conclude that the height of the accretion column increases with the mass accretion rate and, indeed, can be comparable to the NS radius [12].

The height of the accretion column is obviously limited by the magnetosphere's radius ($H < R_{\text{m}}$). However, many additional conditions have to be taken

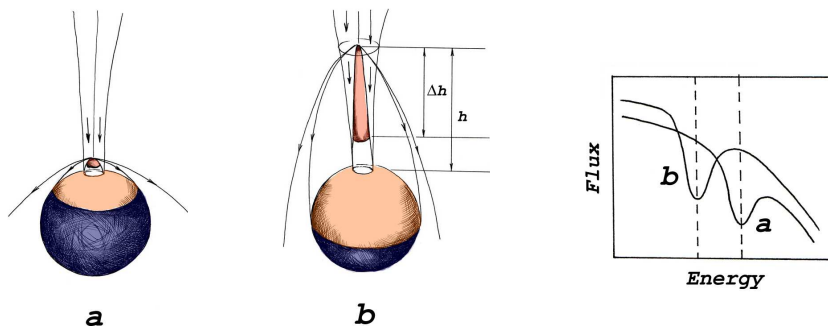


Figure 2: The schematic presentation of the dependence of the cyclotron line energy on the velocity profile in the line-forming region for the case of super-critical XRPs (see [12] for details).

into account. The gas and radiation pressure inside the column should not be higher than the magnetic pressure. This is important for fields of strength below $\sim 2 \times 10^{13}$ G. If the magnetic field strength is higher than $\sim 2 \times 10^{13}$ G, the internal column temperature can reach the value of $\sim 10^{10}$ K, when the electron-positron pair creation with further annihilation into neutrino and anti-neutrino becomes important: $e^+ + e^- \rightarrow \nu_e + \bar{\nu}_e$. In this case part of accretion luminosity can be released by neutrino rather than by photons. However, it was shown that the accretion columns above NS with surface B -field strength $\gtrsim 5 \times 10^{13}$ G cannot be significantly higher than NS radius and their internal temperature does not reach values of $\sim 10^{10}$ K [10].

The accretion column structure determines the beam pattern of XRPs [14]. The height of the accretion column, where the matter is stopped by the radiation dominated shock, is different inside the accretion channel. It is caused by the fact that the radiation energy density drops towards the accretion channel edges. As a result, the height reaches its maximum value in the center of the channel and it decreases towards the edges. Therefore, the radiation from the already stopped matter has to penetrate through the layer of fast moving plasma. It leads to the radiation beaming towards the NS surface, where the radiation is intercepted and reprocessed. Changes of the accretion column height and corresponding variability of the illuminated region on the NS surface explain naturally variations of the cyclotron line centroid energy [11] with the accretion luminosity: the higher the mass accretion rate, the higher the column, the lower the magnetic field strength averaged over the illuminated part of the NS, the lower the observed cyclotron line centroid energy [12, 13].

3 XRPs and ULXs

ULXs are point-like extragalactic X-ray sources with an observed X-ray luminosity in excess of $L \sim 10^{39}$ ergs $^{-1}$, assuming that they radiate isotropically. The bolometric luminosity of ULXs exceeds the Eddington limit for accretion on

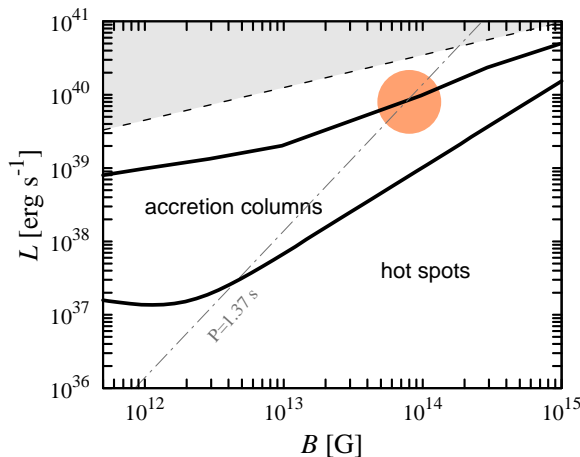


Figure 3: The critical L^* and maximum accretion luminosity values as functions of the B -field strength are given by thick solid lines. The grey region corresponds to the conditions when the accretion disc becomes super-critical. The lower limit on the X-ray luminosity for the case of NS spin period $P = 1.37$ s is shown by dashed-dotted line. It is related to the inhibition of accretion by the propeller effect. The position of the ULX X-2 in galaxy M82 is given by the orange circle.

a $10M_{\odot}$ black hole (BH). This is, indeed, intriguing since ULXs may be a possible manifestation of sub-critical accretion onto intermediate-mass (masses in the range $\sim 10^2 \div 10^5 M_{\odot}$) BHs.

At the present time their true nature is not well understood and in fact there may be several types of objects in this category. Most of the models are focused on accretion onto intermediate or stellar mass BHs.

However, it was found by the *NuSTAR* observatory that the ULX X-2 in galaxy M82 shows coherent pulsations with an average period of 1.37 s, which means that the compact object in this particular case is not a BH but a NS [15]. This discovery implies that accreting NS can reach luminosities of about 10^{40} erg s $^{-1}$ (see Fig. 3), which is two orders of magnitude higher than the Eddington limit. Such high mass accretion luminosity can be explained by extremely high NS magnetic field $\sim 10^{14}$ G, which reduces the scattering cross-section and confines the accretion flow to accretion column [10].

It is already confirmed that in this particular case we see accretion onto NS with magnetar-like magnetic field $\sim 10^{14}$ G [16]. According to simple estimations, an accreting NS at such high mass accretion rate reaches the spin equilibrium (when the corotation and magnetosphere radii are equal) within a few hundreds years. As a result, small changes in the mass accretion rate lead to dramatic changes of the accretion luminosity due to the so-called “propeller”-effect, which has been observed in a few XRPs [17]. The mass accretion rate, at which the “propeller”-effect appears, depends on the B -field strength, and the latter can be estimated from the known mass accretion rate. The “propeller”-effect has been observed in ULX M82 X-2 and magnetic field $\sim 10^{14}$ G has been confirmed [16].

The discovery of NSs as compact objects in ULXs puts an additional important question: what fraction of ULXs are accreting NSs? It is interesting that no other pulsating ULX has been observed yet. According to our recent results, the accretion luminosity of a few $\times 10^{40}$ erg s⁻¹ is a good estimation for maximum NS accretion luminosity [10]. This luminosity coincides with the cut-off observed in the HMXBs luminosity function (ULXs are taken into account there as HMXB) which otherwise does not show any features at lower luminosities [18]. Therefore one can conclude that a substantial fraction of ULXs are accreting NSs.

References

1. *J. Frank, A. King, D. Raine*, *Accretion Power in Astrophysics*. Cambridge: Cambridge Univ. Press, 2002.
2. *D. Lai*, *Phys. J. Web Conf.*, **64**, 1001, 2014.
3. *A.K. Harding, D. Lai*, *Rep. Prog. Phys.*, **69**, 2631, 2006.
4. *A.A. Mushtukov, D.I. Nagirner, J. Poutanen*, *Phys. Rev. D*, **85**, 103002, 2012.
5. *A.A. Mushtukov, D.I. Nagirner, J. Poutanen*, *Phys. Rev. D*, **93**, 105003, 2016.
6. *R. Walter, A.A. Lutovinov, E. Bozzo, S.S. Tsygankov*, *Astron. Astrophys. Rev.*, **23**, 2, 2015.
7. *A.A. Mushtukov, S.S. Tsygankov, A.V. Serber et al.*, *Mon. Not. Roy. Astron. Soc.*, **454**, 2714, 2015.
8. *M.M. Basko, R.A. Sunyaev*, *Mon. Not. Roy. Astron. Soc.*, **175**, 395, 1976.
9. *A.A. Mushtukov, V.F. Suleimanov, Sergey S. Tsygankov, J. Poutanen*, *Mon. Not. Roy. Astron. Soc.*, **447**, 1847, 2015.
10. *A.A. Mushtukov, V.F. Suleimanov, S.S. Tsygankov, J. Poutanen*, *Mon. Not. Roy. Astron. Soc.*, **454**, 2539, 2015.
11. *S.S. Tsygankov, A.A. Lutovinov, E.M. Churazov, R.A. Sunyaev*, *Mon. Not. Roy. Astron. Soc.*, **371**, 19, 2006.
12. *J. Poutanen, A.A. Mushtukov, V.F. Suleimanov et al.*, *Astrophys. J.*, **777**, 115, 2013.
13. *A.A. Mushtukov, J. Poutanen, V.F. Suleimanov et al.*, *Phys. J. Web Conf.*, **64**, 2005, 2014.
14. *A.A. Lutovinov, S.S. Tsygankov, V.F. Suleimanov et al.*, *Mon. Not. Roy. Astron. Soc.*, **448**, 2175, 2015.
15. *M. Bachetti, F.A. Harrison, D.J. Walton et al.*, *Nature*, **514**, 202, 2014.
16. *S.S. Tsygankov, A.A. Mushtukov, V.F. Suleimanov, J. Poutanen*, *Mon. Not. Roy. Astron. Soc.*, **457**, 1101, 2016.
17. *S.S. Tsygankov, A.A. Lutovinov, V. Doroshenko et al.*, *Astron. Astrophys.*, **593**, A16, 2016.
18. *S. Mineo, M. Gilfanov, R. Sunyaev*, *Mon. Not. Roy. Astron. Soc.*, **419**, 2095, 2012.

* The color figures are available online in the Proceedings at <http://www.astro.spbu.ru/sobolev100/>.

Strongly Magnetized Atmospheres and Radiating Surfaces of Neutron Stars

A.Y. Potekhin^{1,2,3}

E-mail: *palex@astro.ioffe.ru*

The theory of thermal emission from the surface layers of magnetized neutron stars is reviewed, including radiative transfer in partially ionized atmospheres with magnetic fields $B \sim 10^{10}$ – 10^{15} G and radiation from condensed surfaces at $B \gtrsim 10^{12}$ G. Applications of the theory to observations of thermally emitting isolated neutron stars with strong magnetic fields are summarized.

1 Introduction

A detailed study of the thermal spectra of neutron stars can yield precious information about properties of plasmas at extreme conditions in their atmospheres and interiors, about the neutron star masses M , radii R , temperatures T , and magnetic fields \mathbf{B} , and eventually help to constrain the equation of state (EOS) of the ultradense matter in the neutron star cores. In recent years, the number and quality of measured thermal spectra of neutron stars increased dramatically thanks to the data collected by the X-ray observatories *Chandra* and *XMM-Newton*. Some of the spectra can be understood with models of non-magnetic atmospheres (e.g., [1] and references therein). However, thermal spectra of many isolated neutron stars (INSs) are significantly affected by strong magnetic fields. The theory of these effects is reviewed in the present paper. Section 2 describes the theory of partially ionized neutron star atmospheres with strong magnetic fields, Sect. 3 considers the model of a condensed radiating surface and hybrid models of a condensed surface covered by a thin atmosphere, Sect. 4 describes synthetic energy and polarization spectra, and Sect. 5 presents examples of applications of the theory to observations.

2 Theory of strongly magnetized atmospheres

We call an atmosphere *strongly magnetized*, if a magnetic field strongly (non-perturbatively) affects opacities and radiative transfer of thermal photons. This occurs if the electron cyclotron energy $\hbar\omega_c \equiv \hbar eB/m_e c \approx 11.577 (B/10^{12} \text{ G}) \text{ keV}$ is greater than either the photon energies $\hbar\omega$ or the atomic binding energies, or both. Here, ω is the photon angular frequency, m_e and $-e$ are the electron

¹ Ioffe Institute, St. Petersburg, Russia

² Central Astronomical Observatory at Pulkovo, St. Petersburg, Russia

mass and charge, and c is the speed of light. These conditions imply (see [2] for discussion) $B \gtrsim 10^{10} T_6 \text{ G}$, where $T_6 \equiv T/10^6 \text{ K}$, and $B \gtrsim B_0$, where $B_0 = m_e^2 c e^3 / \hbar^3 \approx 2.35 \times 10^9 \text{ G}$ is the atomic unit of magnetic field. It is also convenient to define the relativistic magnetic-field parameter $b \equiv \hbar \omega_c / m_e c^2 = B / 4.414 \times 10^{13} \text{ G}$. We call magnetic field *superstrong* if $b \gtrsim 1$. The superstrong fields are believed to exist at the surfaces of magnetars and high- B pulsars [3, 4].

At typical conditions in neutron star photospheres one can describe radiative transfer in terms of specific intensities of two normal polarization modes [5, 6], called extraordinary (X-mode) and ordinary (O-mode), which have different polarization vectors e_j , depending on ω and on the angle θ_{kB} between the wave vector \mathbf{k} and the magnetic field \mathbf{B} . The system of radiative transfer equations (RTE) for the two normal modes is presented in [7].

The polarization vectors of normal modes $e_{\omega,j}$ are determined by the complex polarizability tensor $\chi(\omega)$ and magnetic permeability tensor [5]. The anti-Hermitian part of $\chi(\omega)$ is determined by the absorption opacities, and the Hermitian part can be obtained from it using the Kramers–Kronig relation [8, 9].

In strong magnetic fields, the effects called polarization and magnetization of vacuum can be important (see, e.g., [10]). At $B \lesssim 10^{16} \text{ G}$, they linearly add to χ and can be parametrized by three numbers, called vacuum polarizability and magnetization coefficients, which were fitted by analytic functions of b in [9]. Convenient expressions of e_j through $\chi(\omega)$ with account of the vacuum polarization were presented in [11].

Opacities for the X-mode are strongly reduced, if $\omega_c \gg \omega$. The opacities also depend on θ_{kB} . Nevertheless, at large optical depth radiation is almost isotropic: the magnitude of the diffusive radiative flux is much smaller than the mean intensity. In this case an approximate solution to the RTE is provided by the diffusion approximation [7], which serves as a starting point to an iterative method [12], allowing one to solve the RTE system accurately. To this end, one must know the dependencies of the temperature and densities of particles on the depth. These dependencies can be found from the equations of thermal, hydrostatic, and ionization equilibrium supplemented with the EOS. The plasma composition, EOS, and opacities are affected by the field, as reviewed in [2].

As first noticed in [13], atoms and ions with bound states should be much more abundant at $B \gg B_0$ than at $B \lesssim B_0$ in a neutron star atmosphere at the same temperature. This difference is caused by the increase of atomic binding energies and decrease of atomic sizes at $B \gg B_0$. Therefore, bound-bound and bound-free transitions are important in strong magnetic fields even for light-element atmospheres, which would be almost fully ionized at $B = 0$.

Many authors studied atoms with an infinitely heavy (fixed in space) nucleus in strong magnetic fields (see, e.g., [14], for review). This model, however, is only a crude approximation. If the ratio B/B_0 is not negligibly small compared to the nucleus-to-electron mass ratio, one should take into account quantum oscillations of an atomic nucleus, which depend on the quantum state. Moreover, the astrophysical simulations assume finite temperatures, hence thermal motion

of particles. The theory of motion of a system of point charges q_i at points \mathbf{r}_i in a constant magnetic field was reviewed in [15]. Instead of the canonical momentum \mathbf{P} , a relevant conserved quantity is pseudomomentum $\mathbf{K} = \mathbf{P} + (1/2c) \mathbf{B} \times \sum_i q_i \mathbf{r}_i$. The specific effects related to collective motion of a system of charged particles are especially important in neutron star atmospheres at $B \gg B_0$. In particular, so called *decentered states* may become populated, where an electron is localized mostly in a “magnetic well” aside from the Coulomb center. Binding energies and wave functions of the hydrogen atom moving across a strong magnetic field were calculated in [16, 17]. Bound-bound, bound-free, and free-free radiative transitions were studied in [17–21]. The absorption cross-sections have peaks at the multiples of both the electron and ion cyclotron frequencies for all polarizations α , but unlike the electron cyclotron harmonics, the ion harmonics, except the fundamental, are weak and can be neglected. The dependencies of energies and oscillator strengths on the transverse pseudomomentum $\mathbf{K}_\perp = \mathbf{K} - (\mathbf{B} \cdot \mathbf{K})\mathbf{B}/B^2$ cause a “magnetic broadening” of the spectral lines and ionization thresholds, which can be much larger than the usual Doppler and plasma broadenings.

The He^+ ion moving across a strong magnetic field was studied in [22, 23]. The basic differences from the case of a neutral atom are that the Cartesian components of the operator \mathbf{K}_\perp do not commute and the values of K^2 are quantized [15]. Currently there is no detailed calculation of binding energies, oscillator strengths, and photoionization cross-sections for atoms and ions other than H and He^+ , arbitrarily moving in a strong magnetic field. A practical method of calculation of the quantum-mechanical characteristics of multielectron atoms and ions, based on a combination of several perturbation theories with respect to different physical parameters, has been developed in [24].

Since the quantum-mechanical characteristics of an atom in a strong magnetic field depend on K_\perp , the atomic distribution over K_\perp cannot be written in a closed form, and only the distribution over longitudinal momenta K_z remains Maxwellian. The first EOS calculations with account of these effects have been performed in [25] for hydrogen and in [26] for helium plasmas. To date, self-consistent calculations of the EOS and opacities, including both centered and decentered bound states (i.e., small and large K_\perp), have been realized only for neutron-star atmospheres composed of hydrogen [20, 27, 28]. For atoms and ions with several bound electrons (C, O, Ne), calculations have been performed in terms of a perturbation theory [29, 30].

3 Condensed surfaces and thin atmospheres

Ruderman [31] suggested that a strong magnetic field may cause a condensation of matter. Properties of the resulting condensed magnetic surfaces were studied in a number of papers (see [32] and references therein). Thermal radiation of the surface is determined by its emissivities in two normal modes, which are related to the reflectivities through the Kirchhoff law. They were calculated and fitted in [33] (see references therein for older approaches). Moreover, Motch et al. [34]

suggested that some neutron stars can possess a hydrogen atmosphere of a finite thickness above the solid iron surface. If the optical depth of such atmosphere is small for some wavelengths and large for others, the thermal spectrum differs from that of thick atmospheres. Such spectra were calculated in [35–37] using simplified boundary conditions for the radiative transfer equation at the bottom of the atmosphere. More accurate boundary conditions [33] take into account that any polarized wave, falling from the atmosphere on the surface, gives rise to reflected waves of both normal polarizations, whose intensities add to the respective intensities of the waves emitted by the condensed surface.

Local spectra of radiation emitted by thin hydrogen atmospheres over a condensed surface may reveal a narrow absorption line corresponding to the proton cyclotron resonance in the atmosphere, features related to atomic transitions broadened by the motion effects, and a kink corresponding to the ion cyclotron energy of the substrate ions. Some of these features may be absent, depending on the atmosphere thickness and magnetic field strength. At high energies, the spectrum is determined by the condensed-surface emission, which is softer than the spectrum of the thick hydrogen atmosphere.

One may also envisage an atmosphere having a helium layer beneath the hydrogen layer. The spectrum of such “sandwich atmosphere” can have two or three absorption lines in the range $E \sim (0.2\text{--}1)\text{ keV}$ at $B \sim 10^{14}\text{ G}$ [36].

4 Synthetic energy and polarization spectra

The strong gravity of a neutron star induces a significant redshift of the local photon frequency ω to $\omega_\infty = \omega/(1 + z_g)$ in the remote observer’s reference frame, where $z_g = (1 - 2GM/c^2R)^{-1/2} - 1$ is the gravitational redshift, and G the gravitational constant. Accordingly, a thermal spectrum with effective temperature T_{eff} transforms for the remote observer into a spectrum with a lower “observed” temperature $T_{\text{eff}}^\infty = T_{\text{eff}}/(1 + z_g)$. Along with the radius R that is determined by the equatorial length $2\pi R$ in the local reference frame, one often considers an *apparent radius* for a remote observer, $R_\infty = R(1 + z_g)$, so that the apparent photon luminosity L_{ph}^∞ is determined by the Stefan–Boltzmann law $L_{\text{ph}}^\infty = L_{\text{ph}}/(1 + z_g)^2 = 4\pi\sigma_{\text{SB}} R_\infty^2 (T_{\text{eff}}^\infty)^4$, where σ_{SB} is the Stefan–Boltzmann constant, and $L_{\text{ph}} = 4\pi\sigma_{\text{SB}} R^2 T_{\text{eff}}^4$ is the luminosity in the local reference frame.

The spectral flux that comes to an observer is distorted by the light bending in strong gravity. It can be calculated using equations presented in [38] provided that the emitted specific intensity distribution is known for the entire visible surface of the neutron star. The problem is complicated by nontrivial surface distributions of the magnetic field and effective temperature. A fiducial model for the magnetic field distribution is the relativistic dipole [39], but recent numerical simulations of the magnetothermal evolution produce more complicated distributions (see [40, 41] and references therein). The temperature distribution, consistent with the magnetic-field distribution, is found from calculations of heat transport in neutron star envelopes (see [42] for review).

Synthetic spectra of partially ionized hydrogen atmospheres were calculated in [43], including averaging over the stellar surface with realistic temperature and magnetic field distributions. The spectra depend on the magnetic axis orientation relative to the line of sight. As the star rotates, the latter dependence leads to a rotational phase dependence of the spectra. Model spectra of partially ionized, strongly magnetized neutron star atmospheres composed of hydrogen, carbon, oxygen, and neon with magnetic fields $B \sim 10^{10}$ – 10^{13} G are included in the open database *XSPEC* [44] under the names NSMAX [30, 43] and NSMAXG [30, 45, 46], with the latter allowing for varying surface gravity.

Thermal radiation emergent from neutron stars with strong magnetic fields is expected to be strongly polarized. Since the opacity is smaller for the X-mode, this mode escapes from deeper and hotter layers in the atmosphere, therefore the X-mode polarization prevails in the thermal radiation [47]. Polarization of the observed radiation depends on the distribution of magnetic field and temperature over the visible neutron star surface. As the star rotates, the polarization pattern shows periodic variations, so that measuring the polarization pulse profile allows one to constrain the orientation of the rotation axis and the field strength and geometry [48, 49]. Therefore, future X-ray polarization measurements are expected to resolve degeneracies that currently hamper the determination of magnetar physical parameters using thermal models [50, 51].

After a photon has left the surface of a neutron star with a strong magnetic field, it travels through the magnetosphere and experiences the influence of vacuum polarization, which induces a change in the wave electric field as photon propagates. If the magnetic field is sufficiently strong, then in the vicinity of the star a photon propagates adiabatically, so that its polarization instantaneously adapts to the variation of the magnetic field direction [52, 53]. Farther from the star the field decreases, and eventually photons leave the adiabatic region and maintain their polarization. The rays that leave the adiabatic region pass through only a small solid angle; consequently, polarizations of the rays originating in different regions will tend to align together. This effect can enhance the net observed polarization [54]. A comparison of polarizations assuming either gaseous atmospheres or condensed surfaces was analyzed in [55].

5 Theory versus observations

As argued above, models of strongly magnetized ($B \gg 10^9$ G) neutron-star atmospheres must take the bound species and their radiative transitions into account. Currently there are the following examples of application of models of *strongly magnetized and partially ionized* atmospheres to studies of thermal radiation of neutron stars with strong magnetic fields:

- RX J1856.5–3754, which is the closest and brightest of the class of X-ray INSs (XINSs, also known as the Magnificent Seven), whose X-ray spectra are apparently of purely thermal nature. Its measured spectrum was fitted in the entire range from X-rays to optical within observational error bars

- with the use of the model of a thin magnetized hydrogen atmosphere on top of a condensed iron surface [35] (see also a discussion in [46]).
- phase-resolved spectrum and light curve of XINS RX J1308.6+2127 (RBS1223) have been described in [56] by the model with a magnetized iron surface covered by a partially ionized hydrogen atmosphere;
 - the X-ray spectrum of thermally emitting INS 1E 1207.4–5209 appears to have been explained by cyclotron absorption harmonics, corresponding to $B \approx 7 \times 10^{10}$ G [28, 57];
 - the *XMM-Newton* spectrum of thermally emitting INS 2XMM J104608.7–594306 has been analyzed in [58] with the blackbody model and hydrogen atmosphere model NSMAXG;
 - the spectrum of INS 1WGA J1952.2+2925 is equally well fitted either by the blackbody model with a temperature of $T \approx 2.5 \times 10^6$ K and an emitting area radius of ≈ 0.6 km or by the magnetized atmosphere model NSMAX with $T_{\text{eff}} \sim 10^6$ K and emission from the entire neutron-star surface [59];
 - rotation powered pulsars PSR J1119–6127, B0943+10, J0357+3205, and J0633+0632, whose thermal parts of spectra were analyzed in [60–63] using magnetized atmosphere model NSMAX.

A more detailed discussion of the interpretations of observations of the above-listed objects is given in [46].

References

1. V.F. Suleimanov, J. Poutanen, D. Klochkov, K. Werner, *Eur. Phys. J. A*, **52**, 20, 2016.
2. A. Y. Potekhin, *Phys. Usp.*, **57**, 735, 2014.
3. S. Mereghetti, J.A. Pons, A. Melatos, *Space Sci. Rev.*, **191**, 315, 2015.
4. R. Turolla, S. Zane, A.L. Watts, *Rep. Prog. Phys.*, **78**, 116901, 2015.
5. V.L. Ginzburg, *The Propagation of Electromagnetic Waves in Plasmas* (2nd ed.). London: Pergamon, 1970.
6. Yu.N. Gnedin, G.G. Pavlov, *Sov. Phys. JETP*, **38**, 903, 1974.
7. A.D. Kaminker, G.G. Pavlov, Yu.A. Shibano, *Astrophys. Space Sci.*, **86**, 249, 1982.
8. T. Bulik, G.G. Pavlov, *Astrophys. J.*, **469**, 373, 1996.
9. A. Y. Potekhin, D. Lai, G. Chabrier, W.C.G. Ho, *Astrophys. J.*, **612**, 1034, 2004.
10. G.G. Pavlov, Yu.N. Gnedin, *Sov. Sci. Rev. E: Astrophys. Space Phys.*, **3**, 197, 1984.
11. W.C.G. Ho, D. Lai, *Mon. Not. Roy. Astron. Soc.*, **338**, 233, 2003.
12. Yu.A. Shibano, V.E. Zavlin, *Astron. Lett.*, **21**, 3, 1995.
13. R. Cohen, J. Lodenquai, M. Ruderman, *Phys. Rev. Lett.*, **25**, 467, 1970.
14. H. Ruder, G. Wunner, H. Herold, F. Geyer, *Atoms in Strong Magnetic Fields*. Berlin: Springer, 1994.

15. *B.R. Johnson, J.O. Hirschfelder, K.H. Yang*, Rev. Mod. Phys., **55**, 109, 1983.
16. *M. Vincke, M. Le Dourneuf, D. Baye*, J. Phys. B: Atom. Mol. Phys., **25**, 2787, 1992.
17. *A.Y. Potekhin*, J. Phys. B: Atom. Mol. Opt. Phys., **27**, 1073, 1994.
18. *G.G. Pavlov, A.Y. Potekhin*, Astrophys. J., **450**, 883, 1995.
19. *A.Y. Potekhin, G.G. Pavlov*, Astrophys. J., **483**, 414, 1997.
20. *A.Y. Potekhin, G. Chabrier*, Astrophys. J., **585**, 955, 2003.
21. *A.Y. Potekhin*, Astron. Astrophys., **518**, A24, 2010.
22. *V.G. Bezchastnov, G.G. Pavlov, J. Ventura*, Phys. Rev. A, **58**, 180, 1998.
23. *G.G. Pavlov, V.G. Bezchastnov*, Astrophys. J. Lett., **635**, L61, 2005.
24. *K. Mori, C.J. Hailey*, Astrophys. J., **564**, 914, 2002.
25. *A.Y. Potekhin, G. Chabrier, Yu.A. Shibano*, Phys. Rev. E, **60**, 2193, 1999.
26. *K. Mori, J. Heyl*, Mon. Not. Roy. Astron. Soc., **376**, 895, 2007.
27. *A.Y. Potekhin, G. Chabrier*, Astrophys. J., **600**, 317, 2004.
28. *A.Y. Potekhin, G. Chabrier, W.C.G. Ho*, Astron. Astrophys., **572**, A69, 2014.
29. *K. Mori, C.J. Hailey*, Astrophys. J., **648**, 1139, 2006.
30. *K. Mori, W.C.G. Ho*, Mon. Not. Roy. Astron. Soc., **377**, 905, 2007.
31. *M.A. Ruderman*, Phys. Rev. Lett., **27**, 1306, 1971.
32. *Z. Medin, D. Lai*, Mon. Not. Roy. Astron. Soc., **382**, 1833, 2007.
33. *A.Y. Potekhin, V.F. Suleimanov, M. van Adelsberg et al.*, Astron. Astrophys., **546**, A121, 2012.
34. *C. Motch, V.E. Zavlin, F. Haberl*, Astron. Astrophys., **408**, 323, 2003.
35. *W.C.G. Ho, D.L. Kaplan, P. Chang et al.*, Mon. Not. Roy. Astron. Soc., **375**, 821, 2007.
36. *V. Suleimanov, A. Potekhin, K. Werner*, Astron. Astrophys., **500**, 891, 2009.
37. *V. Suleimanov, V. Hambaryan, A.Y. Potekhin et al.*, Astron. Astrophys., **522**, A111, 2010.
38. *J. Poutanen, A.M. Beloborodov*, Mon. Not. Roy. Astron. Soc., **373**, 836, 2006.
39. *V.L. Ginzburg, L.M. Ozernoi*, Sov. Phys. JETP, **20**, 689, 1965.
40. *D. Viganò, N. Rea, J.A. Pons et al.*, Mon. Not. Roy. Astron. Soc., **434**, 123, 2013.
41. *J.G. Elfritz, J.A. Pons, K. Glampedakis, D. Viganò*, Mon. Not. Roy. Astron. Soc., **456**, 4461, 2016.
42. *A.Y. Potekhin, J.A. Pons, D. Page*, Space Sci. Rev., **191**, 239, 2015.
43. *W.C.G. Ho, A.Y. Potekhin, G. Chabrier*, Astrophys. J. Suppl., **178**, 102, 2008.
44. *K.A. Arnaud*, in Astronomical Data Analysis Software and Systems V. Eds. G. Jacoby, J. Barnes. Astron. Soc. Pacif. Conf. Ser., **101**, 17, 1996.
45. *W.C.G. Ho*, in Magnetic Fields Throughout Stellar Evolution Proc. IAU Symp.

- No. 302. Eds. M. Jardine, P. Petit, H.C. Spruit. Cambridge: Cambridge University Press, 2014, p. 435.
46. *A.Y. Potekhin, W.C.G. Ho, G. Chabrier*, in *The Modern Physics of Compact Stars 2015*. Ed. A. Sedrakian. Proc. Sci., PoS(MPCS2015)016, 2016.
 47. *G.G. Pavlov, Yu.A. Shibarov*, *Sov. Astron.*, **22**, 43, 1978.
 48. *G.G. Pavlov, V.E. Zavlin*, *Astrophys. J.*, **529**, 1011, 2000.
 49. *D. Lai, W.C.G. Ho*, *Phys. Rev. Lett.*, **91**, 071101, 2003.
 50. *M. van Adelsberg, R. Perna*, *Mon. Not. Roy. Astron. Soc.*, **399**, 1523, 2009.
 51. *R. Taverna, F. Muleri, R. Turolla et al.*, *Mon. Not. Roy. Astron. Soc.*, **438**, 1686, 2014.
 52. *J.S. Heyl, N. Shaviv*, *Mon. Not. Roy. Astron. Soc.*, **311**, 555, 2000.
 53. *J.S. Heyl, N. Shaviv*, *Phys. Rev. D*, **66**, 023002, 2002.
 54. *J.S. Heyl, N. Shaviv, D. Lloyd*, *Mon. Not. Roy. Astron. Soc.*, **342**, 134, 2003.
 55. *R. Taverna, R. Turolla, D.G. Caniulef et al.*, *Mon. Not. Roy. Astron. Soc.*, **454**, 3254, 2015.
 56. *V. Hambaryan, V. Suleimanov, A.D. Schwope et al.*, *Astron. Astrophys.*, **534**, A74, 2011.
 57. *V.F. Suleimanov, G.G. Pavlov, K. Werner*, *Astrophys. J.*, **751**, 15, 2012.
 58. *A.M. Pires, C. Motch, R. Turolla et al.*, *Astron. Astrophys.*, **583**, A117, 2015.
 59. *A. Karpova, D. Zyuzin, A. Danilenko, Yu. Shibarov*, *Mon. Not. Roy. Astron. Soc.*, **453**, 2241, 2015.
 60. *C.-Y. Ng, V.M. Kaspi, W.C.G. Ho et al.*, *Astrophys. J.*, **761**, 65, 2012.
 61. *N.I. Storch, W.C.G. Ho, D. Lai et al.*, *Astrophys. J. Lett.*, **789**, L27, 2014.
 62. *A. Kirichenko, A. Danilenko, Yu. Shibarov et al.*, *Astron. Astrophys.*, **564**, A81, 2014.
 63. *A. Danilenko, P. Shternin, A. Karpova, D. Zyuzin*, *Publ. Astron. Soc. Austral.*, **32**, e038, 2015.

Behavior of Perturbations in an Accretion Flow on to a Black Hole

A.V. Semyannikov¹

E-mail: *avsemyannikov@gmail.com*

We investigate the behavior of small acoustic perturbations in the spherical adiabatic relativistic accretion flow on to a non-rotating black hole. The Das model of the accretion [1, 2] is a general relativistic generalization of the classical spherical Bondi accretion. We consider a general relativistic linear wave equation for small acoustic perturbations and fulfill the mode analysis of solutions. We find numerically that perturbations remain finite in amplitude on the event horizon due to the effects of the general relativity in contrast to predictions of the non-relativistic model based on the Bondi accretion approximation [3]. This circumstance downranges the possibilities for detection of black holes.

1 Motivation

It is known that converging flows are often subject to hydrodynamic instabilities. For example, small acoustic perturbations have to increase without limit in the spherical adiabatic accretion flow on to a non-rotating black hole [3]. The predictions of the referenced article are based on the non-relativistic Bondi model of the adiabatic spherical accretion on to a point gravitating mass. However, the more realistic model of accretion taking into account the relativistic nature of flow near the event horizon should take proper account of the finiteness of the accretor's radius (the Schwarzschild radius r_g) and the velocity limit (the light speed c). The aim of the present work is to find the influence of relativistic effects on the efficiency of amplification of small acoustic perturbations in the spherical accretion flow.

2 Model

We examine the spatial stability of spherical adiabatic flow of a non-self-gravitating non-viscous homogeneous matter on to a black hole from infinity. The model of accretion is described by the general relativistic hydrodynamic equations: equation of fluid motion

$$u^\nu \nabla_{;\nu} u^\mu = -\frac{1}{n} \left(g^{\mu\nu} + \frac{u^\mu u^\nu}{c^2} \right) \nabla_{;\nu} p, \quad (1)$$

¹ Volgograd State University, Russian Federation

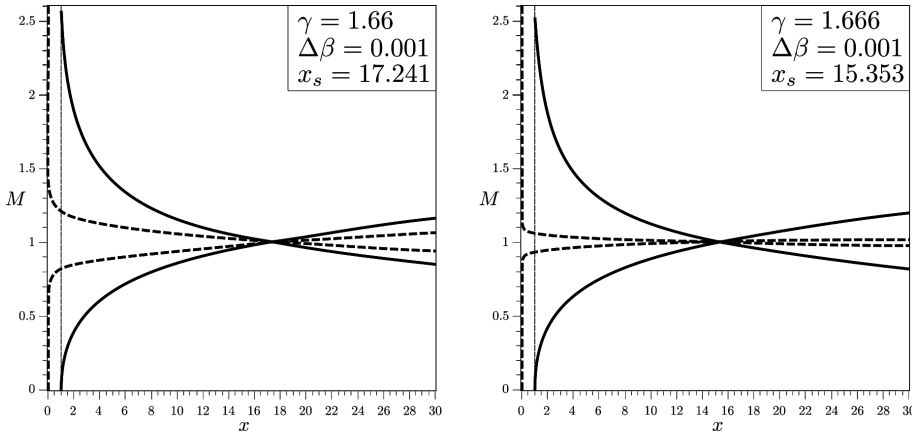


Figure 1: The Mach number M as the function of the dimensionless radial coordinate x (red lines). The subsonic (lower curve) and the supersonic (upper curve) separatrices of a relativistic solution (solid line) and a classic solution (dashed line).

and continuity equation

$$\nabla_{;\mu}(nu^\mu) = 0. \tag{2}$$

Here c is a speed of light, $g^{\mu\nu}$ a contravector of metric tensor, u^μ a geometrical contravector 4-velocity

$$u^\mu = \frac{dx^\mu}{d\tau}, \tag{3}$$

n is a specific relativistic density, and the pressure

$$p = Kn^\gamma. \tag{4}$$

A specific enthalpy is

$$h = mc^2 + \frac{\gamma}{\gamma - 1}Kn^{\gamma-1}. \tag{5}$$

The equation of state (4) allows us to formulate an equation for the speed of sound c_s

$$c_s^2 = c^2 \frac{K\gamma n^{\gamma-1}}{mc^2 + K\frac{\gamma}{\gamma-1}n^{\gamma-1}}. \tag{6}$$

Here K is the gaseous constant, m the rest mass of matter, γ the adiabatic constant. In the case of the steady state spherically symmetric flow the system (1)–(2), (6) is reduced to the algebraic system of two integrals of motion, the mass flux conservation [1, 2]

$$yzx^2 \sqrt{\frac{1 - \frac{1}{x}}{1 - y^2}} = \lambda, \tag{7}$$

and the Bernoulli integral

$$(1 + z^{\gamma-1}) \sqrt{\frac{1 - \frac{1}{x}}{1 - y^2}} = \beta, \tag{8}$$

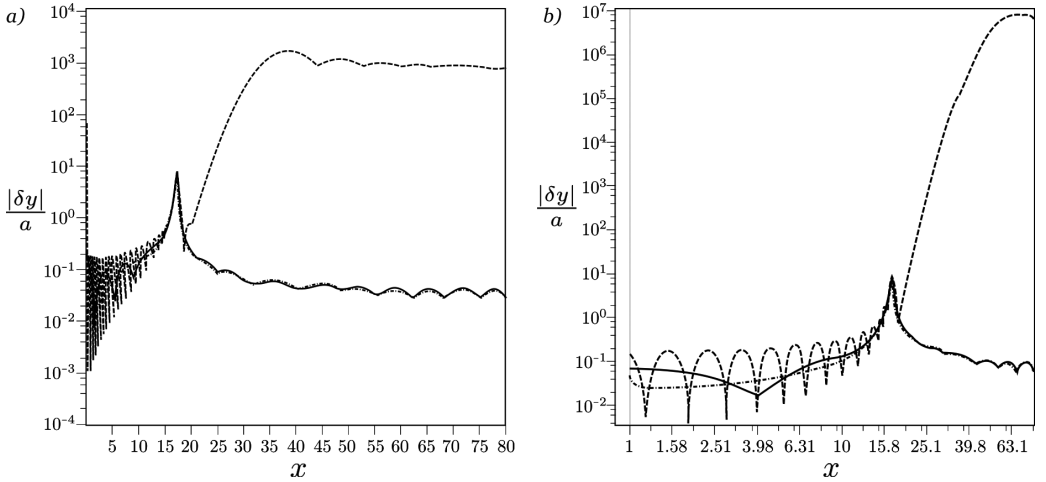


Figure 2: The ratio of the acoustic perturbations of radial velocity $|\delta y|$ for different azimuthal numbers l of spherical harmonics in the non-relativistic (a) and relativistic (b) cases. Dashed line with points is for $l = 0$, solid line for $l = 1$, and dashed line for $l = 10$. The frequency for all calculations $\omega = 0.01$, the adiabatic constant $\gamma = 1.66$, the energy $\Delta\beta = 0.001$.

and the equation for the non-dimensionalized sound speed a

$$a^2 = \frac{(\gamma - 1)z^{\gamma-1}}{1 + z^{\gamma-1}}. \quad (9)$$

Here λ and β are the mass flux and the Bernoulli constant, respectively. The non-dimensionalized flow variables are defined as follows:

$$x = \frac{r}{r_g}, \quad y = \frac{V_r}{c}, \quad z = \left(\frac{K\gamma}{mc^2(\gamma - 1)} \right)^{-\frac{1}{\gamma-1}} n, \quad a = \frac{c_s}{c}. \quad (10)$$

3 Solution

The perturbations are sought in the form

$$n = \delta n + n, \quad u^\mu = \delta u^\mu + u^\mu. \quad (11)$$

Potential of a 4-velocity is

$$u^\mu h = \nabla^{;\mu} \phi. \quad (12)$$

We find a solution in the form

$$\delta\phi = \delta\tilde{\phi}(x)Y_{lm}(\theta, \varphi)e^{-i\omega t}. \quad (13)$$

Cauchy-Lagrange integral is

$$\delta n = -\frac{u_{\sigma,0}}{K\gamma c^2 n_0^{\gamma-2}} \nabla^{;\sigma} \delta\phi. \quad (14)$$

Wave equation

$$\nabla_{;\mu}(d^{\mu\nu}\nabla_{,\nu}\delta\phi) = 0, \quad (15)$$

where d_{ν}^{μ} is a strange tensor

$$d_{\nu}^{\mu} = \frac{1}{K\gamma n_0^{\gamma-2}} \left(\frac{c_s^2}{c^2} g_{\nu}^{\mu} - \left(1 - \frac{c_s^2}{c^2}\right) \frac{u_0^{\mu} u_{\nu,0}}{c^2} \right). \quad (16)$$

A general relativistic wave equation

$$\begin{aligned} \delta\tilde{\phi}'' d^{rr} + \delta\tilde{\phi}' \left(\frac{1}{\sqrt{-g}} \frac{\partial}{\partial x} (\sqrt{-g} d^{rr}) - 2i\omega d^{rt} \right) + \\ - \delta\tilde{\phi} \left(-\frac{\omega^2}{c^2} d^{tt} - i\frac{\omega}{c} \frac{1}{\sqrt{-g}} \frac{\partial}{\partial x} (\sqrt{-g} d^{tr}) - d^{\theta\theta} l(l+1) \right) = 0. \end{aligned} \quad (17)$$

A classical limit of reduced wave equation

$$\begin{aligned} \delta\tilde{\phi}'' (a^2 - y^2) + \delta\tilde{\phi}' \left(2i\omega y - (y^2 + a^2) \frac{y'}{y} + 2y^2 \frac{a'}{a} \right) + \\ + \delta\tilde{\phi} \left(\omega^2 - 2i\omega y \frac{a'}{a} - a^2 \frac{l(l+1)}{x^2} \right) = 0. \end{aligned} \quad (18)$$

4 Results

We find that the acoustic perturbations are amplified significantly (many order of magnitudes) inside the sonic sphere in a spherical accretion flow, though remain finite compared to the case of the non-relativistic Bondi model.

References

1. *T.K. Das*, *Astrophys. J.*, **577**, 880, 2002.
2. *T.K. Das*, *Class. Quant. Grav.*, **21**, 5253, 2004.
3. *I.G. Kovalenko, M.A. Eremin*, *Mon. Not. Roy. Astron. Soc.*, **298**, 861, 1998.

RM Synthesis: Problems and Perspectives

D.D. Sokoloff^{1,2}

E-mail: *sokoloff.dd@gmail.com*

Main bulk of our knowledge concerning magnetic fields of spiral galaxies comes from observations of radio emission of the galaxies and in particular from Faraday rotation measures. We consider here traditional methods of this procedure in context of the new method known as RM Synthesis. RM Synthesis looks as an important tool for investigation of magnetic fields of spiral galaxies. Long wavelength observations allows a limited application of the method while expected facilities of SKA should allow such application in the full extent. Of course, it is desirable to combine RM Synthesis with options based on solution of inverse problem for multiwavelength observations.

1 Introduction

Magnetic field of the Milky Way is known for more than 60 years, and magnetic field of external spiral galaxies has been investigated since the 1980s. The main bulk of contemporary knowledge in this field comes from observations of polarized synchrotron emission in radio range. Polarization gives a hint that spiral galaxies contain magnetic fields of the scale comparable with galactic radius, while Faraday rotation of polarization plane confirms presence of this field and gives an estimate for it strength. The large-scale magnetic field component is almost parallel to the central galactic plane, and its direction is close to the azimuthal direction. The magnetic field strength is about several μG , i.e. magnetic field energy is close to equipartition with turbulent flows in the interstellar medium (see for a review, e.g., [1]).

Observations supporting the above understanding of galactic magnetism were obtained mainly at Effelsberg and VLA at 4 wavelengths (about 3, 6, 18, and 22 cm. A new generation of radio telescopes, which includes LOFAR and forthcoming SKA, opens a new perspective to obtain instructive information concerning galactic magnetic fields. The main novelty here is that it becomes possible to observe polarized radio emission at many (hundreds and possibly thousands) wavelengths instead of few ones only. Importance of this novelty is obvious for experts (see below), the question is, however, how to use this new ability. The aim of this paper is to discuss available suggestions in this respect.

¹ Department of Physics, Moscow State University, Russia

² IZMIRAN, Troitsk, Russia

2 Rotation measures and polarization angles

Starting points to use polarization data to get information concerning large-scale galactic magnetic fields are as follows. Synchrotron emission is polarized and its polarization angle is determined by magnetic field direction. If magnetic field is a small-scale random field, the emission becomes to be depolarized because of cancellation of many incomes with various polarization angles which contribute in one beam. In fact, the observed degree of polarization p (about 10–20%) is much lower than the initial one p_0 (about 70%) that gives a hint that a small-scale magnetic field b is superimposed on the large-scale one B , which leads to substantial depolarization. A simple estimate [2]

$$p = p_0 / (1 + b^2 / B^2) \quad (1)$$

tells that b is about two times larger than B . This estimate is supported by other available information (see for details [1]), however the point is that from one hand depolarization by small-scale magnetic field is far to be the only source of depolarization (see [2, 3]), and from the other hand anisotropic small-scale magnetic field can give polarization without large-scale one (so-called Laing effect – see, e.g., [3]).

Faraday rotation of polarization plane gives more direct information concerning large-scale magnetic field than just polarization. If polarized emission propagates through a slab with the line of sight magnetic field component $\mathbf{B}_{||}$, electron density n_e and thickness L , then its polarization angle ψ scales with λ as

$$\psi = \psi_0 + 0.81 \text{ [rad m}^{-2}\text{cm}^3\mu\text{G}^{-1}\text{pc}^{-1}] } B_{||} n_e L \lambda^2, \quad (2)$$

where the coefficient at λ^2 is known as rotation measure (RM).

An important point is that from the observational point of view ψ varies in the range $-\pi/2 \leq \psi \leq \pi/2$, while Eq. (2) does not take into account this constraint. This is known as $\pm k\pi$ problem. A natural resolution of the problem is to use such range of wavelengths, where $\text{RM}\lambda^2 \leq \pi$ (Faraday thin source [4]) and include λ short enough to makes $\text{RM}\lambda^2$ comparable with observational uncertainties. The range 3–22 cm fits more or less the requirements.

Basing on RM obtained observationally and known electron density, one obtains the line of sight magnetic field component only. Reconstruction of magnetic configuration in galactic disc as a whole requires fitting of a magnetic configuration model based on theoretical expectation from galactic dynamo to RM [5] or position angles [6] distribution in projection of galactic disc on the sky plane. This fitting is a highly non trivial task because the theoretical expectations are far to be very firm. Correspondingly, quite a lot of time and efforts are required to obtain a self-consistent model of galactic magnetic field from polarized observations.

3 Multiwavelength observations

The traditional procedure of magnetic configuration reconstruction from observational data has several substantial constraints. First of all, it does not take into account in an explicit form degree of polarization p and polarized intensity. A possible way to include such data in consideration is to fit a model to observed Stokes parameters $Q(\lambda^2)$ and $U(\lambda^2)$ [7].

A much more substantial point is that Eq. (2) implies that emission and Faraday rotation occur in separate regions at the line of sight so the case of so-called Faraday screen is considered. It happens, e.g., for Faraday rotation of radiation of extragalactic radio sources propagating through a nearby galaxy, say M 31, what can be used for reconstruction of magnetic field in such a galaxy [8]. A much more usual situation is, however, the case of radiation emitted and rotated in the same region in the galaxy in investigation. If such source is Faraday thick, polarization angle may deviate from the simple scaling Eq. (2) [3]. An important additional point is that LOFAR is constructed to observe at wavelengths of about 1 m and longer, so almost all spiral galaxies are expected to be Faraday thick in this spectral range.

If available observations cover a more or less homogeneous spectral range from several cm and up to 1 m and longer, there is an attractive option to fit a particular model of depolarization to available observations to obtain (provided a realistic distributions of electron density and relativistic electrons are somehow known) spatial distribution of magnetic field along the line of sight. Such possibility mentioned already in [9] remains, however, an attractive perspective only. In particular, one needs 25 times longer observational time to get data of comparable quality at 100 wavelengths than at 4 wavelengths. Multiwavelength observations of spiral galaxies are available at the instant for a quite narrow spectral range located at long wavelengths [10]. Expectation that future development of the observational basis will open a possibility to formulate and solve an adequate inverse problem for magnetic field distribution along the line of sight is supported by a positive experience in technique of inverse Doppler imaging in investigations of stellar activity [11] and helioseismology (e.g., [12]), but mathematical problems to be resolved remain very substantial.

4 Concept of RM Synthesis

A fruitful compromise, which allows to use multi-wavelength observations and avoid an extended usage of high-brow mathematical technique of inverse problem theory, was suggested as RM Synthesis in [13].

It was Burn [2] who noted that complex polarized intensity $P = Q + iU$ obtained from a radio source is related to the Faraday dispersion $F(\phi)$ (which

is determined by emissivity and intrinsic position angle, see below) as

$$P(\lambda^2) = \int_{-\infty}^{\infty} F(\phi) e^{2i\phi\lambda^2} d\phi. \quad (3)$$

Here the Faraday depth ϕ is defined by

$$\phi(z) = -0.81 \int B_{\parallel} n_e dz'. \quad (4)$$

Following Eq. (3), P is the inverse Fourier transform of F . Correspondingly, the Faraday dispersion function F is the Fourier transform \hat{P} of complex polarized intensity

$$F(\phi) = \frac{1}{\pi} \hat{P}(k), \quad (5)$$

where $k = 2\phi$.

The idea of RM Synthesis is to use multi-wavelength data in order to find Faraday dispersion F as a function of Faraday depth ϕ . Of course, Faraday depth is far to be the desired magnetic field (or at least its line of sight component B_{\parallel}) as a function of position at the line of sight however the quantities are reasonably related one to the other to make finding of F an attractive destination (e.g., [14]). Comparison of various realizations of RM Synthesis in application to unresolved radio sources is presented in [15].

5 Wavelet based RM Synthesis

Realization of the attractive idea described above faces at least two obvious problems. From one hand, a straightforward understanding of Eq. (5) requires integration over the parameter λ^2 from $-\infty$ to $+\infty$ while according to its physical meaning $\lambda^2 > 0$. This problem can be resolved using the fact that the galactic magnetic field is symmetric in the respect to the galactic central plane. This symmetry gives a link between complex P for $\lambda^2 > 0$ and that one formally calculated for $\lambda^2 < 0$ [16]. Fortunately, exactly the same symmetry follows from the assumption that the source contains just one spectral detail in Faraday dispersion function [17]. The last assumption usually is exploited for RM Synthesis of unresolved radio sources.

From the other hand, performing a Fourier transform (even using symmetry argument), one needs to know the function for all values of λ^2 while in fact observations provide P for a limited spectral range $\lambda_{\min} < \lambda < \lambda_{\max}$. This problem can be in principle resolved by wavelet technique which allows to calculate contributions to the Fourier transform from each spectral range separately [16, 17]. Of course, a limited spectral range allows to isolate some spectral details in Faraday dispersion function only. Analysis performed in [18] shows that one can expect to isolate such details for which $\phi\lambda_{\min}^2 \leq \pi$, i.e. galaxy is Faraday thin at least at the shortest wavelength. It means that using

LOFAR data RM Synthesis can give information concerning turbulent components of galactic magnetic field only. Direct investigation of large-scale galactic magnetic field requires forthcoming facilities of SKA. This result looks for the first sight slightly disappointing, however each telescope allows to observe only some feature of celestial body of an interest and nobody expects that an optical telescope allows to see something, say, inside the Sun. Nevertheless, analysis of [18] stresses the important role of short wavelength observations.

There are indications [19] that RM Synthesis can be used for observational identification of helicity, i.e. crucial driver of galactic dynamo.

6 Conclusions

Summarizing results from the above cited papers, we conclude that RM Synthesis looks as an important tool for investigation of magnetic fields of spiral galaxies. Long wavelength observations allow a limited application of the method, while the expected facilities of SKA should allow such application in the full extent. Of course, it is desirable to combine RM Synthesis with options based on solution of inverse problem for multi-wavelength observations. Of course, fitting of any models to observational data needs to adopt the model to the contemporary understanding of magnetic field symmetries in a celestial body of interest. For spiral galaxies that is magnetic field symmetry in respect to the central plane of the galaxy, however for, say, magnetic field of a jet such symmetry has to be isolated in a particular research.

Acknowledgments. Fruitful discussions with S.A.Mao, R.Beck, P.Frick, L.Rudnick, R.Stepanov are acknowledged. The paper is supported by RFBR under grant 15-02-01407.

References

1. *R. Beck, A. Brandenburg, D. Moss et al.*, Ann. Rev. Astron. Astrophys., **34**, 155, 1996.
2. *B.J. Burn*, Mon. Not. Roy. Astron. Soc., **133**, 67, 1966.
3. *D.D. Sokoloff, A.A. Bykov, A. Shukurov et al.*, Mon. Not. Roy. Astron. Soc., **299**, 189, 1998.
4. *A.G. Pacholczyk*, Radio Galaxies. Oxford: Pergamon Press, 1977.
5. *A. Ruzmaikin, D. Sokoloff, A. Shukurov, R. Beck*, Astron. Astrophys., **230**, 284, 1990.
6. *E.M. Berkhuijsen, C. Horellou, M. Krause et al.*, Astron. Astrophys., **318**, 700, 1997.
7. *S.A. Mao, E. Zweibel, A. Fletcher et al.*, Astrophys. J., **800**, 92, 2015.
8. *D. Moss, A. Shukurov, D.D. Sokoloff et al.*, Astron. Astrophys., **335**, 500, 1998.
9. *A.A. Ruzmaikin, D.D. Sokoloff*, Astron. Astrophys., **78**, 1, 1979.
10. *G. Heald, R. Brawn, R. Edmonds*, Astron. Astrophys., **503**, 409, 2009.

11. *A.V. Goncharskij, V.V. Stepanov, V.L. Khokhlova, A.G. Yagola*, *Sov. Astron.*, **26**, 690, 1982.
12. *A.G. Kosovichev, K.V. Parchevskii*, *Sov. Astron. Lett.*, **14**, 201, 1988.
13. *M.A. Brentjens, A.G. de Bruyn*, *Astron. Astrophys.*, **441**, 1217, 2005.
14. *A.G. de Bruyn, M.A. Brentjens*, *Astron. Astrophys.*, **441**, 931, 2005.
15. *X.H. Sun, L. Rudnick, T. Akahori et al.*, *Astrophys. J.*, **149**, 60, 2015.
16. *P. Frick, D. Sokoloff, R. Stepanov, R. Beck*, *Mon. Not. Roy. Astron. Soc.*, **401**, L24, 2010.
17. *P. Frick, D. Sokoloff, R. Stepanov, R. Beck*, *Mon. Not. Roy. Astron. Soc.*, **414**, 2540, 2011.
18. *R. Beck, P. Frick, D. Sokoloff, R. Stepanov*, *Astron. Astrophys.*, **543**, A113, 2012.
19. *A. Brandenburg, R. Stepanov*, *Astrophys. J.*, **786**, 91, 2014.

Low Multipoles Anomalies of CMB Maps

O.V. Verkhodanov¹

E-mail: *vo@sao.ru*

We consider anomalies of cosmic microwave background observed at low multipoles of the WMAP and Planck cosmic missions. The possible origin of these features is discussed. We study difference of both missions data which is apparently connected with the local sources emission and/or systematics.

1 Introduction

The last decade of the cosmic microwave background (CMB) study was marked by several marvelous discoveries which changed the observational cosmology. The main cosmological parameters were measured with two satellites – WMAP and Planck.

The observations of the CMB radiation by the Wilkinson Microwave Anisotropy Probe (WMAP, <http://lambda.gsfc.nasa.gov>) [1, 2] were revolutionary in modern cosmology. The data were recorded in five bands: 23, 33, 41, 61, and 94 GHz with the measurements of intensity and polarization. The mission results include the CMB maps of anisotropy and polarization, the maps of foreground components (synchrotron and free-free emission, dust radiation), their power spectrum. The resolution of the CMB map restored with implementing the Internal Linear Combination (ILC) method [1] is $40'$. The angular power spectrum of CMB produced by the WMAP experiment allowed one to measure all the main cosmological parameters at the most precise level of observational cosmology (with accuracy less than 10%) [3].

The second set of maps and corresponding data were obtained in the European Space Agency experiment Planck (<http://www.rssd.esa.int/Planck/>) [4] and produced new possibilities in investigation of foreground components and radio sources in millimeter and submillimeter wavelengths. Planck observations were carried out at low frequency instrument (LFI bandwidths: 30, 44, 70 GHz) and high frequency instrument (HFI bandwidths: 100, 143, 217, 353, 545, 857 GHz). The resolution of the Planck CMB maps is $\sim 5'$. The Planck mission allowed one to obtain new and independent observational data.

Results of both experiments also contain some anomalies violated our expectation from the CMB Gaussian distribution. The most discussed ones [5] are Axis of Evil [6], Cold Spot [7], violation of parity in the power spectrum [8], asymmetry “North – South” in galactic coordinate system [9]. The Planck data

¹ Special astrophysical observatory RAS, Nizhnij Arkhyz, Russia

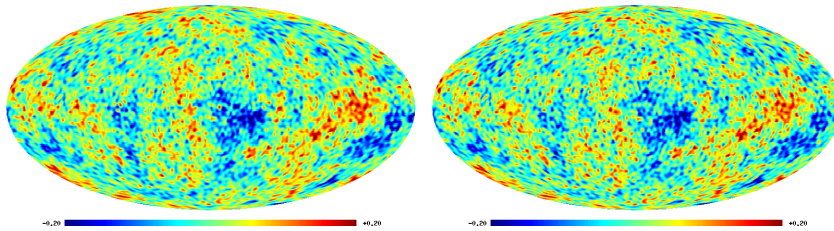


Figure 1: CMB maps restored from the WMAP (left, ILC map) and Planck (right, SMICA map) observational data and smoothed upto $\ell_{\max} = 100$.

added a new unexpected phenomena – too low amplitude of low harmonics [10]. All these anomalies occur at the largest angular scales ($\theta > 1^\circ$) and demonstrate observation statistical anisotropy being a sign of non-Gaussianity at low multipoles.

There are two basic approaches in understanding the origin of anomalies. The first one is based on suggestion of complex processes during early stages of the Universe. The second one follows the idea of connection of the anomalies with foregrounds and/or data analysis procedures.

Two basic properties of CMB allow one to separate its signal from foregrounds: (1) black body emission, so it has the same temperature at all wavelengths, and (2) correlation of CMB and foregrounds should be close to zero, because CMB is a random Gaussian process. In the simple case, the sought ILC temperature can be written as a linear combination of signal from the maps for different frequencies. The different versions of the ILC method and its variations exist both in pixel space and in harmonic space [11]. The maps restored in WMAP and Planck experiments are shown in Fig. 1.

For the restored CMB signal, the angular power spectrum is calculated using the so called $a_{\ell m}$ -coefficients $C(\ell) = \frac{1}{2\ell+1} \sum_{m=-\ell}^{\ell} |a_{\ell m}|^2$. The $a_{\ell m}$ -coefficients are obtained in the standard decomposition of the measured temperature variations on the sky, $\Delta T(\theta, \phi)$, in spherical harmonics (multipoles):

$$\Delta T(\theta, \phi) = \sum_{\ell=2}^{\infty} \sum_{m=-\ell}^{m=\ell} a_{\ell m} Y_{\ell m}(\theta, \phi). \quad (1)$$

2 The main WMAP and Planck CMB data anomalies

Axis of Evil. The Axis of Evil (Fig. 2) is the most famous among non-Gaussian features of the WMAP CMB data. The Axis unifies some problems which require special explanations. They are the planarity and alignment of the two harmonics, quadrupole and octupole, and, partly, the problem of extremely low amplitude of the quadrupole. Different estimations of the significance of existence of this axis, and several hypotheses on its origin were made. Various studies (e.g., [12, 13]) investigated the contribution of background components and their influence on the alignment of multipoles ($\ell = 2$ and $\ell = 3$), and indicated a small probability

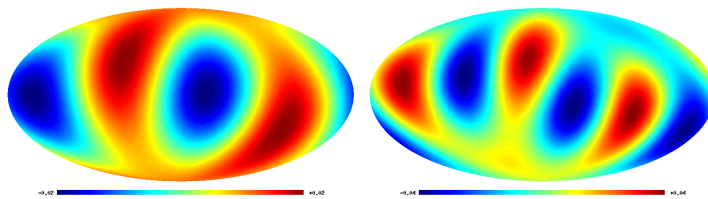


Figure 2: Axis of Evil: planarity and alignment of the quadrupole (left) and the octupole (right) on the WMAP CMB map.

of the background effect on the orientation of the low multipoles. Randomness of such an effect is estimated by the authors as unlikely at the significance level exceeding 98% and excludes the effect of residual contribution of background components.

Some cosmological models were developed to explain the prominence of the axis in the orientation of multipoles. They include the anisotropic expansion of the Universe, rotation and magnetic field [14, 15].

There are some hints demonstrating that the problem of existence of Axis of Evil can be connected with the instability of CMB reconstruction at low multipoles ($2 \leq \ell \leq 10$) in ILC method [16, 17]. Another possible solution of the problem is to construct the separation methods on the homogeneous samples of pixels where possible to tune selection of subsample in such a way that the quadrupole amplitude of the restored map grows and phase changes, so, no axis of evil exists [18].

Using new data, the Planck team [10] detected the angle between planes of quadrupole and octupole is equal $\sim 13^\circ$ (against $\sim 3^\circ$ or $\sim 9^\circ$ for WMAP data at different observational years) and declared that significance of the quadrupole-octupole alignment is substantially smaller than for the WMAP data, falling to almost 98% confidence level. Later, Copi et al. [19] demonstrated that the WMAP and Planck data confirm the alignments of the largest observable CMB modes in the Universe. Using different statistical methods to control the mutual alignment between the quadrupole and octupole, and the alignment of the plane defined by the two harmonics with the dipole direction, the authors obtained that both phenomena are at the greater than 3σ level for Planck CMB maps studied.

Cold Spot. The next exited feature discussed is the Cold Spot (CS) (Fig. 3). This is a cold region exhibiting a complex structure identified in the CMB using spherical Mexican hat wavelets [7]. The non-Gaussianity of the signal in the Southern hemisphere was explained precisely by the existence of this region. The galactic coordinates of center of the spot are $b = -57^\circ, l = 209^\circ$. The probability of the signal in CS, being consistent with the Gaussian model if spherical wavelets are used, is about 0.2% [7]. After obtaining indication of the signal non-Gaussianity at the CS as well as messages on the reduced density of source [20] in smoothed maps of radio survey NVSS at 1.4 GHz, several hypotheses concerning the origin of the Cols Spot were discussed which were related to the integrated Sachs–Wolfe effect, the topological defect, anisotropic expansion, the artifact of data analysis,

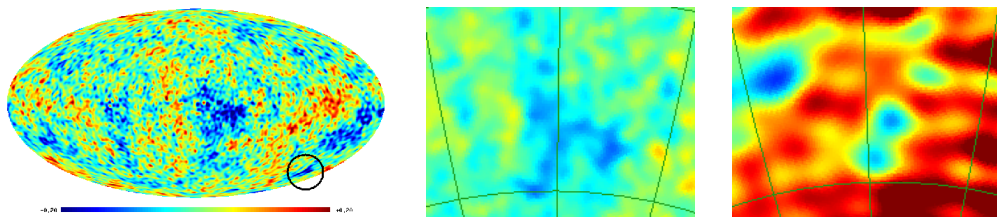


Figure 3: Cold Spot: position of the Cold Spot on the WMAP CMB map (left) and its shape (center) and 408 MHz map (right) with synchrotron emission.

and simply a random deviation (see the review [21]). As was noted in [22], the possible galactic foreground residuals in the CMB maps can produce such a type of the spot as a part of non-Gaussianity at low multipoles. We should add that the CS is also manifested in the data of 1982 in maps of a low-frequency survey where synchrotron radiation contributes significantly to the background (Fig. 3, right). In favor of the hypothesis of the CS being the Galactic phenomena, the following fact testifies. There exists the high correlation of positions of peaks of CMB fluctuation and galactic magnetic field distribution [23].

Violation of the power spectrum parity. A remarkable manifestation of non-Gaussian properties of low multipoles consists in parity asymmetry first noticed in [8] and confirmed in Planck data [10]. For a Gaussian random field of primary perturbations $\Phi(\mathbf{k})$ with a flat power spectrum, the presence of a plateau in the CMB angular power spectrum is expected at low multipoles, which is due to the Sachs–Wolfe effect, namely, to the fact that $\ell(\ell + 1)C_\ell \approx \text{const}$. Spherical harmonics change as $Y_{\ell m}(\hat{\mathbf{n}}) = (-1)^\ell Y_{\ell m}(-\hat{\mathbf{n}})$, when the coordinates are reversed. Therefore, an asymmetry in the angular power spectrum for even and odd harmonics can be regarded as the asymmetry of the power of even and odd components of map. The authors [8] found the power of odd multipoles to systematically exceed the power of even multipoles of low ℓ and termed this phenomenon “parity asymmetry”. To describe such an asymmetry quantitatively, the following quantities are proposed for consideration: $P^+ = \sum_{\text{even } \ell < \ell_{\max}} \ell(\ell + 1)C_\ell/2\pi$, $P^- = \sum_{\text{odd } \ell < \ell_{\max}} \ell(\ell + 1)C_\ell/2\pi$. Using the data of WMAP power spectrum and the results of Monte Carlo simulations, the authors [8] calculated the ratio P^+/P^- for the multipole ranges $2 \leq \ell \leq \ell_{\max}$, where ℓ_{\max} lies between 3 and 23. Comparing P^+/P^- for the WMAP data with the simulated maps ratio allows estimating the quantity p equal to the fraction of simulated spectra in which P^+/P^- is less than or equal to the same quantity for the WMAP map. The value of p was found to reach its lower boundary at $\ell_{\max} = 18$, where p equals 0.004 and 0.001 for the data obtained by the WMAP mission during five and three years of observations, respectively. This fact means that there is a preference for odd multipoles $2 \leq \ell \leq 18$ in the WMAP data at a confidence level of 99.6% with a screening mask imposed on the data, and of 99.76% without any mask. The authors believe the low amplitude of the WMAP CMB quadrupole may be part of the same anomaly as the parity asymmetry.

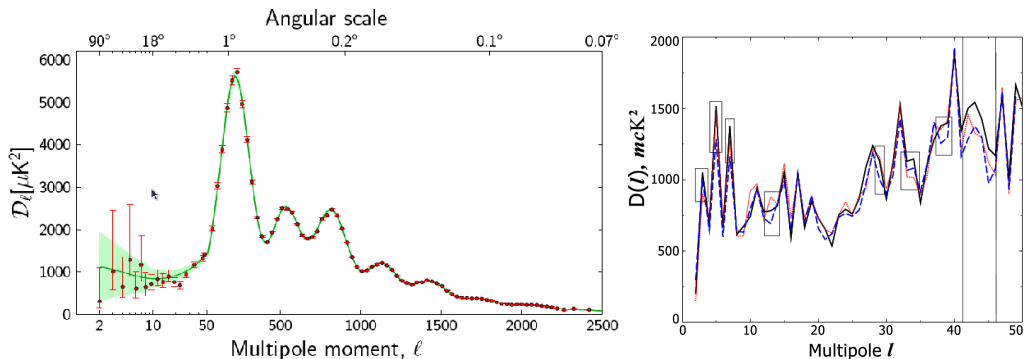


Figure 4: Right: CMB angular power spectrum of the 1st Planck data release. Left: the angular power spectrum $D(\ell) = \ell(\ell + 1)C_\ell/2\pi$ for $2 \leq \ell < 50$. The solid line shows the 7th year WMAP ILC data release. The dotted line marks WMAP9 ILC data. The Planck data are marked by the dashed line. The rectangles show the most different amplitudes. The vertical lines mark limits of $\ell \in [41, 46]$.

Hemispherical Asymmetry. The asymmetry of hemispheres power (see, e.g., Fig. 1) was detected just after publishing the first year all sky maps of the WMAP [9]. Then, in [24], the some calculations based on the angular power spectrum were presented and shown that this spectrum, when estimated locally at different positions on the sphere, appears not to be isotropic. Park [25] also presented evidence for the existence of such hemispherical asymmetry, in which a particular statistical measure is considered to change discontinuously between two hemispheres on the sky, applying Minkowski functionals to the WMAP data. Since the preferred direction according to Eriksen et al. [9] lays close to the ecliptic plane, it was also demonstrated that the large-angular scale N -point correlation functions were different in behavior when computed on ecliptic hemispheres.

The observed properties of the Planck data are consistent with a remarkable lack of power in a direction towards the north ecliptic pole, consistent with the simpler one-point statistics [10].

3 Difference of WMAP and Planck power spectra

One of the main anomalies first detected in the Planck data was the lack of power at low multipoles detected for angular power spectrum $C(\ell)$. Using the WMAP and Planck officially published spectra, we can compare them via the calculation of the difference of maps including only the harmonics with maximum $C(\ell)$ difference (Fig. 4, right).

Following [26], let us consider the differences of maps corresponding to the harmonics having the maximum difference of power. These ranges are marked by rectangles on Fig. 4. The vertical lines demonstrate limits of the multipole range in $\ell \in [41, 46]$. On Figs. 5, 6, there are shown maps of harmonic differences at $\ell = 5$ and $\ell = 7$, respectively. Some features of these differences show the

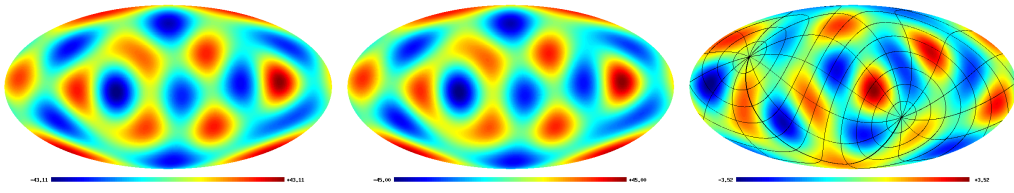


Figure 5: Left to right: the map of $\ell = 5$ of the Planck CMB map SMICA, the $\ell = 5$ of the ILC WMAP9 map, and the map of these signals difference. The equatorial coordinate grid is overlaid on the map of difference.

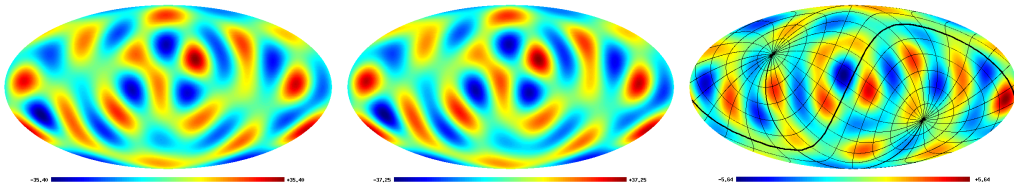


Figure 6: Left to right: the map of $\ell = 7$ of the Planck CMB map SMICA, the $\ell = 7$ of the ILC WMAP9 map, and the map of these signals difference. The ecliptic coordinate grid is overlaid on the map of difference.

position of spots along the Galactic plane, sensitivity of difference map at $\ell = 5$ to the equatorial coordinate system (equatorial poles are placed in singular points – saddles), and the axis of the multipole $\ell = 7$ lays on the Galactic plane and simultaneously, the saddle points of $\ell = 7$ are placed in ecliptic poles. The map of multipole difference at $\ell = 13$ (angular size of $\sim 6.5^\circ$) contains a feature similar to the harmonic $\ell = 7$ where the ecliptic poles are placed in singular points – local map minima and maxima. The multipole difference at the scales $\ell = 29$ ($\sim 3^\circ$) and $\ell = 37$ ($\sim 2.5^\circ$) contains a similar structure of spots placement. One line drawn by the very contrast spots formed with m -modes combinations of the $\ell = 29$ and $\ell = 37$ coincides with the ecliptic plane. Curiously, that a structure of the bright spots placement for $\ell = 29$ and $\ell = 37$ in the right hemisphere corresponds the anisotropic model Bianchi_{VIII} discussed in [10]. There is the range of multipoles ($\ell \in [41; 46]$) where the spectrum strongly differ for the WMAP and Planck data (Figs. 4, 7). The map difference for these multipole range shows the extended structure near the Galactic center.

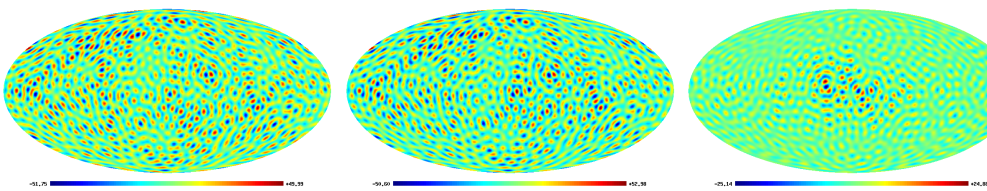


Figure 7: Left to right: the summarized signal of multipole $\ell \in [41, 46]$ for the Planck CMB map SMICA, harmonics $\ell = 41-46$ of WMAP9 ILC, and difference of these signals.

Note, that there are two important moments observed in multipole differences. First, all the maps of multipole difference with high amplitude contain features tied with galactic, ecliptic or/and equatorial (terrestrial) coordinate systems. Second, there is the $\Delta\ell = 8$ period for multipoles numbers having a big difference in amplitude. Peculiar harmonics have numbers $\ell = 5, 13, 29, 37, 45$.

4 Summary

As we can see from the details of the CMB anomalies mentioned above, most of them manifest the properties sensitive to local environment. Three main environments of the cosmic observatory are displayed in the CMB signal distribution. They are our Galaxy, the Solar (ecliptic) system and some features from the equatorial system. The Galaxy is a source of the non-Gaussian residuals visible in CMB spots positions (see [21]). The Cold Spot is a feature visible on a synchrotron map and on a map of the Faraday rotation depth. It could be due to any ionized cloud from Galaxy or its vicinity.

The Solar system objects are an additional residual source on the CMB map which is difficult to account using standard component separation methods. Possible sources of a residual signal are the antenna far sidelobes sensitive to the Sun and bright planets, a solar wind focusing by the Earth magnetosphere and passing through the Lagrange point L2, the objects at boundary of Solar system like the Kuiper belt.

The equatorial system features detected in some CMB correlation maps or in the single harmonic maps can be due by the influence of the Earth microwave emission via the antenna back lobes or possible Solar wind emission modulated by the Earth magnetosphere where the magnetic axis is close the Earth rotation axis.

It is necessary to note that there are some anomalies in the Planck data detected at high ($\ell > 600$) harmonics. There is a disagreement between cosmological parameters determination using the CMB angular power spectrum (including or not other experiments) and using only the Sunyaev–Zeldovich clusters [27]. Such a discordance, as discussed also in this paper, can be explained by the biased estimates of cluster parameters with the X-ray data.

And we can note that

- 1) WMAP and Planck data have practically the same low multipole anomalies, all the visible anomalies probably can be understood in the frame of the local (galactic and ecliptic) sources of microwave emission,
- 2) the difference of WMAP and Planck power spectra looks like one due to systematic effects of maps preparation (e.g. due to beam residuals).

Acknowledgments. Author is thankful to Conference Organizing Committee for hospitality. Author is also grateful to NASA for possibility to use NASA Legacy Archive where WMAP maps stored and ESA for open access to observational results in the Planck Legacy Archive. The GLESP (<http://www.glesp.nbi.dk>) package [28] was used to process the CMB maps on a sphere.

References

1. *C.L. Bennett, M. Halpern, G. Hinshaw et al.*, *Astrophys. J. Suppl.*, **148**, 1, 2003.
2. *N. Jarosik, C.L. Bennett, J. Dunkley et al.*, *Astrophys. J. Suppl.*, **192**, 14, 2011.
3. *C.L. Bennett, D. Larson, J.L. Weiland et al.*, *Astrophys. J. Suppl.*, **208**, 20, 2013.
4. *Planck Collaboration*, *Astron. Astrophys.* **571**, A1, 2014.
5. *C.L. Bennett, R.S. Hill, G. Hinshaw et al.*, *Astrophys. J. Suppl.*, **192**, 17, 2011.
6. *K. Land, J. Magueijo*, *Phys. Rev. Lett.*, **95**, 071301, 2004.
7. *M. Cruz, E. Martinez-Gonzalez, P. Vielva, L. Cayon*, *Mon. Not. Roy. Astron. Soc.*, **356**, 29, 2005.
8. *J. Kim, P. Naselsky*, *Astrophys. J. Lett.*, **714**, L265, 2010.
9. *H.K. Eriksen, F.K. Hansen, A.J. Banday et al.*, *Astrophys. J.*, **605** 14, 2014.
10. *Planck Collaboration*, *Astron. Astrophys.*, **571**, A23, 2014.
11. *S.M. Leach, J.-F. Cardoso, C. Baccigalupi et al.*, *Astron. Astrophys.*, **491**, 597, 2008.
12. *C.J. Copi, D. Huterer, D.J. Schwarz, G.D. Starkman*, *Mon. Not. Roy. Astron. Soc.*, **367**, 79 (2006).
13. *A. Gruppuso, C. Burigana, J. Cosmol. Astropart. Phys.*, **08**, 004, 2009.
14. *M. Demianski, A.G. Doroshkevich*, *Phys. Rev. D*, **751**, 3517, 2007.
15. *T. Koivisto, D.F. Mota, J. Cosmol. Astropart. Phys.*, **06**, 018, 2008.
16. *P.D. Naselsky, O.V. Verkhodanov*, *Astrophys. Bull.*, **62**, 203, 2007.
17. *P.D. Naselsky, O.V. Verkhodanov, M.T.B. Nielsen*, *Astrophys. Bull.*, **63**, 216, 2008.
18. *A.G. Doroshkevich, O.V. Verkhodanov*, *Phys. Rev. D*, **83**, 3002, 2011.
19. *C.J. Copi, D. Huterer, D.J. Schwarz, G.D. Starkman*, *Mon. Not. Roy. Astron. Soc.*, **449**, 3458, 2015.
20. *L. Rudnick, S. Brown, L.R. Williams*, *Astrophys. J.*, **671**, 40, 2007.
21. *O.V. Verkhodanov*, *Phys. Usp.*, **55**, 1098, 2012.
22. *P.D. Naselsky, P.R. Christensen, P. Coles et al.*, *Astrophys. Bull.*, **65**, 101, 2010.
23. *M. Hansen, W. Zhao, A.M. Frejsel et al.*, *Mon. Not. Roy. Astron. Soc.*, **426**, 57, 2012.
24. *F.K. Hansen, A.J. Banday, K.M. Górski*, *Mon. Not. Roy. Astron. Soc.*, **354**, 641, 2004.
25. *C.-G. Park*, *Mon. Not. Roy. Astron. Soc.*, **349**, 313, 2004.
26. *O.V. Verkhodanov*, *Astrophys. Bull.*, **69**, 330, 2014.
27. *Planck Collaboration*, *Astron. Astrophys.*, **571**, A20, 2014.
28. *A.G. Doroshkevich, O.V. Verkhodanov, P.D. Naselsky et al.*, *Int. J. Mod. Phys. D*, **20**, 1053, 2011.

* The color figures are available online in the Proceedings at <http://www.astro.spbu.ru/sobolev100/>.

Structure of Galaxy Groups and Clusters and Measurement of Their Masses

A.I. Kopylov¹, F.G. Kopylova¹

E-mail: *flera@sao.ru*

We report the results of measurement and comparison of masses for a sample of 29 groups and clusters of galaxies ($z < 0.1$). We use the SDSS archive data to determine dynamical masses from the one-dimensional dispersion of radial velocities for virialized regions of radii R_{200} and R_e . Our method for determination of effective radius of galaxy systems from the cumulative distribution of the number of galaxies depending on squared cluster-centric distance allowed us to estimate masses $M_{1/2}$ (within R_e), which are related to the masses enclosed within R_{200} : $M_{200} \sim 1.65 M_{1/2}$. A comparison of the inferred dynamic masses and the hydrostatic masses determined from the radiation of hot gas in galaxy groups and clusters (based on published data) led us to conclude that the inferred masses for the main sample of 21 groups and clusters agree to within 12%.

Galaxy clusters are the largest gravitationally bound structures in the Universe. About 80–90% of their mass is in the form of dark matter, and the remaining mass is represented by baryons, most of which (10–20%) are in the form of hot diffuse plasma with $T > 10^7$ K (it is the main component of the inner medium of galaxy clusters), which emits mostly in the X-ray domain. Galaxies contribute only several percent of the cluster mass. The mass function of galaxy clusters is sensitive to cosmological parameters, turning the measurement of their accurate masses a challenging task [1].

The aim of this study is to measure the dynamical masses of 29 groups and clusters of galaxies using various methods, intercompare the resulting mass estimates, and compare them with the masses inferred from the X-ray emission of gas. We have determined dynamical masses M_{200} of the clusters from the dispersion of radial velocities of galaxies assuming that the systems are in virial equilibrium. The empirical radius R_{200} and the group or cluster mass can be estimated by the equations: $R_{200} = \sqrt{3}\sigma/(10H(z))$ Mpc [2] and $M_{200} = 3G^{-1}R_{200}\sigma^2$, where $H(z)$ is the Hubble constant at redshift z , and G is the gravitational constant. The masses $M_{1/2}$ of spheroidal galaxies and clusters of galaxies with measured dispersions of radial velocities can be determined for the characteristic radius, which is approximately equal to the 3D radius of the galaxy containing half of its luminosity. Thus, the virial mass of the cluster is measured, which is independent of the anisotropy of galaxy velocities,

¹ Special Astrophysical Observatory RAS, Nizhnij Arkhyz, Russia

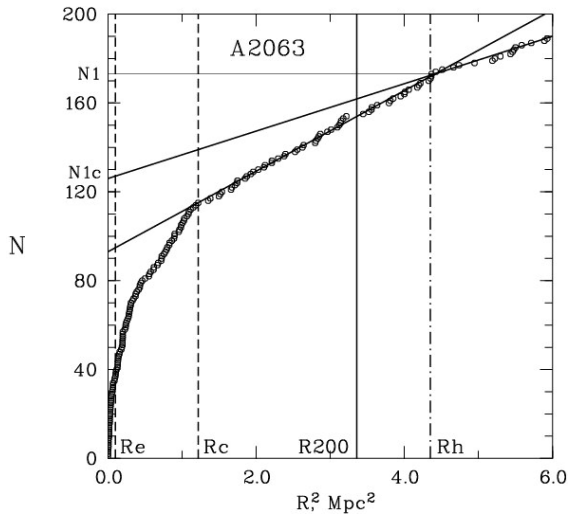


Figure 1: Cumulative distribution of the number of galaxies as a function of squared clustercentric distance for the A2063. The solid vertical line indicates the R_{200} . The dashed-and-dotted line indicates the R_h radius bounding the cluster: core (c) and halo (h); the dashed lines indicate the R_c and R_e radii. The two solid lines show the distribution of galaxies located inside the halos of groups and clusters and the distribution of galaxies that do not belong to the cluster.

$M_{1/2} = 3G^{-1} \sigma_{1/2}^2 r_{1/2}$ [3], where $r_{1/2} = 4/3R_e$ (R_e is the effective radius containing half of the luminosity emitted by the cluster or group).

We use a graphical method to determine the size and the number of galaxies of the system (R_h , N_h) and its effective radius containing half of the near-infrared luminosity (Fig. 1).

Our main results are as follows (see also [4]):

1. We developed an empirical method for identifying galaxy groups or clusters from the observed cumulative distribution of the number of galaxies depending on squared cluster-centric distance.
2. We show that the dynamic masses of galaxy groups and clusters for regions of radii R_{200} and R_e are related as $M_{200} \sim 1.65 M_{1/2}$.
3. The inferred dynamic (M_{200} and $1.65 M_{1/2}$) and hydrostatic ($M_{X,200}$) masses for 21 groups and clusters of galaxies agree with each other to within 12%.

References

1. A.A. Vikhlinin, A.V. Kravtsov, M.L. Markevich et al., *Uspekhi Fiz. Nauk*, **184**, 349, 2014.
2. R.G. Carlberg, H.K.C. Yee, E. Ellingson et al., *Astrophys. J. Lett.*, **485**, L13, 1997.
3. J. Wolf, G.D. Martinez, J.S. Bullock et al., *Mon. Not. Roy. Astron. Soc.*, **406**, 1220, 2010.
4. A.I. Kopylov, F.G. Kopylova, *Astron. Bull.*, **70**, 243 2015.

The Fundamental Plane and Other Scaling Relations of Groups and Clusters of Galaxies

F.G. Kopylova¹, A.I. Kopylov¹

E-mail: *flera@sao.ru*

We present the scaling relations of galaxy groups and clusters derived by using archival data from SDSS and 2MASX catalogs. We applied a new method for determining the size of the galaxy clusters [1] and their effective radius as the radius enclosing half of the galaxies (not half of the luminosity), since the luminosity of the brightest galaxies in groups can exceed 50% of the total luminosity of the group. The characteristics $\log L_K$, $\log R_e$ and $\log \sigma_{200}$ obtained for 94 systems of galaxies ($0.012 < z < 0.09$ and Virgo) define the Fundamental Plane (FP) relation with the scatter of 0.15 that is similar in slope to the FP of clusters of galaxies measured in [2, 3] by other methods and in other bands. We find that the FP of the stellar population of the systems of galaxies in the near-infrared has the slope $L_K \propto R_e^{0.70 \pm 0.13} \sigma^{1.34 \pm 0.13}$ and the FP of the hot gas does $L_X \propto R_e^{1.15 \pm 0.39} \sigma^{2.56 \pm 0.40}$ or $L_K \propto R_e^{0.81 \pm 0.21} \log L_X^{0.30 \pm 0.05}$.

Dynamical and photometric parameters of the early-type galaxies (central stellar velocity dispersion σ , effective radius R_e , mean surface brightness $\langle I_e \rangle$) form the so-called Fundamental Plane [4, 5]. The FP of the galaxies has a significantly lower scatter compared with the earlier obtained Faber–Jackson relation between luminosity and velocity dispersion and the Kormendy relation between surface brightness and radius. Originally, the FP of clusters of galaxies was constructed using observational characteristics of a sample of 16 rich clusters of galaxies ($z < 0.2$) [2]. As a result of fitting, with residuals being minimized in L , they obtained the FP in the form: $L \propto R_e^{0.89 \pm 0.15} \sigma^{1.28 \pm 0.11}$.

To construct the scaling relations of our systems of galaxies (see the resume above), we used the one-dimensional dispersion of radial velocities of galaxies σ_{200} found within the radius R_{200} , near-infrared luminosity L_K , and effective radius R_e , enclosing half of galaxies, derived from the observed cumulative galaxy distribution considered as a function of the squared cluster-centric distance. The X-ray luminosity is based on the published data, e.g. [6, 7, 8]. We have found that the form of the FP of groups and clusters is consistent with the FP of the early-type galaxies (Fig. 1) defined in the same way. But they have different zero-points occurring, as we established, due to the difference in the mass-to-light ratio of galaxies and systems of galaxies. The fourth variable, the mass-to-light ratio, included by us in our FP reduces the scatter by about 16% [9], but the slope of the FP does not change.

¹ Special Astrophysical Observatory RAS, Nizhnij Arkhyz, Russia

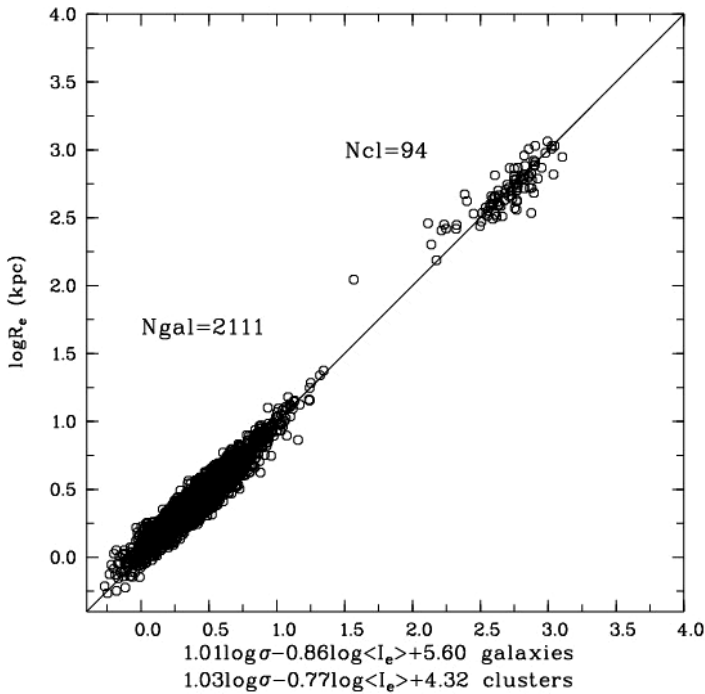


Figure 1: The Fundamental Plane of the galaxies, groups and clusters of galaxies. The effective radius R_e is the radius enclosing half of the galaxies.

References

1. A.I. Kopylov, F.G. Kopylova, *Astroph. Bull.*, **70**, 243, 2015.
2. R. Schaeffer, S. Maurogordato, A. Cappi, F. Bernardeau, *Mon. Not. Roy. Astron. Soc.*, **263**, L21, 1993.
3. M. D'Onofrio, D. Bettoni, D. Bindoni et al., *Astron. Nachr.*, **334**, 373, 2013.
4. S. Djorgovski, M. Davis, *Astrophys. J.*, **313**, 59, 1987.
5. A. Dressler, D. Lynden-Bell, D. Burstein et al., *Astrophys. J.*, **313**, 42, 1987.
6. H. Ebeling, A.C. Edge, H. Böhringer et al., *Mon. Not. Roy. Astron. Soc.*, **301**, 881, 1998.
7. H. Böhringer, W. Voges, J.P. Huchra et al., *Astrophys. J. Suppl.*, **129**, 435, 2000.
8. A. Mahdavi, M.J. Geller, *Astrophys. J.*, **607**, 202, 2004.
9. F.G. Kopylova, A.I. Kopylov, *Astroph. Bull.*, **71**, 2016.

Simulation of CH₃OH Masers

A.V. Nesterenok¹

E-mail: *alex-n10@yandex.ru*

A model of CH₃OH maser is presented. Two techniques are used for the calculation of molecule level populations: the accelerated lambda iteration (ALI) method and large velocity gradient (LVG), or Sobolev, approximation. The methods are found to give similar results, provided the gas velocity change across the cloud due to the velocity gradient is much larger than the Doppler line width.

1 Introduction

Intense maser transitions of the CH₃OH molecule are observed towards high-mass star-forming regions. The high brightness temperature of the maser emission permits us to observe them with the very long baseline interferometry (VLBI) technique, achieving both very high angular and velocity resolutions. Modeling of the maser pumping can provide estimates of the physical conditions in the maser regions [1]. The current study is aimed at modeling of the pumping mechanism of methanol masers. The zone of validity of the LVG approximation is discussed.

2 Results

We consider the one-dimensional model of a flat gas-dust cloud. The cloud consists of a mixture of H₂ and CH₃OH molecules, He atoms, and dust particles. The physical parameters of the cloud are the following: number density of H₂ molecules $N_{\text{H}_2} = 5 \times 10^6 \text{ cm}^{-3}$, number density of CH₃OH (A- and E-species) $N_{\text{m}} = 100 \text{ cm}^{-3}$, gas temperature $T_{\text{g}} = 150 \text{ K}$, dust temperature $T_{\text{d}} = 150 \text{ K}$, micro-turbulent speed $v_{\text{turb}} = 0.5 \text{ km s}^{-1}$, velocity gradient $dv/dz = 0.05 \text{ km s}^{-1} \text{ AU}^{-1}$. Let us define the resonance region length $\Delta z_{\text{D}} = v_{\text{D}} dv/dz$, where v_{D} is the velocity width of the spectral line profile. The LVG approximation with the full treatment of continuum effects [2] and the ALI method [3] were used in the calculations of methanol level populations and line intensities. The detailed description of the model is given in our paper [4].

Fig. 1 shows the dependence of the gain of the maser line at 6.7 GHz at the line center on the cloud depth calculated by means of the ALI method and the LVG approximation. There is a significant discrepancy in the results of two methods at the cloud height $H = 30 \text{ AU}$. The gain has negative values at almost all cloud depths according to accurate calculations, while the LVG approximation provides

¹ Ioffe Institute, Saint Petersburg, Russia

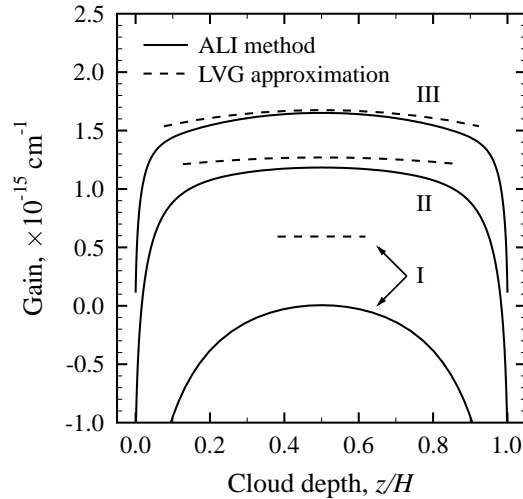


Figure 1: The gain of the 6.7 GHz $5_1 \rightarrow 6_0$ A⁺ maser line as a function of the cloud depth. The results are presented for three values of the cloud height: (I) 30 AU; (II) 90 AU; (III) 150 AU. At the parameters in question, $\Delta z_D = 11.5$ AU.

high positive values of the maser gain. There is an agreement between the results of two techniques at large cloud height – the difference between the gain values at the cloud centre is about 10 per cent at $H = 90$ AU and about 2 per cent at $H = 150$ AU. The LVG approximation reproduces the results of accurate radiative transfer calculations at large cloud heights and high velocity gradients: the cloud height has to be of the order of or greater than 5–10 lengths of the resonance region.

References

1. *A.M. Sobolev, M.D. Gray*, Proc. IAU Symp. No. 287, 2012, p. 12.
2. *D.G. Hummer, G.B. Rybicki*, Astrophys. J., **293**, 258, 1985.
3. *G.B. Rybicki, D.G. Hummer*, Astron. Astrophys., **245**, 171, 1991.
4. *A.V. Nesterenok*, Mon. Not. Roy. Astron. Soc., **455**, 3978, 2016.

Correlation of Radial Fluctuations in Deep Galaxy Surveys

S.I. Shirokov¹, Yu.V. Baryshev¹

E-mail: *lakronous@mail.ru*

Fluctuations of the number of galaxies in different catalogs are compared using the method of estimation of sizes and amplitudes of the radial fluctuations for different redshift bins. The Pearson correlation coefficient of fluctuations derived for these samples has the value $\rho = 0.7 \pm 0.12$ for the redshift interval $0.1 < z < 1.7$. This correlation of independent surveys of different research groups confirms the existence of super-large galaxy structures with sizes up to 1000 Mpc/h.

1 Statement of the problem

Determination of the maximum size of large-scale inhomogeneities in the distribution of galaxies is one of the most important problems in the modern observational cosmology.

For example, the Sloan Digital Sky Survey shows that at small redshifts there are inhomogeneity structures with a size of 400 Mpc/h. This work shows that there are similar and larger structures on large redshifts in the beam surveys. These structures should be correlated in the same fields in independent surveys of different research groups.

2 The method

Estimation of the fluctuation amplitude and size within galaxy distributions method (Fig. 1) was first proposed in [1] and modified in [2]. The left panel of the figure illustrates the wide-angle (CfA, 2df, SDSS) and beam (zCOSMOS, UVISTA, ALHAMBRA) surveys. The right panel shows the visible and model (uniform) galaxy distributions for the beam survey. The gray areas indicate the fields of deficiency or excess of the galaxy number. The fluctuation amplitude is a ratio of the visible galaxy number to the model galaxy number. The fluctuation size is a distance between the zero intersections of fluctuations with different signs.

The compared catalogs are as follows: ALHAMBRA [3], UltraVISTA [4], 10k-zCOSMOS [5], XMM-COSMOS [6], and HDF-N [7].

Table 1 shows the Pearson correlation coefficient ρ , its error σ_ρ , and its authenticity R from Student's table that were used to indicate the catalogs correlation.

¹ Saint Petersburg State University, Russia

Table 1: Correlation coefficients

The catalogs pair	ρ	σ_ρ	R
ALH-F4 & XMM-COSMOS	0.82	0.29	0.975
ALH-F4 & UVISTA	0.59	0.36	0.9
ALH-F4 & zCOSMOS	0.58	0.2	0.995
ALH-F5 & HDF-N	0.61	0.21	0.99

3 Results

In the deep COSMOS field there are fluctuations of the number of galaxies on the redshift $z \sim 2$ with the amplitude of 20% and the linear dimensions varying from 500 to 1500 Mpc.

The independent beam surveys of the COSMOS field are consistent in both the amplitudes and the linear dimensions of inhomogeneities with the correlation coefficient equal to 0.7 ± 0.12 .

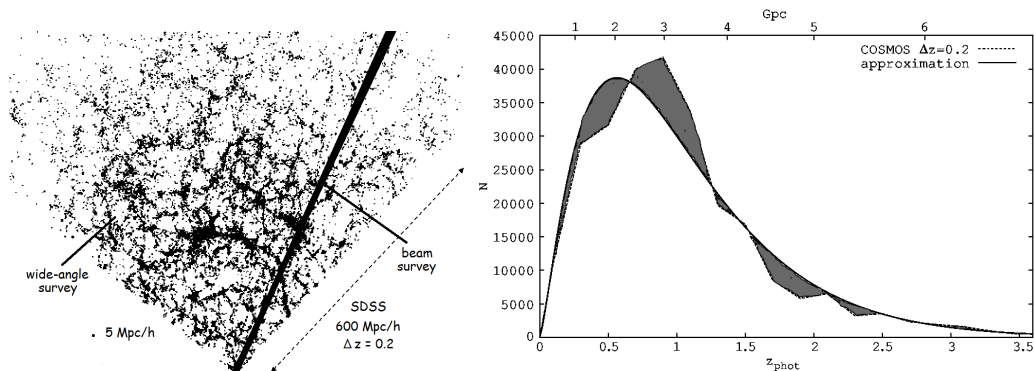


Figure 1: The method illustration.

Acknowledgments. S.S. and Yu.B. thank for the partial financial support the St. Petersburg State University research project No. 6.38.18.2014.

References

1. N.V. Nabokov, Yu.V. Baryshev, *Astrophys.*, **53**, 91, 2010.
2. S.I. Shirokov, D.I. Tekhanovich, Yu.V. Baryshev, *Vestn. Leningr. Univ.*, 1, **59**, 659, 2014.
3. A. Molino, N. Benitez, M. Moles et al., *Mon. Not. Roy. Astron. Soc.*, **441**, 2891, 2014.
4. A. Muzzin, D. Marchesini, M. Stefanon et al., *Astrophys. J. Suppl.*, **206**, 8, 2013.
5. K. Kovac, S.J. Lilly, O. Cucciati et al., *Astrophys. J.*, **708**, 505, 2010.
6. M. Brusa, F. Civano, A. Comastri et al., *Astrophys. J.*, **716**, 348, 2010.
7. <http://www.stsci.edu/ftp/science/hdf/hdf.html>

The influence of Small Scale Magnetic Field on the Polar Cap X-Ray Luminosity of Old Radio Pulsars

A.I. Tsygan¹, D.P. Barsukov^{1,2}, K.Y. Kraav²

E-mail: *bars.astro@mail.ioffe.ru*

The influence of small-scale magnetic field on the polar cap heating by reverse positrons is considered. We use the polar cap model with steady space charge limited electron flow. To calculate the electron-positron pairs production rate we take into account only the curvature radiation of primary electrons and its absorption in magnetic field. The reverse positron current is calculated in the framework of two models: rapid and gradually screening. It is shown that some pulsars are better described by the rapid screening model and some other pulsars have better agreement with calculation by the gradually screening model.

The polar caps of old radio pulsars are heated by reverse positrons. Such positrons emerge nearby the upper plate of the inner gap, are accelerated within it and hit to the neutron star surface causing the polar cap heating. The reverse positron current is calculated in the framework of two models: rapid [1] and gradual [2, 3] screening. In the first model electron-positron plasma rapidly screens the electric field above the inner gap that leads to a small reverse positron current and hence not so large polar cap heating. In the second model small electric field exists above the inner gap. It causes a substantial increasing of the reverse positron current and hence leads to a strong polar cap luminosity L_{pc} .

The result of calculation of L_{pc} for various ratios of small scale surface magnetic strength B_{sc} to strength B_{dip} of dipolar field is shown in Fig. 1. The polar cap luminosity L_{pc} calculated in the framework of the rapid screening model is shown by slant hatched region and calculated in the framework of the gradually screening model is shown by vertically hatched region.

The discrepancy between the calculated and observed values may be due to presence of some viscous force acting on positrons. The force may be related to the radiation closed inside the gap [11] or radiation coming from deep layers of a neutron star [12].

Acknowledgments. The work of D.P.B. was partly supported by the RFBR (project 13-02-00112).

¹ Ioffe Institute, Saint Petersburg, Russia

² SPbPU, Saint Petersburg, Russia

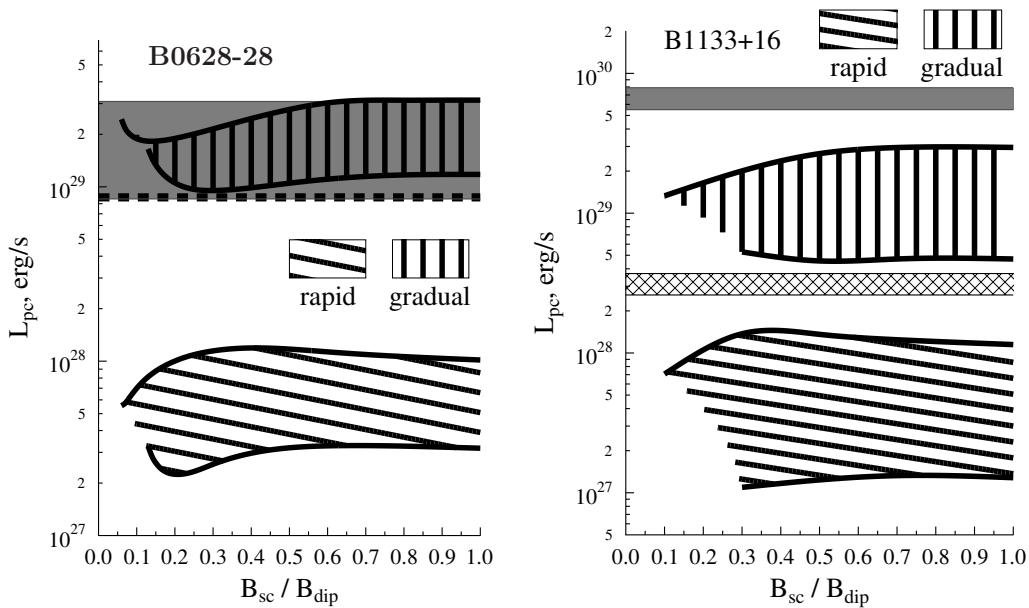


Figure 1: Left: the polar cap luminosity L_{pc} for B0628–28, $B_{dip} = 6.0 \times 10^{12}G$, $P = 1.24s$, $\tau = 2.8 \times 10^6$ years [4], inclination angle $\chi = 30^\circ$ is taken from [5]. The observed L_{pc} range taken from [6] is shown by gray area, L_{pc} from [7] is shown by dashed line. Distance $D = 332_{-40}^{+52}$ pc is taken from [8]. Right: the polar cap luminosity L_{pc} for B1133+16, $B_{dip} = 4.26 \times 10^{12}G$, $P = 1.19s$, $\tau = 5.04 \times 10^6$ years [4], $\chi = 55^\circ$ [9]. The observed L_{pc} value taken from [10] is shown by cross hatched area, L_{pc} range from [6] is shown by gray area.

References

1. J. Arons, W.M. Fawley, E.T. Scharlemann, *Astrophys. J.*, **231**, 854, 1979.
2. A.K. Harding, A.G. Muslimov, *Astrophys. J.*, **556**, 987, 2001.
3. Yu.E. Lyubarskii, *Astron. Astrophys.*, **261**, 544, 1992.
4. R.N. Manchester, G.B. Hobbs, A. Teoh, M. Hobbs, *Astron. J.*, **129**, 1993, 2005.
5. I.F. Malov, E.B. Nikitina, *Astron. Rep.*, **56**, 693, 2012.
6. J. Gil, F. Haberl, G. Melikidze et al., *Astrophys. J.*, **686**, 497, 2008.
7. A. Szary, arXiv: astro-ph/1304.4203, 2013.
8. A.T. Deller, S.J. Tingay, M. Bailes, J.E. Reynolds, *Astrophys. J.*, **701**, 1243, 2009.
9. I.F. Malov, E.B. Nikitina, *Astron. Rep.*, **55**, 19, 2011.
10. O. Kargaltsev, G.G. Pavlov, G.P. Garmire, *Astrophys. J.*, **636**, 406, 2006.
11. V.M. Kontorovich, A.B. Flanchik, *J. Exp. Theor. Phys. Lett.*, **85**, 267, 2007.
12. D.M. Sedrakian, A.S. Harutunyan, M.V. Hayrapetyan, *Astrophys.*, **57**, 530, 2014.

Faint Radio Galaxies on the Planck Mission Maps

O.V. Verkhodanov¹, E.K. Majorova¹, O.P. Zhelenkova¹,
D.I. Solovyov², M.L. Khabibullina¹, O.S. Ulakhovich³

E-mail: *vo@sao.ru*

We investigate the distribution of emission on the multifrequency Planck maps toward radio sources of several samples separated by spectral index, redshift, morphology.

The “Cold” surveys were conducted at the RATAN-600 radio telescope in the centimeter and decimeter wavelength ranges. The RC (RATAN-Cold) catalog [1] contains multifrequency flux density measurements. The limiting sensitivity of the RCR (RC Refined) catalog is 10 mJy at 1.4 GHz. We investigated the regions with a radius of 1.5 beam widths at the Planck high frequencies for occurrence of a positive signal at the level of the signal-to-noise ratio $1 < S/N < 3$. We prepared the catalog of 117 radio sources with the measurement data and corresponding continuous spectra from the radio to submm range [2, 3]. Independent flux density estimations of the investigated radio sources, which are presented in the Planck catalog (there are 16 such objects in our list), give evidence of the satisfactory accuracy of flux estimation in the introduced method. Energy distribution in radio source spectra is marked by a rise in the submillimeter range and shows evidence of a dust component which present in AGN. The presence of such sources, difficult to clear out from the CMB maps, complicates the statistical analysis of the Planck CMB maps at scales $< 7'$. Statistics of CMB peaks in the region of the investigated RCR radio sources show distinction for objects of different types: 1) on average, the flat-spectrum sources (i.e., from the spectral range $-0.5 < \alpha \leq 0.5$) fall into the positive peaks region 1.2 times more often than the steep-spectrum objects if the 1σ detection level is set; 2) the average number of cold spots in the range of $S/N > 2.0$ in the $7'$ vicinity of the RCR sources is very small in comparison both with the data on hot spots and with the models. This fact can prove that the selection of the sources in the microwave range is not random.

The stacked images of the Planck CMB maps for different object populations are shown on Fig. 1. Some topological features, e.g. minima and maxima, are visible in the objects areas. We can conclude that the CMB maps contain signal from radio galaxies and/or their parent galaxy, probably, due to a dust

¹ Special Astrophysical Observatory RAS, Nizhnij Arkhyz, Russia

² St. Petersburg Branch of Special Astrophysical Observatory RAS, Pulkovo, Russia

³ Physical Faculty of Kazan Federal University, Russia

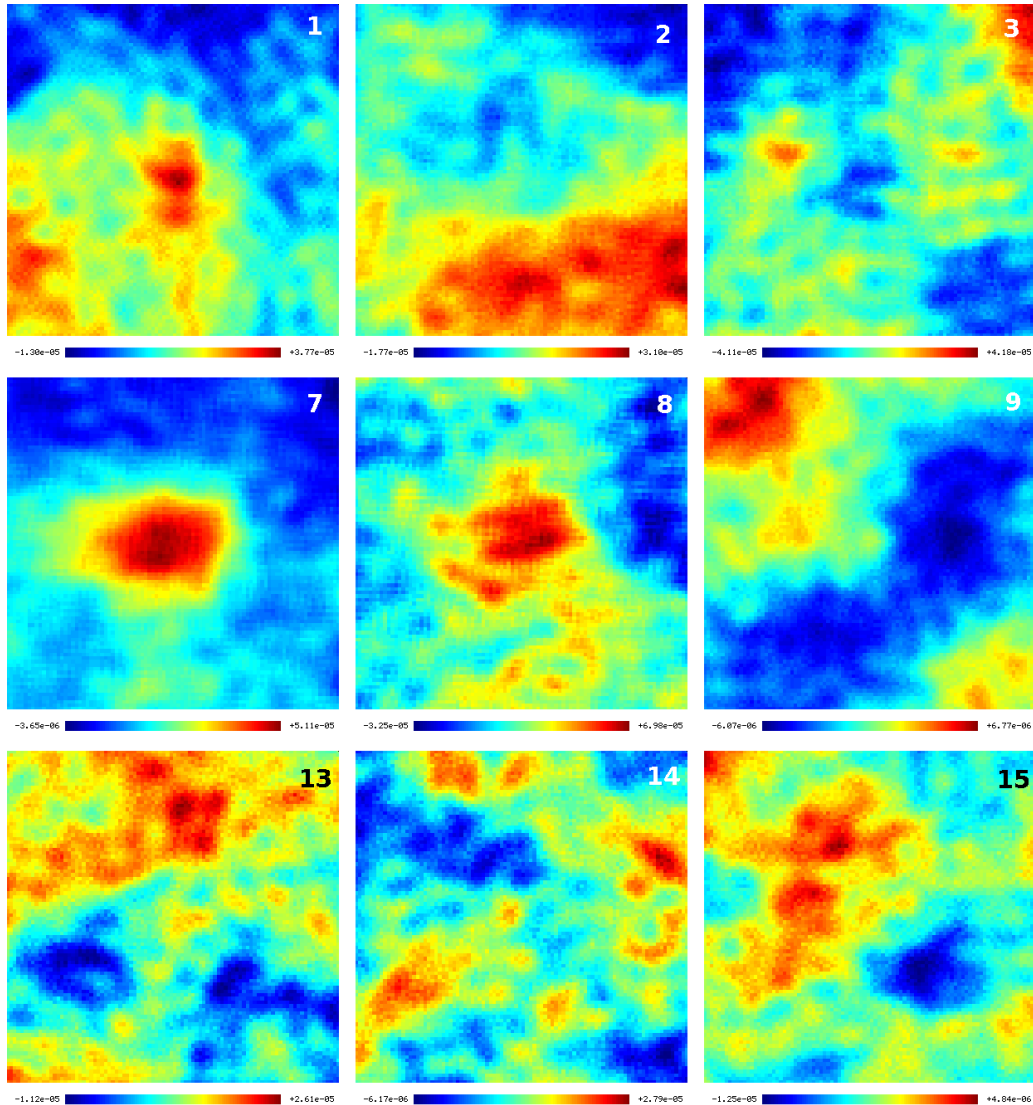
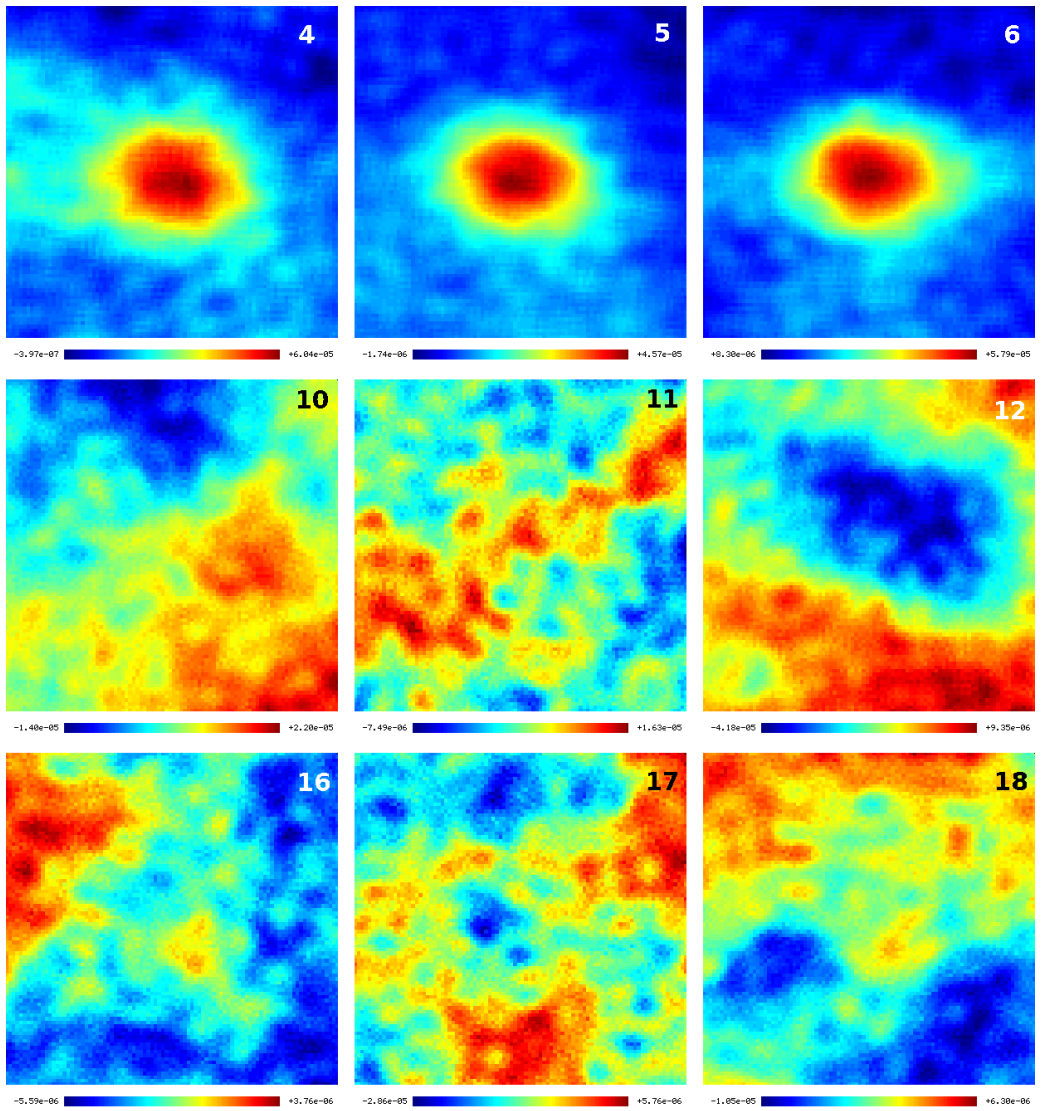


Figure 1: A response from stacking areas from the Planck 2.02 CMB maps around: (1) RCR-objects (117 stacked objects); (2) giant radio galaxies larger $\theta > 4'$ and 1 Mpc (89 obj.); (3) gE and CD galaxies (25 obj.); (4) WENSS radio sources (RS) with the radio spectral index $\alpha < -1.1$ (224 obj.); (5) WENSS RS, $-1.1 \leq \alpha < -0.75$ (661 obj.); (6) WENSS RS, $-0.75 \leq \alpha < -0.5$ (497 obj.); (7) WENSS RS, $-0.5 \leq \alpha < 0$ (238 obj.); (8) WENSS RS, $\alpha \geq 0$ (19 obj.); (9) distant RG, $0.3 \leq z < 0.7$ (1797 obj.); (10) HZRG, $0.7 \leq z < 1.0$ (205 obj.); (11) HZRG, $1.0 \leq z < 1.5$ (149 obj.); (12) HZRG, $1.5 \leq z < 2.0$ (103 obj.); (13) HZRG, $2.0 \leq z < 2.5$ (77 obj.); (14) HZRG, $z \geq 2.5$ (81 obj.); (15) BATSE events with $t < 2s$ (495 obj.); (16) BATSE, $t > 2s$ (1540 obj.); (17) BeppoSAX, $t < 2s$ (87 obj.); (18) BeppoSAX, $t > 2s$ (694 obj.).



component. This signal contaminates the resulting CMB maps [4]. Objects of different population in the stacked area on CMB maps demonstrate different map topology. Some average zones are connected with response similar to Zeldovich–Sunyaev effect observing like minima on the CMB map. Other ones are gE-galaxies often being a center of clusters, distant RGs with $1.5 \leq z < 2$ in the epoch of active cluster formation. Short BATSE events, probably, connected with neutron stars merging in elliptical galaxies, and giant radio galaxies demonstrate inverse Compton scattering of CMB photons with the RG radio lobes electrons.

References

1. Yu.N. Parijskij, N.N. Bursov, N.M. Lipovka et al., *Astron. Astrophys. Suppl.*, **87**, 1, 1991.
2. O.V. Verkhodanov, E.K. Majorova, O.P. Zhelenkova et al., *Astron. Lett.*, **41**, 457, 2015.
3. O.V. Verkhodanov, E.K. Majorova, O.P. Zhelenkova et al., *Astrophys. Bull.*, **70**, 156, 2015.
4. O.V. Verkhodanov, D.I. Solovyov, O.S. Ulakhovich, M.L. Khabibullina, *Astrophys. Bull.*, **71**, 139, 2016.